# DYNAMICAL AND CHEMICAL COUPLING OF THE SUMMER MONSOONS AND THE UPPER TROPOSPHERE-LOWER STRATOSPHERE

A Dissertation

Submitted to the Faculty

of

Purdue University

by

Xinyue Wang

In Partial Fulfillment of the

Requirements for the Degree

of

Doctor of Philosophy

December 2020

Purdue University

West Lafayette, Indiana

# THE PURDUE UNIVERSITY GRADUATE SCHOOL
# STATEMENT OF DISSERTATION APPROVAL


Dr. Yutian Wu, Co-Chair

Lamont-Doherty Earth Observatory, Columbia University

Dr. Wen-wen Tung, Co-Chair

Department of Earth, Atmospheric, and Planetary Sciences

Dr. Alexander Gluhovsky

Department of Earth, Atmospheric, and Planetary Sciences

Dr. Harshvardhan

Department of Earth, Atmospheric, and Planetary Sciences

Dr. Daniel Chavas

Department of Earth, Atmospheric, and Planetary Sciences

**Approved by:**

Dr. Daniel Cziczo

Head of the Department of Earth, Atmospheric, and Planetary Sciences

This thesis is dedicated to my grandparents.

ACKNOWLEDGMENTS

I am profoundly grateful to my supervisor, Prof. Yutian Wu, for continuous encouragement and support for the past five years. Her patience, guidance and invaluable advice have shaped my professional growth and lightened my career path. Thank you Yutian, for the help you provided far beyond academic advising. I couldn't have had a better mentor throughout my Ph.D. career. I also sincerely appreciate my co-advisor Prof. Wen-wen Tung for help me overcoming obstacles throughout my research. She has made my grad school life very enjoyable. I extend thanks to my Ph.D committee members, Prof. Alexander Gluhovsky, Prof. Harshvardhan, and Prof. Daniel Chavas for their insightful comments and interest in my work. Additionally, I would like to thank all the EAPS staff for their assistance and cooperation in various ways.

My sincere thanks go to Dr. Mingfang Ting, Dr. Arlene Fiore, Dr. Lorenzo Polvani, and Dr. Richard Seager. I will never forget how welcome you made me feel when I came to visit the Lamont–Doherty Earth Observatory. I will always treasure the memories of studying at Columbia University.

I would also like to express my heartfelt gratitude to NCAR ACOM UTLS group for hosting my visits. I am so lucky to spend two unforgettable summers with friends in Boulder. Special thanks to Dr. William Randel, who continues to be pillars of support and inspiration in my research and helps set me on my ideal career path. I appreciate Dr. Laura Pan, Dr. Mijeong Park, and Dr. Simone Tilmes, who teach me how to approach scientific problems and inspire me to expand my research perspectives.

Last but not the least, I would like to thank my family and my friends in China for their support. I thank Jianghanyang Li, for his unwavering love and encouragement along the way. And most importantly to my beloved parents, without whom none of this would have been possible.

TABLE OF CONTENTS

Page

# LIST OF TABLES

# LIST OF FIGURES

Figure Page

Figure Page

Figure Page

# ABSTRACT

Wang, Xinyue Ph.D., Purdue University, December 2020. Dynamical and Chemical Coupling of the Summer Monsoons and the Upper Troposphere-Lower Stratosphere. Major Professors: Yutian Wu and Wen-wen Tung.

The upper troposphere-lower stratosphere (UTLS) is a transition region between the troposphere and the stratosphere. During the boreal summer, the UTLS is dominated by large-scale anticyclonic circulations over the Asian and North American monsoon regions, exhibiting complex dynamical and chemical characteristics. Recent studies have emphasized the important role of the summer monsoon system in stratosphere-troposphere exchange of water vapor and chemical species, which strongly influences the atmospheric chemistry and climate system. The transport in the UTLS region occurs in both directions, stratosphere-troposphere transport (STT) and troposphere-stratosphere transport (TST). For example, observational studies indicate localized maxima of tropospheric pollutants and stratospheric water vapor (SWV) in the UTLS, which are controlled by deep convection and large-scale circulation. Meanwhile, stratospheric ozone ($O_3$) can fold into tropospheric air and entrain into the planetary boundary layer (PBL) via deep STT, and thus affect air quality at the surface. In this thesis, we aim at improving the understanding of the transport processes in the UTLS that are linked to monsoon dynamics using observations and modelling tools.

First, we investigate the TST transport in association with the Asian summer monsoon. We examine the simulation of SWV in the Community Earth System Model, version 1 with the Whole Atmosphere Community Climate Model as its atmospheric component [CESM1(WACCM)]. CESM1(WACCM) generally tends to simulate a SWV maximum over the central Pacific Ocean instead of over the Asian continent as observed, but this bias is largely improved in the high vertical resolu-

tion version. The high vertical resolution model with increased vertical layers in the UTLS is found to have a less stratified UTLS over the central Pacific Ocean compared with the low vertical resolution model. It therefore simulates a steepened potential vorticity gradient over the central Pacific Ocean that better closes the upper-level anticyclone and confines the SWV within the enhanced transport barrier.

We further study the transport pathways connecting the Northern Hemisphere surface and the North American (NA) UTLS by diagnosing Boundary Impulse Response idealized tracers implemented at the Northern Hemisphere surface during summer. In ensemble average, air masses enter the NA UTLS region above Central America, and then slowly mix into the higher latitudes. However, fast transport pathways with modal age around two weeks are evident in some tracer ensembles. For these rapid transport pathways, the tracers first reach the UTLS region over the eastern Pacific and the Gulf of Mexico as a result of enhanced deep convection and vertical advection, followed by horizontal transport over the United States by a strengthened UTLS anticyclone circulation.

To the end, we evaluate the downward transport of stratospheric $O_3$ via STT using simulation from a state-of-the-art chemistry climate model implemented with an artificial stratospheric ozone tracer ($O_3S$). We find that $O_3$ transported from the stratosphere makes a significant contribution to the surface $O_3$ variability where background surface $O_3$ exceeds $95^{th}$ percentile, especially over the western U.S. Maximum covariance analysis is applied to $O_3$ anomalies paired with stratospheric $O_3$ tracer anomalies to identify the stratospheric intrusion and the underlying dynamical mechanism. The first leading mode corresponds to deep stratospheric intrusions in the western and northern tier of the U.S., and intensified northeasterlies in the mid-to-lower troposphere along the west coast, which also facilitate the transport to the eastern Pacific Ocean. The second leading mode corresponds to deep intrusions over the Intermountain Regions. Both modes are associated with eastward propagating baroclinic systems, which are amplified near the end of the North Pacific storm tracks, leading to strong descents over the western United States.

# 1. INTRODUCTION

## 1.1 Stratosphere Troposphere Coupling

Earth's atmosphere is divided into several layers on the basis of temperature changes with altitudes. The lowest two layers of the atmosphere are the troposphere and the stratosphere, with temperature dropping rapidly with increasing altitude in the troposphere and increasing in the stratosphere. Also, the chemical compositions of these two layers are fundamentally different: 99% of the water vapor is confined to the troposphere (Mohanakumar, 2008) whereas 90% of the ozone resides in the stratosphere (Dütsch, 1978). The upper troposphere-lower stratosphere (UTLS) region is a transition region between the troposphere and the stratosphere, where mass-exchange processes have a great impact on both the troposphere and stratosphere. Understanding the dynamical and chemical coupling between the stratosphere and troposphere in the UTLS is important as we work to improve the representation of atmospheric processes in global climate models (GCMs) and predict global changes (Shapiro, 1980; Holton et al., 1995; Stohl et al., 2003; Fueglistaler et al., 2009; Randel & Jensen, 2013).

Figure 1.1 highlights the stratosphere-troposphere exchange (STE) processes from Holton et al. (1995). The black dashed line indicates the average position of the thermal tropopause, which is defined as the lowest level at which the temperature lapse rate decreases to 2 K/km or less for the next 2 km by the World Meteorological Organization (WMO, 1986). The tropopause occurs near 17 km in the tropics and gradually slopes downward to the higher latitudes, locating at 8 km in the polar regions (Škerlak, 2014). A global mass circulation denoted by blue arrows is known as the Brewer-Dobson circulation (BDC), which is driven by the extratropical Rossby and gravity wave breaking. The circulation is characterized by strong tropical upwelling from the troposphere to the stratosphere, moving poleward and descending in

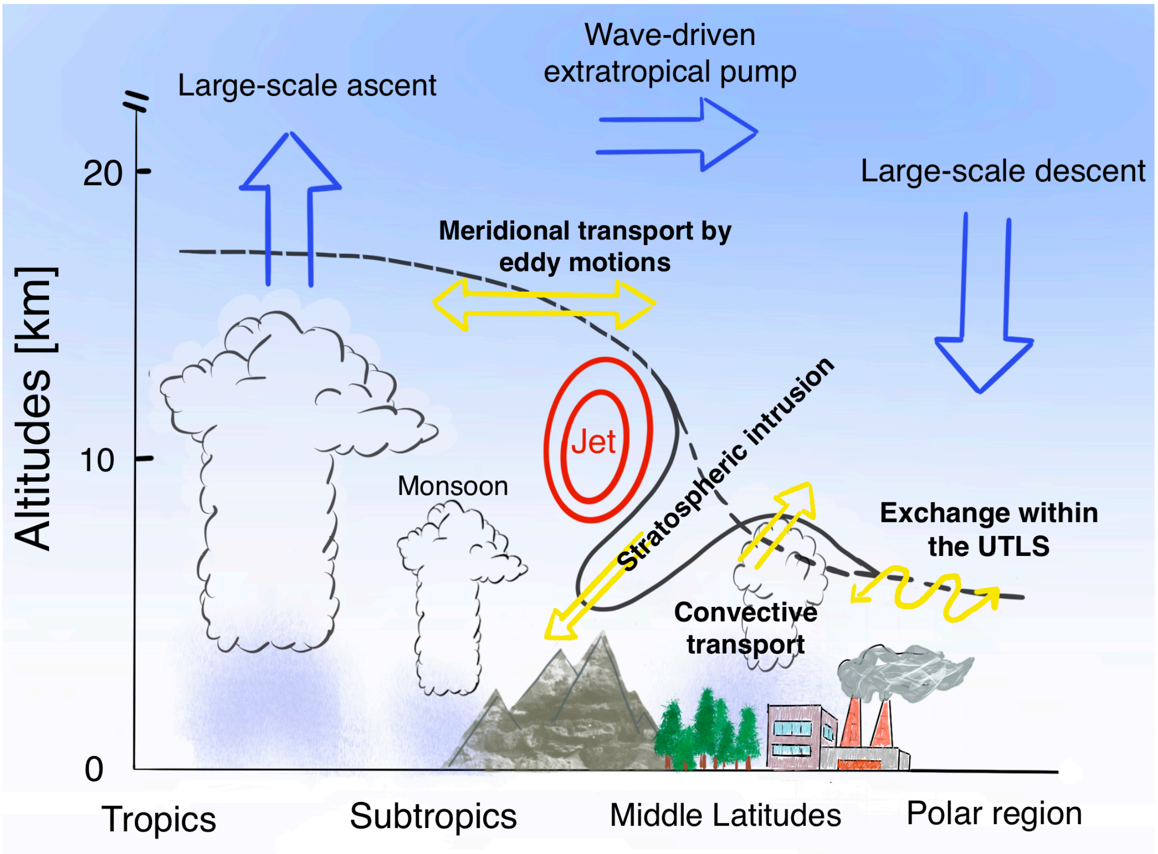


Figure 1.1. The schematic portrays the important processes coupling the stratosphere and troposphere. The black dashed line denotes the climatological tropopause. The solid black line indicates synoptic-scale processes that contribute to two-way stratosphere-troposphere exchange, such as stratospheric intrusions and convective transport. Blue arrows indicate the Brewer–Dobson circulation, which is driven by the extratropical pumping (or the Eliassen-Palm flux divergence). The wiggly arrow indicates the reversible mixing and transfer within the UTLS region.

the high latitudes in both hemispheres (Brewer, 1949; Dobson, 1956; Plumb, 1996). The BDC has been found speeding up since the 1950s, primarily due to the increase of anthropogenic greenhouse gases, and future acceleration is also predicted in global climate models, which will contribute to the recovery of stratospheric ozone (Collins et al., 2003; Hegglin & Shepherd, 2009; Randel, Wu, Voemel, Nedoluha, & Forster, 2006). However, in this thesis we mainly investigate the STE on a smaller spatial and temporal scale denoted by broad yellow arrows, specifically the troposphere-to-stratosphere transport (TST) and the stratosphere-to-troposphere transport (STT) associated with convective activities and the large-scale circulations in the Northern Hemisphere summer months. There are preferred regions of STE. The net TST is found on equatorward of the tropospheric jet whereas the net STT is highest on poleward of the jets in the subtropical and middle latitudes (Stohl et al., 2003; Sprenger & Wernli, 2003; Yang, Chen, Tang, & Hess, 2016). Škerlak (2014) calculated the cross-tropopause mass flux in ERA-Interim and found deep TST signal over China's east coast in JJA. Wu, Orbe, Tilmes, Abalos, and Wang (2020) implemented idealized pulse tracer diagnostic in a global climate model and identified a fast TST pathway over the southern slope of the Tibetan Plateau and northern India. Tropopause folds associated with large-scale subsidence are considered important in STT (X. Wang, Wu, Randel, & Tilmes, 2020). Wu, Chen, Taylor, and Zhang (2018) used idealized aquaplanet model experiments and demonstrated that the northwestern side of the upper-level anticyclone is preferred location for the occurrence of tropopause folds. The rapid transport of the stratospheric ozone ($\sim$ 4 days) into the planetary boundary layer (PBL) during boreal summer is investigated in many studies. The eastern Mediterranean, the Tibetan Plateau, and the mountain ranges along the west coast of North America are most likely influenced by STT by analyzing the ERA-Interim ozone flux from the stratosphere into the PBL (Škerlak, 2014; Zanis et al., 2014).

Recent studies have shown that monsoon system is an efficient pathway in linking the troposphere and stratosphere. The vigorous ascent rapidly lifts tropospheric pollution and aerosols from boundary layer to the convective outflow level ($\sim$ 200 hPa), and part of the air masses are lifted to 100 hPa and the global stratosphere (M. Park, Randel, Emmons, & Livesey, 2009; Bergman, Fierli, Jensen, Honomichl, & Pan, 2013; Wu et al., 2020). Additionally, extreme storms can penetrate the tropopause and directly inject tropospheric air masses into the stratosphere, though with infrequent occurrences (J. B. Smith et al., 2017; Cooney, Bowman, Homeyer, & Fenske, 2018). The water vapor, precursors of ozone-depleting substances, and aerosols transported into the UTLS have a great impact on the Earth's radiation budget and stratospheric chemistry (S. Solomon et al., 2016). Many studies have emphasized the key role of stratospheric water vapor (SWV) in controlling the formation of cirrus clouds and its positive feedback in amplifying global warming and cooling effect in the stratosphere (de F. Forster & Shine, 1999a; Dessler, Schoeberl, Wang, Davis, & Rosenlof, 2013). S. Solomon et al. (2010) showed that a 0.5 ppmv decrease in SWV leads to nearly 30% decrease in the rate of surface warming. Nitric oxide ($N_2O$), chlorofluorocarbons (CFCs), and methane, emitted in industrialized areas and transported to the UTLS region, constitute the principal chemical families ($NO_x$, $ClO_x$, and $HO_x$) that participate in ozone destruction in the stratosphere and above. The nonvolcanic stratospheric aerosols affect the Earth by scattering sunlight back and accelerating stratospheric ozone destruction (Vernier et al., 2015; Yu, Toon, Neely, Martinsson, & Brenninkmeijer, 2015).

STT occurs on a broad range of isentropic surfaces while the deep STT into the PBL is relatively rare, about 10% of the globally integrated STE flux air mass flux penetrates to 700 hPa (Škerlak, 2014). The downward transport of stratospheric ozone during deep STT has been implicated to be an important source of tropospheric ozone (Langford, Aikin, Eubank, & Williams, 2009; Yates et al., 2013; Langford et al., 2017). The tropospheric ozone can pose a threat to human health and the ecosystem even at moderate concentration because of its high oxidation capability. The transport is achieved by a "tongue" containing high stratospheric ozone extrudes downward, folds into the tropospheric air and descends toward the surface. The folded air can directly intersect the surface over high elevation regions such as the mountainous Western United States. Sometimes, tropopause folds induce as much ozone to the surface as those produced by anthropogenic pollution, causing ozone exceedances over the EPA limits (Lin et al., 2012). Most of the previous studies focus on the deep stratosphere-to-troposphere transport during spring because the impact of deep STT on surface $O_3$ are relatively strong at NH extratropics in late spring due to a combination of peak $O_3$ abundances at the tropopause and stronger surface turbulent mixing. The downward ozone transport is typically associated with the dry intrusion branch of the extratropical cyclones (Sprenger & Wernli, 2003; Jaeglé, Wood, & Wargan, 2017). In particular, Lin et al. (2015) used both observations and chemistry climate model output and showed that stratospheric intrusions over the western U.S. occur more frequently in late spring during La Niña phases due to the meandering polar jet and frequent storm activities. Tang, Prather, and Hsu (2011) found coincidences between the geographic patterns of convective events and STT flux over summer continents. It suggests that the convective air masses penetrating into the lower stratosphere will force subsidence, pushing the stratospheric air below it into lower model layers and eventually into the troposphere. The physical processes of the summertime stratospheric intrusions and the quantity of ozone associated with these deep intrusions, however, remain obscure, largely because of the limitation in observations. In addition, most of the previous studies examined individual tropopause fold cases. The linkage between summertime stratospheric intrusions and surface ozone enhancements from a long-term climatological perspective deserves closer investigation.

There are other STE processes associated with eddy motions near the tropopause, including stratospheric streamers, potential vorticity (PV) cutoffs (Holton et al., 1995; Sprenger, Wernli, & Bourqui, 2007), and eddy sheddings (Hsu & Plumb, 2000; Popovic & Plumb, 2001; Garny & Randel, 2013), but these will not be discussed in this thesis.

### 1.2 The summer monsoons and the UTLS coupling

The Asian summer monsoon sweeps across India, Southeast Asia, China, Japan, and the western Pacific, influencing the lives of more than a billion people (Rodwell & Hoskins, 1996). As its counterpart in the Western Hemisphere, the North American monsoon also impacts urban complexes and vast agricultural areas with a current population of about 12 million people (Adams & Comrie, 1997). With rapid growth in population and industrial activities across the monsoon regions, the monsoonal convection coupled to surface emissions can have profound consequences on air quality and the UTLS composition. The tropospheric chemical species in the UTLS enhance aerosol–cloud interactions and in turn change the behavior of monsoon systems (B. Wang, Yim, Lee, Liu, & Ha, 2014; X. Li, Ting, Li, & Henderson, 2015). Therefore, the coupling between the summer monsoons and the UTLS is crucial in understanding processes bridging regional air quality, global chemistry-climate interaction, and climate change.

The monsoon circulation contains cyclonic flow with convective updrafts in the troposphere and strong anticyclonic vortex in the UTLS (Gettelman, Kinnison, Dunkerton, & Brasseur, 2004; Randel & Park, 2006; Randel et al., 2010). During boreal summer, the anticyclone in response to the Asian monsoon is the most pronounced circulation pattern in the UTLS (Hoskins & Rodwell, 1995). There are continuing efforts to understand the transport processes of the chemical species entering the UTLS associated with the Asian summer monsoon. Fu et al. (2006) used satellite measurements and suggested that the convective overshooting over the Tibetan Plateau (TP) and its south slope is primarily responsible for the transport into the UTLS region. However, M. Park et al. (2009) used a global chemistry transport model with tagged surface emission of carbon monoxide and demonstrated that the influence of deep convection over TP is minor. Instead the convection within Southeast Asia is found to be highly influential in lofting the surface air upward to the convective detrainment level near 12 km. Part of the air masses are lifted subsequently by slow upward motion to

100 hPa and above through a vertical conduit, which is located on the eastern side of the anticyclone. Recently, Wu et al. (2020) examined transport pathways linking the surface to the UTLS using an idealized pulse passive tracer approach to reveal the transport dynamics. Fast transport paths are identified over the southern slope of the TP, northern India, and Saudi Arabia with a modal age of 5-10 days. They showed that the vertical eddy flux controls the transport at 100-150 hPa while convective processes dominate around 200-300 hPa. The North America (NA) summer monsoon anticyclone is also apparent but is substantially weaker (Higgins, Yao, & Wang, 1997; Siu & Bowman, 2019) than its Asian sister. It is likely that the transport characteristics related to the NA summer monsoon behave differently than those in Asia due to the very different topography, convection and large-scale circulations in the two regions. Therefore, an investigation of the relative contributions due to distinct mechanisms and their transport timescales associated with the NA summer monsoon based on the idealized pulse passive tracer approach is needed.

In addition to the distinctive dynamical signature, monsoon coupled with strong local emission leaves an evident anthropogenic signature on chemical composition in the UTLS (Santee et al., 2017). Both observational and modeling studies have revealed that the Asian monsoon anticyclone is coincide with localized maxima in tropospheric tracer constituents in the UTLS, including pollution aerosols (Vernier, Thomason, & Kar, 2011; Vernier et al., 2015; Lau, Yuan, & Li, 2018), carbon monoxide (Q. Li, Jiang, et al., 2005; Q. Li, Jacob, et al., 2005), hydrogen cyanide (Randel et al., 2010), nitrogen oxides (M. Park, Randel, Kinnison, Garcia, & Choi, 2004) and stratospheric water vapor (M. Park, Randel, Gettelman, Massie, & Jiang, 2007; Randel, Zhang, & Fu, 2015). The enhanced pollution in the UTLS is associated with the confinement of strong upper-level anticyclones over both monsoon regions. Once entering the UTLS, the air parcel tends to circulate but is confined within the monsoon anticyclonic flow associated with steepened geopotential height and PV gradients (Dunkerton, 1995; M. Park et al., 2007). The promoted gradients are characterized as a barrier to suppress horizontal transport across gradients (Rosenlof, Tuck, Kelly, Russell, & McCormick, 1997; M. Park et al., 2008; Garny & Randel, 2013; Ploeger et al., 2015), and confine the slowly rotating air parcels within the anticyclone.

As discussed above, the localized maximum of SWV within the Asian summer monsoon anticyclone has been well observed and documented in satellite studies, yet discrepancies are found in model simulations among different configurations of the Whole Atmosphere Community Climate Model (WACCM) (X. Wang et al., 2018). Wet biases are commonly seen over the subtropical central Pacific in WACCM models. This bias in simulating SWV implies the lack of some dynamical or chemical processes in the models. Poorly simulated SWV in GCMs can cause uncertainties in reproducing moist processes and thus affect the accuracy of future projections. Thus, it is important for us to understand the biases in SWV simulations in order to improve the model performance.

## 1.3 Outline

In this thesis, we study the dynamical and chemical linkage between the summer monsoonal circulations and the UTLS. We use both observational measurements and model experiments to investigate the summertime cross-tropopause transport processes in both directions, specifically troposphere-stratosphere transport (TST) and stratosphere-troposphere transport (STT), and the associated dynamical mechanisms.

The thesis is composed of 5 chapters. First, we investigate troposphere-stratosphere transport using observational measurement and WACCM simulations. Satellite observations have shown a persistent maximum in stratospheric water vapor (SWV) in the UTLS confined by the upper-level anticyclone over the Asian summer monsoon region. However, the discrepancies in simulating SWV over the Asian summer monsoon region are commonly found in different configurations of CESM1(WACCM). In Chapter 2, we show that the WACCM version 5 with increased vertical layers (WACCM5-L110) resolves the UTLS temperature more accurately which better confines the SWV within the transport barrier. In Chapter 3, we study efficient pathways connecting surface air to the North American (NA) UTLS by using the pulse tracer diagnostic implemented in higher vertical resolution WACCM5. We find that deep convection controls transport from the boundary layer to 200 hPa while enhanced large-scale circulation dominates transport upwards into the UTLS region and anti-cyclonically towards southern United States.

Regarding the stratosphere-troposphere transport, we focus on deep stratospheric intrusions and its impact to surface episodic ozone extremes in Chapter 4. We analyze the daily WACCM6 simulations and find that $O_3$ transported from the stratosphere makes a significant contribution to the surface $O_3$ variability where background surface $O_3$ exceeds $95^{th}$ percentile over the western U.S. The deep stratospheric intrusion is associated with eastward propagating baroclinic systems, which are amplified near the end of the North Pacific storm tracks, leading to strong descents over the western U.S.

Finally, our findings are summarized in Chapter 5, where we also discuss open questions and further directions. The overarching goal of my research is to advance our understanding of the dynamical and chemical processes in the upper troposphere and lower stratosphere (UTLS) associated with summer monsoons. The results of this work will help close critical gaps in our knowledge about dynamical-chemical coupling in the UTLS region.

# 2. THE SIMULATION OF STRATOSPHERIC WATER VAPOR OVER THE ASIAN SUMMER MONSOON IN CESM1(WACCM) MODELS

The work contained in this chapter has been published in Journal of Geophysical Research Atmospheres.

## 2.1 Introduction

Both satellite and aircraft measurements show that tracer constituents exhibit localized extrema in the upper troposphere lower stratosphere (UTLS) over the Asian and North American monsoon regions during boreal summer, such as maxima of tropospheric species like methane (M. Park et al., 2004), carbon monoxide (CO; Q. Li, Jiang, et al., 2005; Q. Li, Jacob, et al., 2005; Pan et al., 2016; Garny & Randel, 2016) and stratospheric water vapor (Rosenlof et al., 1997; Randel et al., 2001; Gettelman et al., 2004; Dessler & Sherwood, 2004; Milz et al., 2005; M. Park et al., 2007; Randel et al., 2015; K. Zhang, Fu, Wang, & Liu, 2016) and minima of stratospheric species like ozone (Randel et al., 2001; Gettelman et al., 2004; Randel & Park, 2006; M. Park et al., 2007, 2008). Among these chemical constituents in the UTLS, stratospheric water vapor (SWV) is important due to not only its radiative forcing on surface climate (de F. Forster & Shine, 1999b; S. Solomon et al., 2010; Maycock, Joshi, Shine, & Scaife, 2013) but also its chemical effects on stratospheric ozone (Dvortsov & Solomon, 2001) and chlorine activation reactions (Anderson, Wilmouth, Smith, & Sayres, 2012; S. Solomon et al., 2016). The importance of a realistic representation of the SWV over the Asian summer monsoon region in atmospheric models has been emphasized in simulating troposphere-stratosphere exchange correctly (Dethof, O'Neill, Slingo, & Smit, 1999; Bannister, O'neill, Gregory, & Nissen, 2004; Ploeger et al., 2013). Additionally, chemical species like SWV also provide a complementary perspective on the upper-level monsoon circulation dynamics (M. Park et al., 2009; Ryu & Lee, 2010; Garny & Randel, 2013). However, models perform poorly in terms of their simulation of SWV (Jiang et al., 2012; Takahashi, Su, & Jiang, 2016). Considerably large model biases in the simulations of SWV are found among models that participated in the Phase 5 of Coupled Model Intercomparison Project (CMIP5). There exists both wet- and dry-biases, ranging from 1% to about 200% at 100 hPa based on the multi-year mean vertical profiles of $H_2O$ in CMIP5 models. Eight out of nineteen CMIP5 models evaluated in Jiang et al. (2012) differ from the observed SWV at 100 hPa by more than 30%.

Previous studies have investigated the dynamical processes influencing the SWV over the Asian summer monsoon regions. It has been suggested that chemical tracers vertically transported by convection over the monsoonal region can reach the convective outflow level near 12 km (Folkins, Oltmans, & Thompson, 2000; Gettelman et al., 2002), and part of them are lifted subsequently by slow upward motion to 100 hPa and above (M. Park et al., 2007, 2008, 2009; Uma, Das, & Das, 2014). As demonstrated in model experiments of Bergman et al. (2013) and Pan et al. (2016), air parcels likely enter the UTLS through a vertical conduit between the center of the Asian monsoon anticyclone (AMA) and the strongest convective activity, and are then circulated but confined within the monsoon anticyclonic flows associated with steepened geopotential height and potential vorticity (PV) gradients (Dunkerton, 1995; Jackson, Driscoll, Highwood, Harries, & Russell, 1998; Dethof et al., 1999; M. Park et al., 2007; Ploeger et al., 2015; Ploeger, Konopka, Walker, & Riese, 2017). The promoted gradients are characterized as a barrier to suppress horizontal transport across gradients (Rosenlof et al., 1997; Q. Li, Jiang, et al., 2005; Randel & Park, 2006; M. Park et al., 2008; Bergman et al., 2013; Garny & Randel, 2013; Ploeger et al., 2015, 2017), and confine the slowly rotating air parcels within the AMA.

Both observational and modeling studies have been done to investigate the effects of monsoon convection on SWV. Dessler and Sherwood (2004) and Schwartz et al. (2013) proposed that the penetration by overshooting deep convection contributes to a wetter tropopause, implying that the monsoon deep convection susceptibly has a moistening effect in the UTLS. However, overshooting convection occurs irregularly, and the prominent center of deep convection is not co-located with but rather on the southeastern side of the SWV maximum [see Figure 2 in M. Park et al. (2007) and Fig. 2a in Randel et al. (2015)]. These facts cast doubts on this mechanism. Recently, Wright, Fu, Fueglistaler, Liu, and Zhang (2011) and Randel et al. (2015) suggested that the large-scale circulation and the temperature on the southern side of the AMA play a dominant role in controlling the SWV over the Asian summer monsoon region, and in particular, they found the stronger (weaker) the convection, the colder (warmer) the subtropical temperature, the dryer (wetter) the SWV at 100 hPa. This serves as a dehydration mechanism, which is governed by adiabatic cooling during the convection-driven upwelling and subsequent freezing out following the Clausius-Clapeyron relationship. The linear regression analysis between circulation and SWV variations at 100 hPa in observations shows an anomalous upper-level anticyclonic flow pattern during anomalous dry events, implying that dry UTLS is accompanied by an intensified AMA, which corresponds to a stronger monsoonal convection (Gill, 1980; Rodwell & Hoskins, 1996), and vice versa. Randel et al. (2015) suggested that the temperature on the southern side of the AMA acts as a key link between the large-scale circulation and SWV. M. Schoeberl and Dessler (2011) and Kim, Grise, and Son (2013) commented that small temperature variance can significantly affect the SWV, i.e. a 4 K temperature change at 100 hPa could induce 60% (approximately 3 ppmv) variation of SWV following the Clausius-Clapeyron relationship. Both radiosonde measurements and model experiments indicate that convection exerts a cooling effect in the AMA region, which is associated with radiative cooling, cold air entrainment and equatorial wave propagation in the upper troposphere (Gage et al., 1991; Tsuda, Murayama, Wiryosumarto, Harijono, & Kato, 1994; Highwood & Hoskins, 1998; Norton, 2001; Zhou & Holton, 2002; Gettelman et al., 2002; Sherwood, Horinouchi, & Zeleznik, 2003; Kuang & Bretherton, 2004; Randel & Wu, 2005; M. Park et al., 2007; Kim, Randel, & Birner, 2018). Therefore, the dehydration mechanism suggests that enhanced convection substantially dehydrates the air, as opposed to the moistening effect by overshooting convection.

Previous studies mostly examined the simulations of area-averaged SWV (Inness, Slingo, Woolnough, Neale, & Pope, 2001; Roeckner et al., 2006; Hardiman et al., 2015), generally in the deep tropics; however, a detailed investigation of the spatial distributions over the summer monsoon regions has not yet been performed. More specifically, the questions we aim to address in this study are: 1. How good is SWV simulated in the Whole Atmosphere Community Climate Model (WACCM) experiments? 2. What causes the biases in the simulation of SWV? 3. Several studies have emphasized the importance of increased model vertical resolution in capturing many critical UTLS processes (Lindzen & Fox-Rabinovitz, 1989; Pope, Pamment, Jackson, & Slingo, 2001; Inness et al., 2001; Roeckner et al., 2006; Gettelman et al., 2010; Charlton-Perez et al., 2013; Kim et al., 2013; Abalos, Randel, Kinnison, & Serrano, 2013; W. Wang, Matthes, Schmidt, & Neef, 2013; Richter, Solomon, & Bacmeister, 2014). Therefore, will increased model vertical resolution promote an improved representation of the monsoon signature on the SWV? The remainder of the paper is organized as follows: Section 2 describes the model experiments and observational data, Section 3 presents the model evaluation of both SWV and CO and proposes the underlying mechanism for the model biases. Summary and discussions are in Section 4.

## 2.2 Data and Methods

### 2.2.1 The WACCM Experiments

The Community Earth System Model version 1 (CESM1; Hurrell et al., 2013) WACCM includes interactive atmosphere, ocean, land, and sea-ice components (Marsh et al., 2013; Mills et al., 2016). WACCM is one of the high-top state-of-the-art chemistry-climate models, integrating the atmospheric physics and chemistry from the surface to nearly 140 km. Two model configurations with almost identical model setups but different vertical resolutions are examined in this study: CESM1(WACCM)-L70 (hereafter L70) with 70 vertical levels and CESM1(WACCM)-L110 (hereafter L110) with 110 vertical levels, both with horizontal resolution of 0.95° latitude × 1.25° longitude (∼100 km). The vertical resolution in the mid-troposphere and lower stratosphere is about 1.2/0.5 km in the L70/L110 (see Fig. 2.1). The two models include improved physics processes, convective parameterizations and fully interactive chemistry modified from the Community Atmosphere Model, version 5 (CAM5; Neale et al., 2010; Mills et al., 2016). The orographic and non-orographic gravity waves drag (GWD) parameterizations are almost identical in L70 and L110 following Richter, Sassi, and Garcia (2010). The parameter tuning of GWD is modified as a result of refined vertical resolution following the Stratosphere-troposphere Processes And their Role in Climate (SPARC) Quasi-Biennial Oscillation initiative (QBOi) protocol (Butchart et al., 2018). L70 and L110 are coupled to the biogeophysical and biogeochemical parameterizations and numerical implementation of version 4.5 of the Community Land Model (CLM4.5; Oleson et al., 2013). Most of the details about L70 are documented in Mills et al. (2017) and the details of L110 are described in Butchart et al. (2018). The climatological simulations averaged over June, July and August (JJA) spanning the range from 1979 to 2014 in both models are compared.

Both the L70 and L110 are fully coupled ocean-atmosphere experiments, and the difference between the two reveals the impact due to solely vertical resolution. In addition to the coupled model, L110 forced with prescribed sea surface temperatures (SSTs) and sea ice properties based on the Atmospheric Model Intercomparison Project (AMIP) experiment (Taylor, Stouffer, & Meehl, 2012) is also examined here. Additionally, two experiments subject to the same settings but with different boundary conditions using CESM1(WACCM4), which participated in the Chemistry Climate Model Initiative (CCMI) experiments (Eyring et al., 2013; Morgenstern et al., 2017) with nudged Quasi-Biennial Oscillation (QBO), are used. One integration is an AMIP-style (CCMI-AMIP) run whereas the other is a coupled ocean-atmosphere run (CCMI-Coupled). WACCM4 has a horizontal resolution of 1.9° latitude × 2.5°

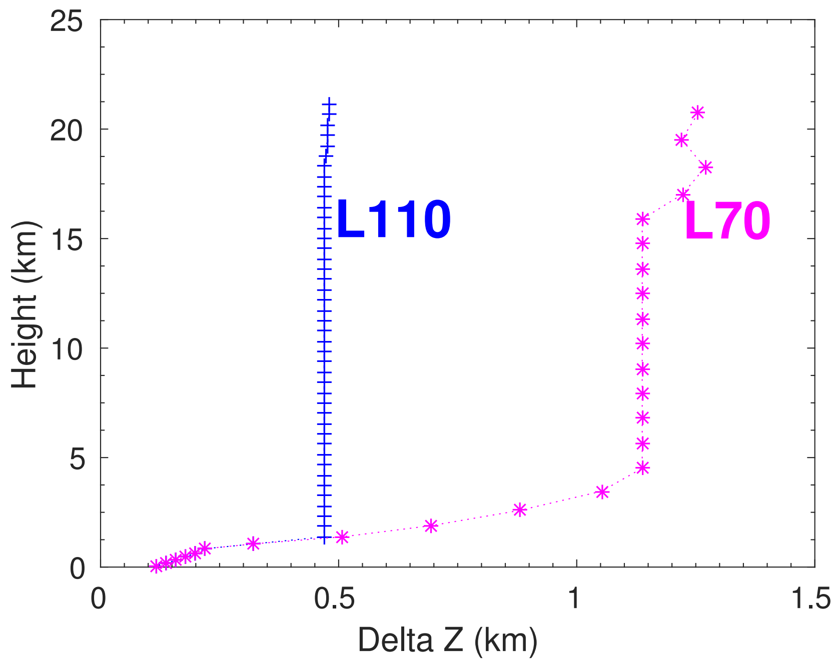


Figure 2.1. Vertical grid spacing in km as a function of height used in the CESM1(WACCM) simulations with 70 vertical levels (asterisks) and 110 vertical levels (plus signs) from the surface to 50 hPa.

Table 2.1.
Characteristics of the Models Analyzed in the Study

| Model | Vertical Layers | Horizontal Resolution | Period Spanned |
|---|---|---|---|
| CESM1(WACCM)-L70 | 70 | 0.95° latitude × 1.25° longitude | 1979-2014 |
| CESM1(WACCM)-L110 | 110 | 0.95° latitude × 1.25° longitude | 1979-2014 |
| L110-AMIP | 110 | 0.95° latitude × 1.25° longitude | 1979-2014 |
| CCMI-AMIP | 66 | 1.9° latitude × 2.5° longitude | 1979-2014 |
| CCMI-Coupled | 66 | 1.9° latitude × 2.5° longitude | 1979-2014 |
| CESM1(WACCM4) | 66 | 1.9° latitude × 2.5° longitude | 1950-2006 |
| SC-WACCM4 | 66 | 1.9° latitude × 2.5° longitude | 1950-2008 |
| SD-WACCM4 | 88 | 1.9° latitude × 2.5° longitude | 2005-2010 |

longitude and 66 layers in the vertical (Marsh et al., 2013; Tilmes et al., 2016; Garcia, Smith, Kinnison, Cámara, & Murphy, 2017) and is the high-top version of CAM4. The information of WACCM experiments with different configurations evaluated in this study are summarized in Table 1.

### 2.2.2 Microwave Limb Sounder Water Vapor

We analyze the water vapor measurements derived from the Aura Microwave Limb Sounder (MLS) version 4.2 level 2 products (Livesey et al., 2015). The main development in MLS v4.2 waer vapor retrievals is an improved cloud detection methodology. MLS data are available from 2004 to present. Here we use the retrievals spanning the range from 2005 to 2014 to evaluate the performance of CESM1(WACCM) models. MLS provides $H_2O$ (water vapor volume mixing ratio in ppmv) with vertical resolution around 3 km in the UTLS. The uncertainties in $H_2O$ measurements are about 20% near the upper troposphere (215 hPa) and 10% at the UTLS (100 hPa) in the tropics and mid-latitudes (Jiang et al., 2012, 2015).

### 2.2.3 ERA-Interim Meteorological Analyses

We use both daily and monthly meteorological analyses from ERA-Interim (ERAI) reanalysis (Dee et al., 2011), including temperature and wind fields with horizontal resolution of 1° latitude × 1° longitude. Monthly ERAI data during the overlapping time period as the WACCM experiments (1979-2014) are analyzed to validate the model simulations of temperature and circulations. Both daily and monthly ERAI data of PV, temperature and circulations from 2005 to 2014 overlapping with MLS data are used for composite analysis.

## 2.3 Results

The analyses are mostly performed on the simulations at 100 hPa level. MLS observations show that the localized SWV maxima during boreal summer are primarily at 100 hPa (Randel et al., 2015; K. Zhang et al., 2016), which is confined by the AMA effectively near 100 hPa (Randel & Park, 2006). Furthermore, Randel et al. (2015) found that the climatology and variability of SWV was nearly identical on isentropic versus pressure levels. Therefore, we choose the model levels nearest to 100 hPa in order to avoid uncertainties due to interpolation, specifically 103 hPa in L70 and 102 hPa in L110. If not specified, the pressure levels in this study refer to the nearest model levels. Temperature fields nearest to 200 hPa are also explored.

### 2.3.1 Simulation of Stratospheric Water Vapor over the Asian Summer Monsoon Region

The boreal summer (JJA) climatological distributions of 100 hPa water vapor in MLS data and the L70/L110 simulations during 2005-2014 are shown in Fig. 2.2. The model results are not sensitive to the averaging time period (similar results are found during 1979-2014; not shown). The 100 hPa horizontal circulation averaged during 2005-2014 is also shown in Fig. 2.2. The circulation in Fig. 2.2a shows the equatorial easterly, subtropical westerly and the relatively strong meridional flows acting together to encompass the AMA center. The maxima SWV values (∼5.3 ppmv) at 100 hPa are clustered over the zonally elongated domains of 20°-35°N, 40°-120°E, strongly coherent within the AMA but distant from the deep convection center in the Southeast Asia. The localized SWV maximum in observations exhibits a strong monsoon dynamical signature.

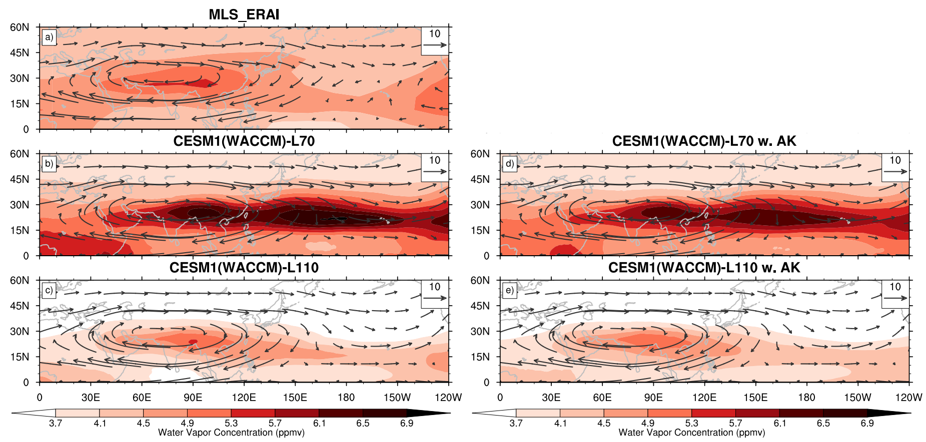


Figure 2.2. The colors show the summertime SWV (ppmv) at 100 hPa from (a) MLS, (b) L70, (c) L110, (d) L70 weighted by AK and (e) L110 weighted by AK during 2005-2014, overlaid with the averaged horizontal winds (m/s) in vectors during 2005 to 2014 at that level. Winds in (a) are from ERAI, (b, d) and (c, e) are from L70 and L110, respectively.

Fig. 2.2b and Fig. 2.2c show the multi-year mean SWV and circulation simulated in L70 and L110, respectively. To better highlight the model performance as compared with observations, Fig. 2.3a and Fig. 2.3b show the percentage differences in L70 and L110 relative to MLS observations. It is noteworthy that, in L70 (shown in Fig. 2.2b), the maximum (∼6.9 ppmv) is located over the central Pacific (170°E-170°W) and the secondary maximum (∼6.5 ppmv) is located within the AMA. Although the overall magnitude of SWV over the continent is well captured in L70, the wet bias over the central Pacific (∼50%) significantly exceeds the 10% range of uncertainty in MLS (shown in Fig. 2.3a). The bias in SWV in L70, in particular that the maximum is located over the ocean rather than the continent, is surprising given the current understanding of the AMA dynamics (Rodwell & Hoskins, 1996; Qu & Huang, 2015) and the observed linkage between the AMA and SWV (Randel et al., 2015). Compared with L70, L110 with increased vertical resolution and refined GWD parameterizations, shows a significant improvement in the simulation of SWV, particularly in terms of its spatial distribution. Fig. 2.2c displays a maximum of about 5.3 ppmv located within the AMA in L110, which is similar to observations (Fig. 2.2a). Comparing to the SWV in MLS, L110 has a dry bias (∼25%) poleward of 30°N (see Fig. 2.3b). The meridional velocity on the eastern flank of the AMA decreases sharply from the continent to the ocean, which helps the anticyclonic flows close better in L110.

The effects of the averaging kernels (AKs) on the simulated SWV at 100 hPa are checked. The details about the MLS AKs are discussed in (Livesey et al., 2015). Fig. A.1 displays the equatorial MLS v4.2 AK that we applied to the simulations. Fig. 2.2d and Fig. 2.2e show the SWV convolved with the AK from L70 and L110, respectively. The weighted SWV shown in Fig. 2.2d and e stay very close to what we have seen in Fig. 2.2b and c, which indicates the influence of AK is small in the subtropics.

In addition to the SWV difference, discrepancies are also found in the temperatures and circulations in L70 as shown in Fig. 2.4a with respect to the summer climatology (2005-2014) in ERAI reanalysis. There is a warm bias over the continent and a cold bias over the central Pacific Ocean (boxed regions in Fig.2.4; 15°-30°N, 170°E-170°W) in L70 and the anomalous westerlies exist along the entire subtropics in L70 as compared with those in ERAI reanalysis and L110 (Fig. 2.4a, Fig. 2.7b, a and Fig. 2.9a). The eastern branch of the AMA is found extending eastward to the central Pacific Ocean, which we claim is responsible for the poor simulation of the SWV (to be discussed). The biases of temperatures, especially the cold center over the central Pacific Ocean, are reduced in L110 as compared with L70 (see Fig. 2.4b).

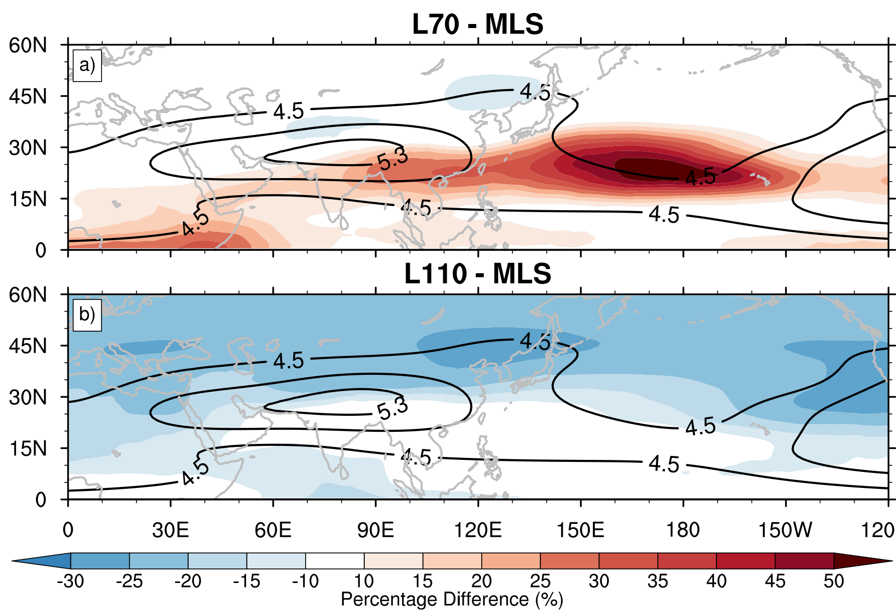


Figure 2.3. Color shadings show the percentage difference in (a) L70 and (b) L110 with respect to the MLS measurements during JJA 2005-2014. The black contours are the MLS SWV as in Fig. 2.2a with contour interval of 0.4 ppmv.

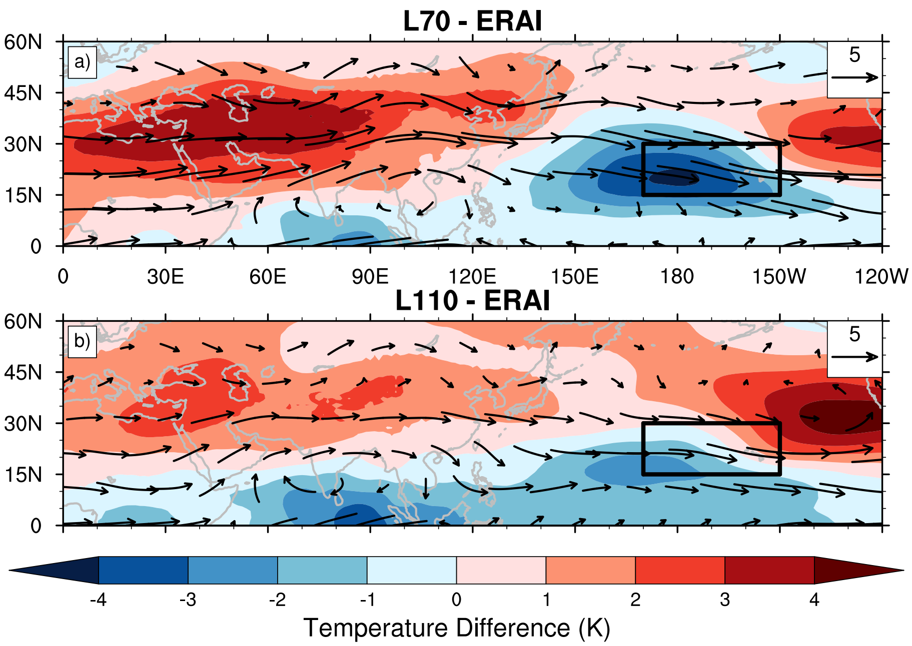


Figure 2.4. Color shadings and vectors represent the difference in the 100 hPa temperature (K) and the difference in the 100 hPa horizontal wind fields (m/s) in (a) L70 and (b) L110 with respect to the ERAI reanalysis from 2005 to 2014.The black boxes outline the domains (15°-30°N, 170°E-170°W) in which large temperature differences are found.

Though both L70 and L110 presented above are coupled models, the side-by-side comparisons of coupled runs with their atmosphere-only counterparts indicate that the performance of simulated SWV and circulation around 100 hPa is insensitive to boundary conditions. As depicted in Fig. A.2, the simulation of AMIP-style L110 (Fig. A.2a) closely resembles the structure of coupled runs (Fig. A.2c) and observations. Compared with coupled L110, the dry bias over the continent is improved and the AMA is better closed in AMIP-style L110. Meanwhile, the common deficiencies can be seen in both the AMIP-style (Fig. A.2b) runs and coupled runs (Fig. A.2d) from the WACCM4 CCMI experiments, notably with the SWV maximum shifted eastward and circulations extended to the Pacific Ocean. This suggests that the differences in SWV simulations are likely due to the model vertical resolution and refined GWD parameterizations and not to differences in boundary conditions.

Moreover, other configurations of WACCM4 that are available are also studied (see Table 1 and Fig. A.3), i.e. CESM1(WACCM4) in the CMIP5 archive, specified chemistry (SC)-WACCM4 (K. L. Smith, Neely, Marsh, & Polvani, 2014) and specified dynamics (SD)-WACCM4 (Kunz, Pan, Konopka, Kinnison, & Tilmes, 2011; Lamarque et al., 2012). The specific humidity (kg/kg) outputs from these models are converted to the water vapor volume mixing ratio by multiplying 1.61 (ppmv/ppm). The CESM1(WACCM4) (Fig. A.3a) and SC-WACCM4 (Fig. A.3b) look remarkably similar to each other but both unrealistically simulate the SWV maximum over the Pacific Ocean. The SD-WACCM4 is nudged towards the Goddard Earth Observing System, Version 5 (GEOS-5) meteorological analysis (i.e., horizontal wind and temperature fields) of NASA's Global Modeling and Assimilation Office (GMAO) (Rienecker et al., 2011; Lamarque et al., 2012; Arnone, Smith, Enell, Kero, & Dinelli, 2014). The SD-WACCM4 similarly shows a maximum of SWV over the central Pacific Ocean (see Fig. A.3c), and this bias is also found in the Modern-Era Retrospective Analysis for Research and Applications (MERRA) reanalysis specific humidity (not shown). The biased SWV in SD-WACCM4 is likely attributed to the unreliable temperature in MERRA reanalysis above 300 hPa (Jiang et al., 2012; Tian et al., 2013;

Jiang et al., 2015). The temperature differences of MERRA compared with ERAI in the UTLS can be up to 2 K [see Fig. C3 in Fueglistaler et al. (2013) and Fig. 3-5 in Bosilovich et al. (2015)]. To sum up, the discrepancies are commonly found in WACCM experiments with different configurations.

In Section 3.2, we will focus on the L70 and L110 and will provide a possible mechanism to explain the differences between the two, specifically the magnitude and spatial pattern associated with the Asian summer monsoon circulation.

### 2.3.2 Mechanisms Underlying Differences in High and Low Vertical Resolution Models

#### Differences in Temperatures in High and Low Vertical Resolution Models

Since the SWV relies strongly on the UTLS temperature, we start by analyzing the temperatures between the high and low vertical resolution models. Fig. 2.5a and Fig. 2.5b show the temperature differences in L70 and L110 at 100 hPa and 200 hPa, respectively. It is noteworthy that salient temperature difference (∼1.5-3 K) between L70 and L110 lies over the central Pacific Ocean at 100 hPa (see Fig. 2.5a). Similar patterns are found averaging from 1979-2014 (not shown). In L70, it is relatively colder over the subtropical central Pacific (boxed regions in Fig.2.5; 15°-30°N, 170°E-170°W) compared to L110. The cold bias is accentuated at higher levels above 100 hPa. However, the temperature difference in the subtropics shows the opposite sign in the levels below 140 hPa (see 200 hPa as an example, shown in Fig. 2.5b). The zonal mean temperature differences between the two models in a longer time period (1979-2014) are shown in Fig. 2.6a. The dipole structure in the temperature difference suggests that the lower vertical resolution model is relatively warmer in the free troposphere and cooler in the lower stratosphere, which is a robust result as found in other studies (Pope et al., 2001; Inness et al., 2001; Roeckner et al., 2006; Richter et al., 2014). Similar temperature bias pattern can be found in L70 relative to ERAI (see Fig. 2.6b). But this bias is largely reduced in L110 (see Fig.

2.6c). In the Northern Hemisphere (NH) subtropics, the warm anomaly in L70 in the troposphere is largely due to the warm anomaly over the Pacific Ocean and the cold anomaly in the lower stratosphere is dominated by that over the Pacific Ocean.

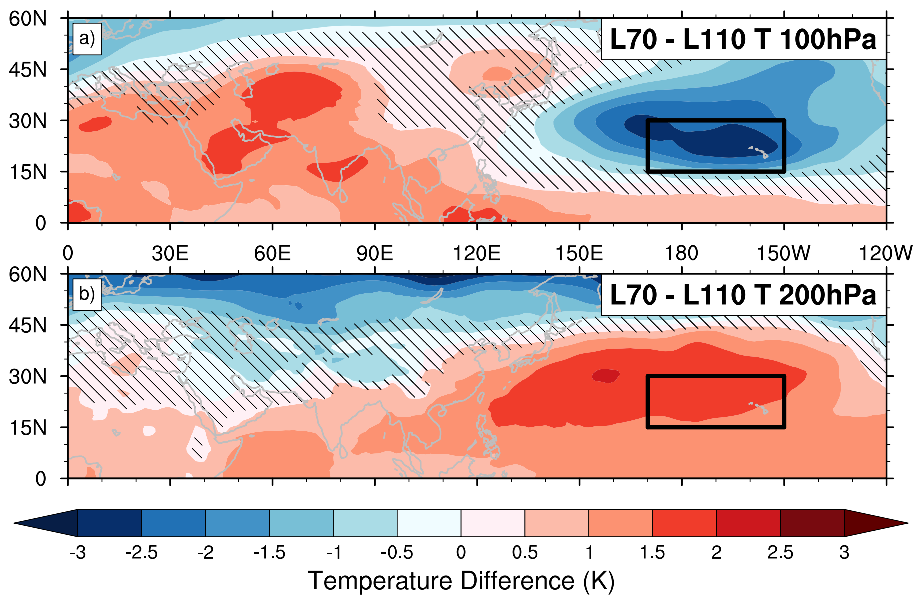


Figure 2.5. Color shadings represent the temperature difference (K) in L70 versus L110 at (a) 100 hPa and (b) 200 hPa from 2005 to 2014. The hatching in the right indicates where the differences are not statistically significant at the 95% confidence level using the Student $t$-test. The black boxes are the same as in Fig. 2.4.

First, we explain the zonal mean temperature difference in the troposphere between L70 and L110 models. To do that, we compare the climatological outgoing longwave radiation (OLR) and pressure velocity ($\omega$) at 445 hPa between the two models. As shown in Fig. A.4, weaker OLR associated with stronger vertical ascent is seen in the western Pacific in L70, indicating that the model with coarser vertical resolution has stronger convective activities. Richter et al. (2014) also documented that the model with higher vertical resolution can reduce the positive bias of precipitation over the Asian summer monsoon region. In order to quantify the total diabatic heating (including radiative heating, sensible heating, latent heating and eddy heating flux) released to the environment, the climatological apparent heat source Q1, which is the residual of the heating budget of resolvable variables, is calculated following Eq. 2.1 (Yanai, Esbensen, & Chu, 1973; Yanai & Johnson, 1993; B. Chen, Tung, & Yanai, 2016):

$$\begin{aligned} Q_1 &\equiv c_p(\frac{p}{p_0})^{\kappa}(\frac{\partial\bar{\theta}}{\partial t} + \bar{\mathbf{v}}\cdot\nabla\bar{\theta} + \bar{\omega}\frac{\partial\bar{\theta}}{\partial p}) \\ &= Q_R + L(\bar{c} - \bar{e}) - \nabla\cdot\overline{s'\mathbf{v}'} - \frac{\partial\overline{s'\omega'}}{\partial p} \end{aligned} \tag{2.1}$$

with $\theta$ the potential temperature, $\mathbf{v}$ the horizontal wind, $\kappa$ the ratio of the gas constant $R$ and the specific heat at constant pressure of dry air $c_p$, $\omega$ the pressure velocity and $p_0 = 1000$ hPa; $Q_R$ the radiative heating, $c$ and $e$ the rates of condensation and evaporation per unit mass of air, respectively, $L$ the latent heat of vaporization, $s$ the dry static energy. The over-bar denotes the zonal average and the prime denotes the departure from the zonal mean. As shown in Fig. A.5, the apparent heating averaged over the Pacific Ocean (170°E-170°W) is stronger in the mid-troposphere between 10°N and 20°N due to stronger convective activities in L70. Therefore, the warmer upper-troposphere over the Pacific Ocean can be explained by the stronger heating associated with stronger convective activities in the coarser vertical resolution model.

In stark contrast, relatively stronger cold bias appears in the lower stratosphere in L70 compared with L110 (Fig. 2.6a) and is seen over the Pacific Ocean (Fig. 2.5a). Here, we attribute the cold anomaly in the lower stratosphere in L70 to stronger upwelling (see Fig. A.6). The wave-driven large-scale ascent in the tropical tropopause layer accompanied by adiabatic cooling is considered to play a dominant role in driving the lower-stratospheric temperature. The upwelling is forced by both the extra-

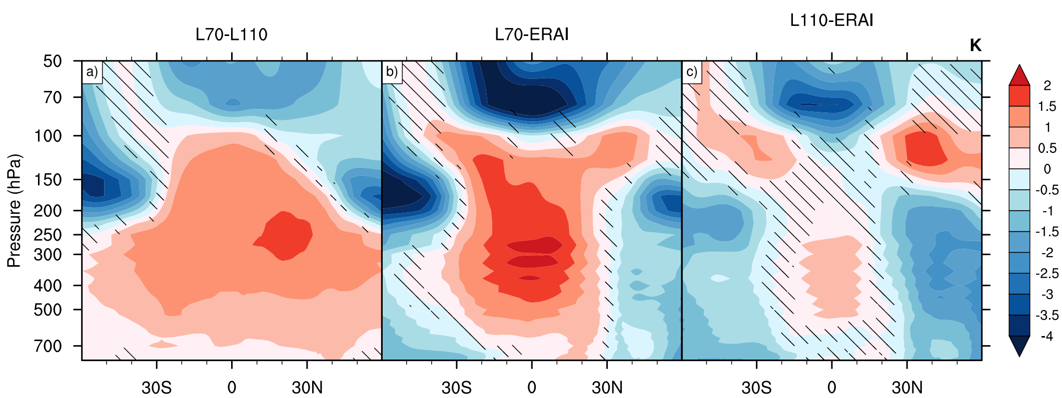


Figure 2.6. Zonal mean temperature difference (K) in (a) L70 and L110, (b) L70 and ERAI and (c) L110 and ERAI. The hatching is the same as in Fig. 2.5.

tropical and tropical waves (Randel & Jensen, 2013). Extra-tropical stratospheric pumping and downward control mechanism associated with wave dissipation in the subtropics could induce an upwelling in the tropical lower stratosphere (Haynes, McIntyre, Shepherd, Marks, & Shine, 1991; Reid & Gage, 1996; Plumb & Eluszkiewicz, 1999; Garcia & Randel, 2008; Taguchi, 2009; G. Chen & Sun, 2011; Garny, Dameris, Randel, Bodeker, & Deckert, 2011; Randel & Jensen, 2013), and the dissipation of waves is proportional to the strength of the zonal mean zonal wind (Andrews, Holton, & Leovy, 1987; Calvo, Garcia, Randel, & Marsh, 2010). Fig. 2.7a shows the differences in zonal mean zonal wind in the two models and L70 has a stronger (∼2m/s) and slightly equatorward shifted subtropical jet compared with L110. This is consistent with the larger meridional temperature gradient in the tropics (Fig. 2.6a) and also the overall larger SWV (Maycock et al., 2013) in L70. Compared with ERAI, there is an overall westerly bias prevailing in the UTLS in both model simulations but it becomes reduced in the L110 (see Fig. 2.7b and Fig. 2.7c).

To explain the difference in stratospheric temperature between L70 and L110, we calculate the transformed Eulerian mean (TEM) vertical velocity $\bar{w}^*$ using monthly variables following Eq. 2.2 (Andrews et al., 1987):

$$\bar{w}^* = \bar{w} + \frac{1}{acos\phi}\frac{\partial}{\partial\phi}(cos\phi\frac{\overline{v'\theta'}}{\bar{\theta}_z}) \tag{2.2}$$

where $w$ is the log-pressure vertical velocity converted from pressure velocity $\omega$, $a$ is the radius of the earth, and $\phi$ is the latitude. Fig. A.6 shows the vertical residual velocity $\bar{w}^*$ difference between L70 and L110. The tropical ascent and extratropical descent can be seen in L110 climatology. In L70, there is an anomalous ascent in the tropics in general, likely due to enhanced subtropical jet, which contributes to the cold anomaly in the lower stratosphere (Andrews et al., 1987; Calvo et al., 2010). Besides, several other processes might also contribute to the increased ascent in L70. The intensification of both Rossby wave-driven and the equatorial wave-driven upwelling associated with the enhanced convective heating could contribute to the stronger mean ascent in the UTLS in L70 (Boehm & Lee, 2003; Norton, 2006; Ryu & Lee,

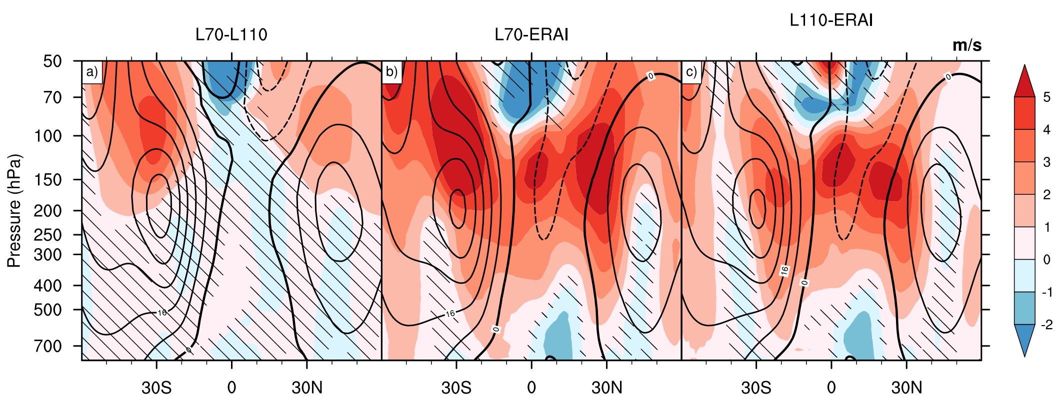


Figure 2.7. Difference in zonal mean zonal wind (m/s, color shading) between (a) L70 versus L110, (b) L70 versus ERAI and (c) L110 versus ERAI, respectively. The black contours with contour interval of 8 m/s represent the climatological zonal mean zonal wind in L110 in (a), and the zonal mean zonal wind in ERAI in both (b) and (c). Solid contours are for positive values, dashed for negative, and thick solid for zero. The hatching is the same as in Fig. 2.5.

2010). Additionally, the dipole temperature structure is accompanied by an upward shift of the cold point tropopause in coarser vertical resolution model (Abalos et al., 2013), which could also contribute to the anomalous cooling in the lower stratosphere through the difference in the established radiative equilibrium between L70 and L110 (Kuang & Bretherton, 2004). The anomalous adiabatic cooling induced by the enhanced upwelling is compensated by stronger radiative heating in L70 (not shown). Ackerman, Liou, Valero, and Pfister (1988) and Gage et al. (1991) suggested that the presence of ice particles, thin cirrus and aerosols is a possible candidate for the larger heating rate in the lower stratosphere. In L70, we also find more frequent high clouds (not shown), which is likely to balance the anomalous adiabatic cooling induced by upwelling.

**Differences in SWV Magnitude**

Here we use the above analysis of the difference in temperatures between L70 and L110 to explain the difference in the magnitude of SWV. As discussed in the Introduction, (Randel et al., 2015) documented that the dehydration primarily occurs on the equatorial flank of the AMA and more SWV is associated with warmer temperature at 100 hPa. Fig. A.7a, b shows the regression coefficient of the SWV variations in the box region (20°-40°N, 40°-140°E) regressed onto the temperatures at 100 hPa in L70 and L110, respectively. The patterns resemble Figure 8 in Randel et al. (2015) and show a warm temperature anomaly on the equatorward flank of the AMA associated with a wet anomaly of SWV, indicating that both L70 and L110 are able to reproduce the dehydration mechanism. As shown in Fig. 2.5a, the warmer temperature is found in the equatorial flank of the AMA at 100 hPa in L70, which is consistent with the relatively wetter SWV in the domain of interest (see Fig. 2.3).

However, we note here that the warmer temperature over the continent at 100 hPa in L70 is not likely a result of stronger convective activities since a stronger convection is associated with a colder tropopause temperature within the AMA region (M. Park et al., 2007; Randel et al., 2015). Instead, other factors such as difference in vertical resolution with refined GWD parameterizations may play a role.

Additionally, as shown in Fig. 2.5a, large difference in UTLS temperature over the central Pacific Ocean is found between the two models with L70 colder than L110. The evident cold center is collocated with the unrealistic SWV maximum in L70, which rules out the possibility of direct vertical transport from below according to the dehydration mechanism. Instead, we argue that it is the UTLS temperature difference over the Pacific Ocean that plays a critical role in the simulation of the AMA and SWV spatial distribution (to be discussed next).

**Differences in SWV Spatial Distribution**

As shown in Fig. 2.2b, conspicuous wet bias of simulated SWV is found over the central Pacific Ocean in L70 and it is a common model deficiency as found in a suite of WACCM experiments (Fig. A.2b, d and A.3). As shown in the 3-D trajectory runs in Randel and Park (2006), most of the particles released on the isobaric surfaces within the AMA remain inside the domain after several weeks, and a relatively small fraction of particles is transported eastward outside. The AMA associated with the Asian monsoon deep convection has a large dynamical variability (Gill, 1980; Jin & Hoskins, 1995; Popovic & Plumb, 2001), and therefore, it is challenging to locate the north-south boundary of the horizontal transport barrier for UTLS chemical species (Garny & Randel, 2013; Ploeger et al., 2015). For our study, one candidate that likely contributes crucial parts in confining the SWV within the anticyclonic flow, specifically in the east-west boundary, is the UTLS temperature over the central Pacific Ocean.

The mechanism is proposed based on the compensation between the temperature anomaly and the PV anomaly. The negative PV anomaly is commonly used as an indicator for the intensity of the AMA (Randel & Park, 2006; Bergman et al., 2013; Garny & Randel, 2013). Small PV gradient inside the AMA indicates that the air is well mixed. Previous studies have emphasized the importance of the strong PV gradient at the edge of the AMA on suppressing the cross-gradient advection and characterizing the horizontal transport barrier (Ploeger et al., 2015). Composite analyses using ERAI reanalysis are conducted here in order to illustrate the linkage between the temperature and PV gradient.

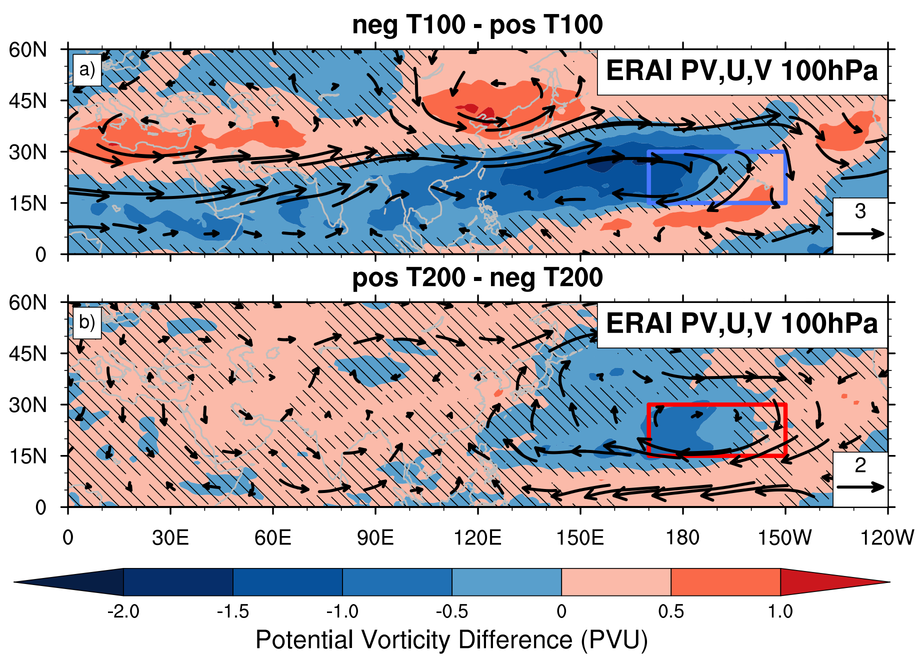


Figure 2.8. Difference in the composited 100 hPa PV (color shadings) and winds (m/s; vectors) for the temperatures averaged in the box (15°-30°N, 170°E-170°W) above the central Pacific for (a) cold and warm temperature days at 100 hPa and (b) warm and cold temperature days at 200 hPa. The hatching is the same as in Fig. 2.5.

As discussed in Section 2.3.2, conspicuous temperature differences are found over the central Pacific region (15°-30°N, 170°E-170°W) in the UTLS between L70 and

L110 with different signs at 100 hPa and 200 hPa. First, we show the linkage between 100/200 hPa temperature anomalies and anomalous PV/winds at 100 hPa using ERAI reanalysis data. Daily temperature and PV from the ERAI reanalysis spanning the range of ten years (from 2005 to 2014) are employed. The monthly data show similar results (not shown here). We define the warm (cold) events as the days when the area-averaged temperature over the noted domain (15°-30°N, 170°E-170°W) is higher (lower) than the ten-year average value during summer months at each pressure level. Our analyses are based on compositing 100 hPa PV for the warm events and cold events at 100 hPa and 200 hPa, respectively. Fig. 2.8a shows the composite difference of 100 hPa PV between the 100 hPa cold and warm events. The sign of the PV anomaly is such that the low PV anomaly expanding eastward occurs in association with the colder than normal central Pacific temperature at 100 hPa with uniformly stronger subtropical westerlies (∼2m/s) and an anticyclonic flow anomaly over the western Pacific Ocean, which is directly analogous to that in L70 (see Fig. 2.9a). It indicates that the relatively colder temperature in L70 at 100hPa compared with L110 is related to the negative PV anomalies. Fig. 2.8b shows the composite difference of 100 hPa PV between the 200 hPa warm and cold events. The anomalous anticyclonic flow and negative PV are found on top of the warm temperature region over the central Pacific and this is analogous to that in L70 as well. Therefore, both the cold bias at 100 hPa and the warm bias at 200 hPa in L70 lead to low PV anomaly extending to the Pacific Ocean, further diminish the PV gradient on the eastern flank of the AMA.

To further quantify the cause of the negative PV anomaly over the Pacific Ocean in L70 compared with L110, we decompose the PV difference into the contributions due to stratification difference and due to relative vorticity difference as follows (Wu & Shaw, 2016):

$$\delta PV \approx \underbrace{-g(f+\zeta)\delta(\frac{\partial\theta}{\partial p})}_{\text{stratification difference}} \quad \underbrace{-g\delta(f+\zeta)(\frac{\partial\theta}{\partial p})}_{\text{relative vorticity difference}} \tag{2.3}$$

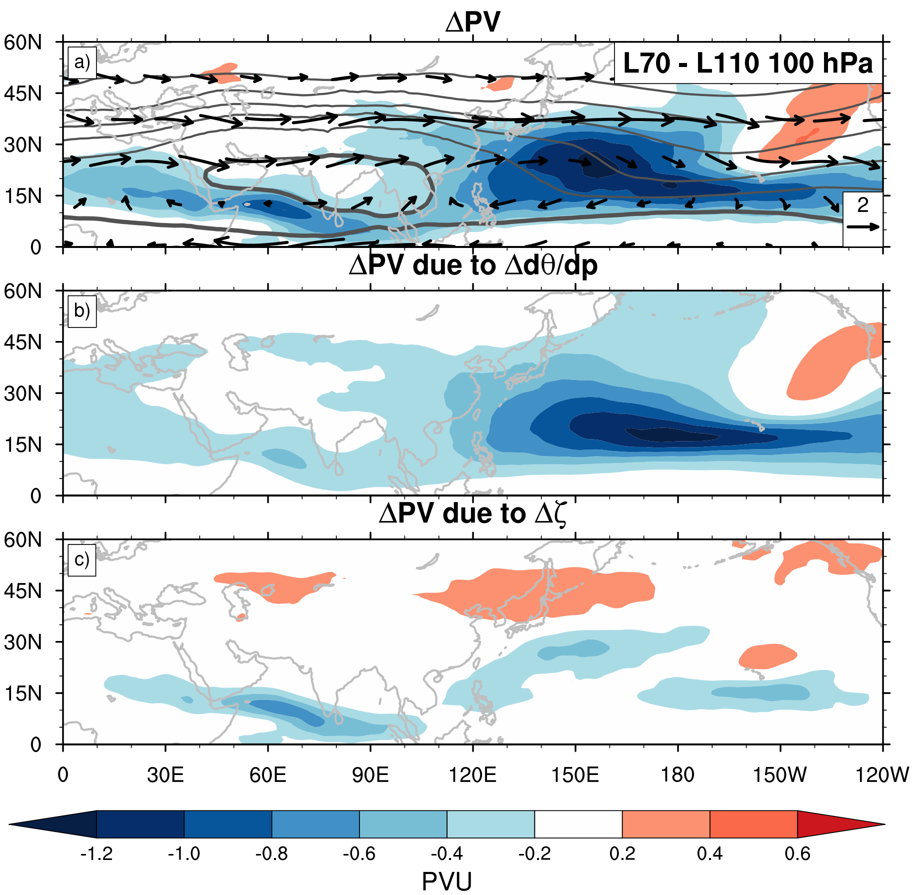


Figure 2.9. (a) Difference of PV (color shadings) and winds (m/s; vectors) between L70 and L110 at 100 hPa. The gray contours represent the climatological PV in L110 (contour interval: 2PVU). The thick gray line indicates 2PVU surface. The decomposition of the PV difference (L70 minus L110) into the contributions (b) due to the difference in stratification [i.e., $-g(f+\zeta)\delta(\frac{\partial\theta}{\partial p})$] and (c) due to the difference in horizontal circulation [i.e., $-g\delta(f+\zeta)(\frac{\partial\theta}{\partial p})$].

where $\delta$ indicates the difference between the L70 and L110, $g$ is the gravitational acceleration, $f$ is the Coriolis parameter and $\zeta$ is the relative vorticity. The sum of the decomposition following the right-hand-side of Eq. 2.3 is about equal to the left-hand-side (not shown). Compared with L110, L70 has a negative PV anomaly over the central Pacific Ocean (Fig. 2.9a). We find that, in L70, both the less stratified UTLS (Fig. 2.9b) and, to a lesser extent, the anomalously anticyclonic circulation (Fig. 2.9c) contribute to the negative PV anomaly over the Pacific Ocean and result in a relatively weaker PV gradient on the eastern branch of the AMA (see Fig. 2.9a) and thus a more leaky transport barrier in L70. Since SWV is highly sensitive to temperature, once SWV is extended to the relatively warmer place over the Pacific Ocean as compared with the continent, it tends to stay there, thus the maximum of SWV is seen over the Pacific Ocean in L70.

### 2.3.3 The Simulations of CO over the Asian Summer Monsoon Region

Although this study focuses mostly on the simulations of the SWV, we also evaluate the simulated CO in the two models as complementary evidence. Since both the spatial pattern and magnitude of CO are less dependable on the temperature fields, it is highly controlled by the large-scale circulation. Overall, L70 and L110 are able to reproduce the localized maximum embedded within the AMA reasonably well (see Fig. 2.10a and Fig. 2.10b), which is consistent with the work by Pan et al. (2016), who examined the variability of CO and its linkage to the AMA in SD-WACCM4. However, compared with the simulation in L110, in L70, CO is not well isolated within the AMA and leaks out from the southeastern Asia to the central Pacific in the subtropics (see Fig. 2.10c), which is highly collocated with the PV anomaly (shown in Fig. 2.9a). But L70 has a more reasonable simulation of CO compared to water vapor, likely due to its less dependence in the UTLS temperature and relatively shorter lifetime. Therefore, we confirm that the UTLS temperature anomalies

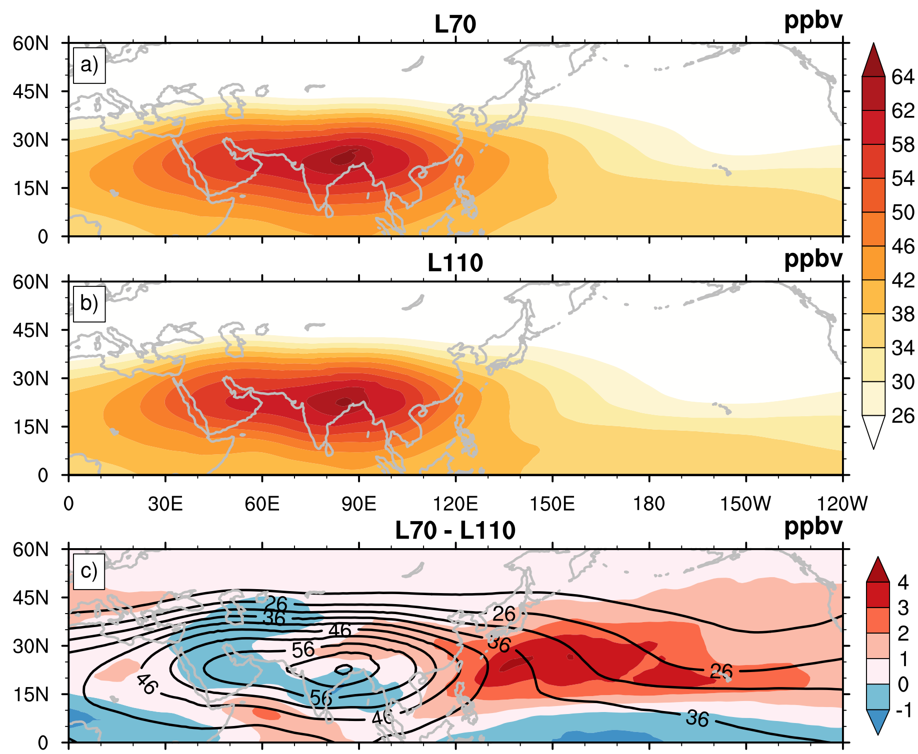


Figure 2.10. The colors show the summertime horizontal structures of CO (ppbv) from (a) 103 hPa L70 and (b) 102 hPa L110 averaged over 1979 to 2014. (c) Colors show the CO difference (ppbv) between L70 and L110 with CO in L110 (black contours).

over the central Pacific are responsible for the model deficiency in the confinement of chemical constituents in L70.

## 2.4 Summary and Discussion

Our primary purpose of this study has been to examine the model performance in the simulation of SWV associated with the Asian summer monsoon and whether model vertical resolution affects the representation of SWV. We have found that the maximum of the simulated SWV is located over the central Pacific Ocean in most of the WACCM configurations, instead of over the Asian continent as in the MLS retrievals. The high vertical resolution model L110 with refined GWD parameterization, though displaying a dry bias on the poleward side, corrects the deficiency with SWV confined within the AMA and maximized over the continent.

Our results indicate that the temperature over the central Pacific Ocean is a significant factor in the representation of the Asian monsoon characters in the UTLS. We find that one of the improvements with increased vertical resolution and refined GWD parameterization lies in resolving the UTLS temperature more accurately, which is consistent with Richter et al. (2014). The relatively stronger convection in L70 likely contributes to the warmer troposphere-cooler stratosphere dipole pattern. L110 with higher vertical resolution and refined GWD is capable of alleviating the cold bias above and the warm bias below 100 hPa over the central Pacific Ocean, and therefore simulates a steepened PV gradient over the central Pacific Ocean that better closes the upper-level anticyclone and confines the SWV within the enhanced transport barrier.

Before concluding, possible caveats have to be noted. First, although L110 corrects the cold anomaly over the central Pacific Ocean, we didn't explicitly address why but suspect that it's related to the stronger ascent occurring over the central Pacific Ocean. The observational evidence of the upward motion in the lower stratosphere occurring over central Pacific Ocean is documented in Gage et al. (1991). Second, the purpose of this study is to make use of the model experiments that are available and have a clean pair of low and high vertical resolution versions to examine the model performance of simulating SWV. However, to further test the robustness of the mechanism proposed in this study, we plan to extend the analysis to an ensemble of models that participated in the CCMI experiments in future work.

Previous studies have focused on the westward eddy shedding of the AMA and its role in chemical transport (Popovic & Plumb, 2001; Garny & Randel, 2016). Different from previous studies, our work emphasizes the importance of the eastern branch of the AMA in the confinement of chemical transport and the necessity to improve the representation of that in climate models. Despite the difference in simulated convection, it is the increased vertical resolution and refined GWD parameterization that improve the representation of the UTLS temperature and thus the anticyclone dynamics and SWV. The overall results demonstrate that models in general have biases in simulating SWV, which is likely associated with stronger westerlies and weaker PV gradient in the NH subtropics. Our results demonstrate that model version with increased vertical resolution is able to correct these biases.

# 3. FAST TRANSPORT PATHWAYS INTO THE NORTH AMERICAN UPPER TROPOSPHERE AND LOWER STRATOSPHERE AS AN INTERPLAY BETWEEN DEEP CONVECTION AND THE LARGE-SCALE CIRCULATION

A version of this chapter has been submitted to Geophysical Research Letters.

## 3.1 Introduction

Observations and model studies have shown that the summer monsoon circulation is an effective gateway of tropospheric air into the stratosphere (Randel et al., 2010; Vogel et al., 2019; Wu et al., 2020). Transport via the Asian and North American (NA) monsoons influences the composition of the upper troposphere and lower stratosphere (UTLS), which in turn directly impacts the stratospheric chemistry and global radiative forcing (S. Solomon et al., 2011; Yu et al., 2015; Anderson et al., 2017; Clapp & Anderson, 2019). Despite consensus on the pronounced monsoonal signals in both Asian and NA UTLS, the characteristics of monsoon-related troposphere-to-stratosphere transport and the underlying dynamics remain topics of active research.

The Asian summer monsoon (ASM) related transport mainly consists of rapid uplifting from the surface to the convective outflow level by deep convections and typhoons, coupled with subsequent ascent and horizontal confinement by the large-scale ASM anticyclone in the UTLS (Gettelman et al., 2002; M. Park et al., 2007, 2008, 2009; Vogel et al., 2014; Pan et al., 2016). Recently, Wu et al. (2020) complemented previous studies and examined transport pathways linking the surface to the UTLS using an idealized pulse passive tracer approach to reveal the transport dynamics. Fast transport paths were identified over the southern slope of the Tibetan Plateau, northern India, and Saudi Arabia with a modal age of 5-10 days. They demonstrated that the vertical eddy flux controls the transport at 100-150 hPa while convective processes dominate around 200-300 hPa. The modal timescale for transport ranges from 3 days to a month across various studies (B. Chen, Xu, Yang, & Zhao, 2012; Bergman et al., 2013; Orbe, Waugh, & Newman, 2015; Tissier & Legras, 2016; Wu et al., 2020).

The NA UTLS exhibits similarities as well as differences with its Asian counterpart during summer. For instance, comparable stratospheric water vapor maxima are observed over both monsoon regions, however, the isotopic composition differs with enriched $\delta$D above North America but not over Asia (Randel et al., 2012). A localized aerosol layer is found above NA monsoon, but its calculated composition is different than that of the Asian tropopause aerosol layer (Yu et al., 2015). Because of the very different topography, convection and large-scale circulations in the two regions, it is likely that the transport characteristics related to the North American summer monsoon (NASM) behave differently than those in Asia. While much progress has been made in understanding transport via the ASM during the past decades, studies on transport into the NA UTLS remain comparatively limited. There are several mechanisms that may be responsible for the NA UTLS transport. Throughout the year, air gradually ascends into the stratosphere from the tropical upper troposphere, and then moves towards higher latitudes due to horizontal eddy transport (Vaughan & Timmis, 1998; Highwood & Hoskins, 1998; Fueglistaler, Wernli, & Peter, 2004; Fueglistaler et al., 2009; Abalos et al., 2013). In July and August, the NA UTLS is dominated by a semi-permanent anticyclone near 30°N, 110°W, owing to a Matsuno-Gill type response to the diabatic heating in the tropics and subtropics (Gill, 1980; Siu & Bowman, 2019). This large-scale anticyclone plays an important role in controlling a range of chemical species in the NA UTLS (Weinstock et al., 2007; Froyd et al., 2009; S. Solomon et al., 2011; Thomason & Vernier, 2013; Yu et al., 2015; Randel et al., 2015) and in increasing the residence time of air over the United States (Koby, 2016). In addition to the NASM convection that is primarily located south of 30°N, overshooting storms become active in the contiguous United States, primarily over the north-central Great Plains, which may hydrate the UTLS (Dessler & Sherwood, 2004; D. L. Solomon, Bowman, & Homeyer, 2016; J. B. Smith et al., 2017; Cooney et al., 2018). However, a substantial fraction of moist air parcels at 100 hPa in the 20°N-40°N latitudinal range cannot be explained by nearby deep convection (Sun & Huang, 2015). Therefore, an investigation of the relative contributions due to distinct mechanisms and their transport timescales into the NA UTLS is needed to interpret observations and improve the model performance in simulating processes in the UTLS.

In this study, we focus on the most efficient route connecting the Northern Hemisphere (NH) surface and the NA UTLS due to its implication for transporting short-lived trace gas pollutants which can deplete stratospheric ozone (Levine, Braesicke, Harris, Savage, & Pyle, 2007; Hossaini et al., 2015). Specifically, we aim to address three questions: (1). Are there relatively efficient pathways for transport from the boundary layer into the NA UTLS during summer? (2). What is the timescale for the fast transport? (3). What is the dynamical mechanism? To isolate the role of dynamics from other factors such as lower tropospheric chemistry and surface emissions, we apply the idealized pulse passive tracer approach (to be discussed later) and use the same model experiment as in Wu et al. (2020). The numerical model experiment and diagnostics will be described in the following section.

## 3.2 Methods

We apply the "Boundary Impulse Response (BIR)", or known as the pulse tracer approach to diagnose transport characteristics linking the NH surface to the North American UTLS. This approach has been commonly used to study the atmospheric transport (Orbe, Holzer, & Polvani, 2012; Orbe, Holzer, Polvani, & Waugh, 2013; Orbe, Waugh, Newman, & Steenrod, 2016). Specifically, BIR of a location contains information on the distribution of times since a pulse of passive tracer, constituting as air masses released from source region, last contacts the NH surface. The Green's function or distribution of transit times captures all possible pathways connecting the source region and the receptor surface, and allows us to identify the most efficient route. The diagnostics are performed with the Whole Atmosphere Community Climate Model version 5 (WACCM5) in atmosphere-only mode. The model resolution is 0.95° latitude × 1.25° longitude (∼100 km) with 110 pressure layers (∼0.5 km spacing above the boundary layer and in the lower stratosphere). Hereafter we refer to this model as WACCM5-L110. Deep convection is treated by G. J. Zhang and McFarlane (1995) with improved convective momentum transport (Richter & Rasch, 2008; Tilmes et al., 2016) and shallow convection is treated by S. Park and Bretherton (2009). WACCM5-L110 includes a number of improvements to standard WACCM configuration. X. Wang et al. (2018) reported that simulations by this model agree well with reanalysis data and observations with regard to the wind and temperature climatologies as well as stratospheric water vapor distribution. Further information on WACCM5-L110 is summarized in Garcia and Richter (2019).

Our tracer implementation is identical to that presented in Wu et al. (2020). Specifically, the pulse tracer is released at the boundary layer over the entire NH with concentration being set to 1 mol/mol only during the first day. The passive tracer has no specific sources and sinks. Its concentration is set to zero whenever the tracer is in contact with the surface again after its release. The transport of tracer is driven by both resolved and parameterized processes in the model. For each summer, we implement 10 tracers and release them on different days, that is, on 3, 10, 17, 24, and 31 July and 3, 10, 17, 24, and 31 August, respectively, to explicitly assess how the transport properties vary with synoptic variability of the monsoonal system. We examine statistics from 90 tracers, that is, nine-year simulations. The model is integrated from January 1981 to December 1994 with prescribed sea surface temperatures and sea ice.

What processes account for the fast transport from the NH surface to the NA UTLS? To evaluate this we turn to the tracer budget as follows:

$$\frac{\partial T_x}{\partial t} = TAT_x + VDT_x + TCOND\_T_x + TCONS\_T_x, \tag{3.1}$$

with $T_x$ the pulse tracer, corresponding to the mass fraction of air that had last contact with NH surface at any time in the past, $TAT_x$, $VDT_x$, $TCOND\_T_x$, and $TCONS\_T_x$ the transport tendency due to the resolved dynamics, vertical diffusion, deep convection, and shallow convection, respectively, which are calculated by the model and saved at daily time step. Tracer budget analysis allows us to disentangle different processes during the transport and assess the influence of each component explicitly. The resolved dynamics term can be further decomposed into horizontal and vertical advection components as follows:

$$TAT_x = \underbrace{-\frac{u}{acos\phi}\frac{\partial T_x}{\partial \lambda} - \frac{v}{a}\frac{\partial T_x}{\partial \phi}}_{\text{horizontal advection}} \quad \underbrace{-\omega\frac{\partial T_x}{\partial p}}_{\text{vertical advection}} \quad , \tag{3.2}$$

where $u, v, \omega$ denote the zonal velocity, meridional velocity, and vertical velocity in pressure coordinates, respectively. $p$ denotes the pressure value. $a$ is the radius of the earth. $\phi$ and $\lambda$ are the latitude and longitude, respectively.

## 3.3 Results

To characterize transport timescales from the surface into the NA UTLS, we analyze the daily evolution of the 90 tracers averaged over the box defined by 10°N-40°N and 140°W-60°W at 110 hPa (see Figure 3.1a). The tropopause height is typically located above 150 hPa over the NASM region during July and August months (see Figure A.8). Pressure level of 110 hPa is in the range of the UTLS, and analysis on 100 hPa yields similar results (not shown). The boxed region is the same as that in Randel et al. (2015), where maxima in UTLS water vapor are observed. Sorting the peak values of each BIR Green's function, corresponding to the transport modal times, allows us to categorize the "normal" ensemble where the modal age falls between the $10^{th}$ and $90^{th}$ percentile (23-55 days). The black curve is the average of the normal ensembles, peaking on day 40 and decaying slowly. Accordingly, Figure 3.1c shows the composited modal age distribution for these normal ensembles at 110 hPa. The fastest modal times occur above Central America, equatorial Pacific and Atlantic Ocean, on a modal time scale of 14 days to 21 days, respectively. The transport time scale gradually increases toward higher latitudes due to the quasi-horizontal eddy transport by the North American anticyclone (Abalos et al., 2013), similar to the results of ASM region as found in Wu et al. (2020).

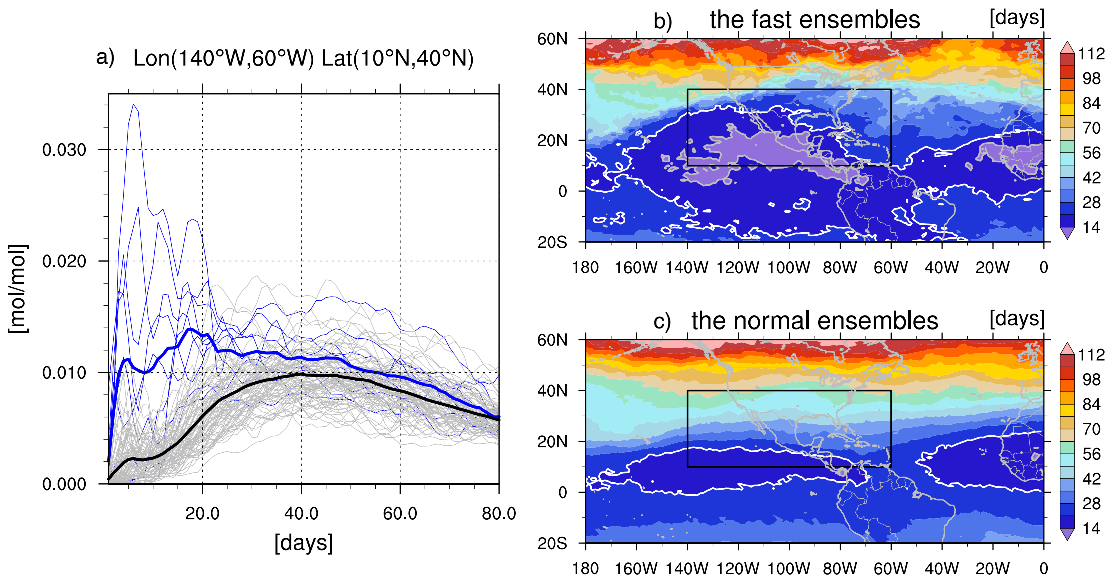


Figure 3.1. (a) Gray lines plot tracer mixing ratio evolution averaged over 10°N-40°N and 140°W-60°W (black-boxed region on the right) at 110 hPa. Blue lines indicate the fast transport ensembles with modal ages below the $10^{th}$ percentile, and the thick blue line is their mean. The thick black line is the mean of normal tracer ensemble whose modal age falls between the $10^{th}$ and $90^{th}$ percentile. (b) shows the averaged modal ages of fast ensemble represented by blue lines in (a). Similarly, (c) shows the averaged modal ages of normal tracer ensemble. Gray and white contours highlight 14 and 21 days of modal age, respectively.

The fast modal ages in Figure 3.1a exhibit a widespread distribution (see also Figure A.9), and a variety of transport pathways is expected. Transit along some paths takes more than 2 months (66 days), while along others it occurs within 3 days. We elaborate on the fastest transport process below. Blue lines in Figure 3.1a highlight the fast ensemble members whose model age falls below the $10^{th}$ percentile, with an ensemble mean with modal age of 17 days. Figure 3.1b shows the composited modal age distribution for the fast ensembles at 110 hPa. The fastest transport pathway shifts northward to 20°N and occurs above the eastern Pacific and the Gulf of Mexico, with a regional modal age of 14 days.

We now examine the day-to-day evolution of the fast ensembles compared to the normal ensembles by evaluating the average BIR during different periods, that is, over 1-2, 3-5, 6-8, and 9-14 days after the first day of release. Figure 3.2 displays the ensemble mean tracer concentration differences between the fast and normal cases at 110 hPa, at 25°N, and in zonal mean between 140°W-60°W. During days 1-2, very rapid and strong uplift of tracers into the NA UTLS region occurs preferentially over the Gulf of Mexico and the eastern Pacific. During days 3-5, a substantial increase is seen above the northwest Mexico. In addition to vertical transport by deep plumes near 90°W, 20°N, horizontal advection can be seen in both zonal and meridional directions. Tracers are transported westward and equatorward, especially in the upper troposphere. During days 6-8, tracers are advected northeastward and maximize above the subtropical eastern Pacific and the Gulf of California. During days 9-14, tracers are separated from the tropics, and are confined above the southern United States. However, for normal ensembles, there is nearly indistinguishable tracer enhancement above the North American Southwest. The vast majority of tracers arrives the UTLS in the Western Hemisphere near 10°N, especially above the northern Africa.

Tracer budget analyses are used to examine the contributions from individual processes following Eq. 3.1 averaged over the boxed region 10°N-40°N and 140°W-60°W. To obtain a general picture, we calculate and plot the vertical profiles of the relative contribution of each term using the average of 90 BIR tracers during the first week (see Figure A.10). In fact, calculations composited for the fast and normal ensembles yield profiles with comparable amplitude peaks throughout the atmosphere (not

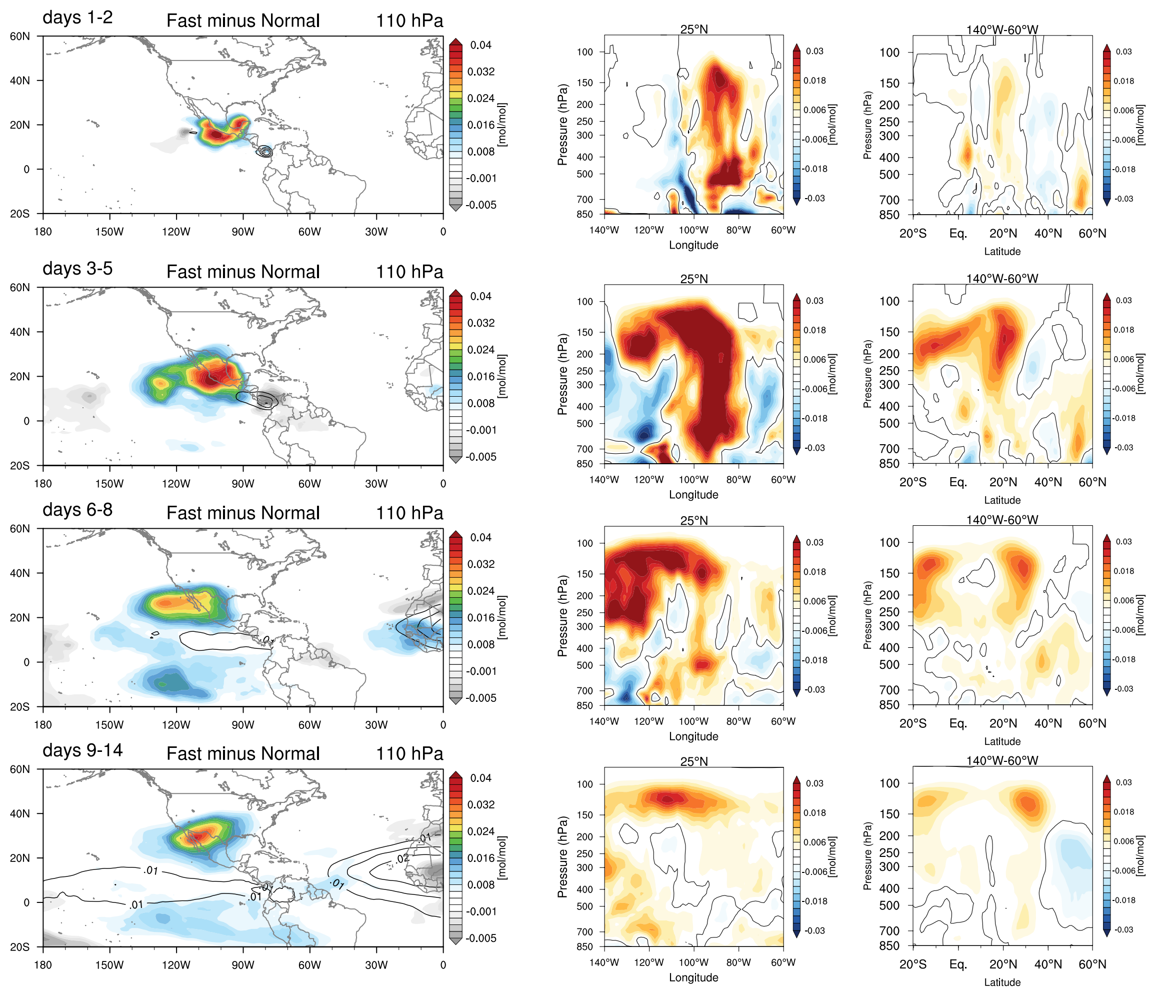


Figure 3.2. Color shadings are tracer evolution differences between the fast and the normal ensemble at 110 hPa (left column), the vertical-longitudinal cross sections at 25°N (middle column), and the vertical-latitudinal cross-sections averaged between 140°W and 60°W (right column) during days 1-2 (first row), days 3-5 (second row), days 6-8 (third row), and days 9-14 (fourth row). The units are mol/mol. Black contours in the left column denote the averaged tracer concentrations of the normal ensembles while denote the zero contour lines in the middle and right columns.

shown). The transport tendency in the mid-to-upper troposphere, especially from 400 hPa to 300 hPa, is largely attributed to the nearby deep convection, and partly by the resolved dynamics. The shallow convection-driven and vertical diffusion-driven transport processes are relatively weaker. Above 300 hPa, the contribution due to deep convection decreases rapidly with altitudes where the resolved dynamics-driven transport takes over, together with vertical diffusion to a lesser extent. The Costa Rica Aura Validation Experiment campaign has observed a sharp drop in aerosol composition at 200 hPa, which is linked to the abrupt decrease of convective influence (Froyd et al., 2009). Coherent behaviors are also seen in another artificial tracer study based on e90 [Figure 11c in Abalos, Randel, Kinnison, and Garcia (2017)]. Overall, both deep convection and resolved dynamics play principal roles in transport into the NA UTLS region, consistent with the processes of its Asian counterpart (Wu et al., 2020). More precisely, while the deep convection determines the gradient of tracer concentrations at the bottom of the UTLS, the resolved large-scale circulation governs the transport further upward.

The leading mechanisms responsible for the fast transport into the NA UTLS are evaluated by contrasting to conditions of the normal ensembles. Because the difference in area-averaged convective transport ($TCOND\_T_x$) is most pronounced at 200 hPa during the first two days (not shown), we first show the horizontal distribution of the composited 200 hPa $TCOND\_T_x$ for the fast ensembles, normal ensembles, and their differences, respectively, in the left column of Figure 3.3. For normal ensembles, the deep convection-driven transport tendency shows a localized maximum between 0°N-10°N, consistent with the observed heaviest precipitation in tropical Central America and the northern part of South America (Randel et al., 2015; Siu & Bowman, 2019). In contrast to the climatological maxima of tracer transport in the tropics, stronger positive tendency due to deep convection is found north of 15°N in the fast ensembles, clustering around the Gulf of Mexico, northwestern Mexico (i.e., Sierra Madre Occidental), and southern Mexico (i.e., southwest slope of Sierra Madre del Sur). Meanwhile, there is anomalously weak transport tendency along the Great

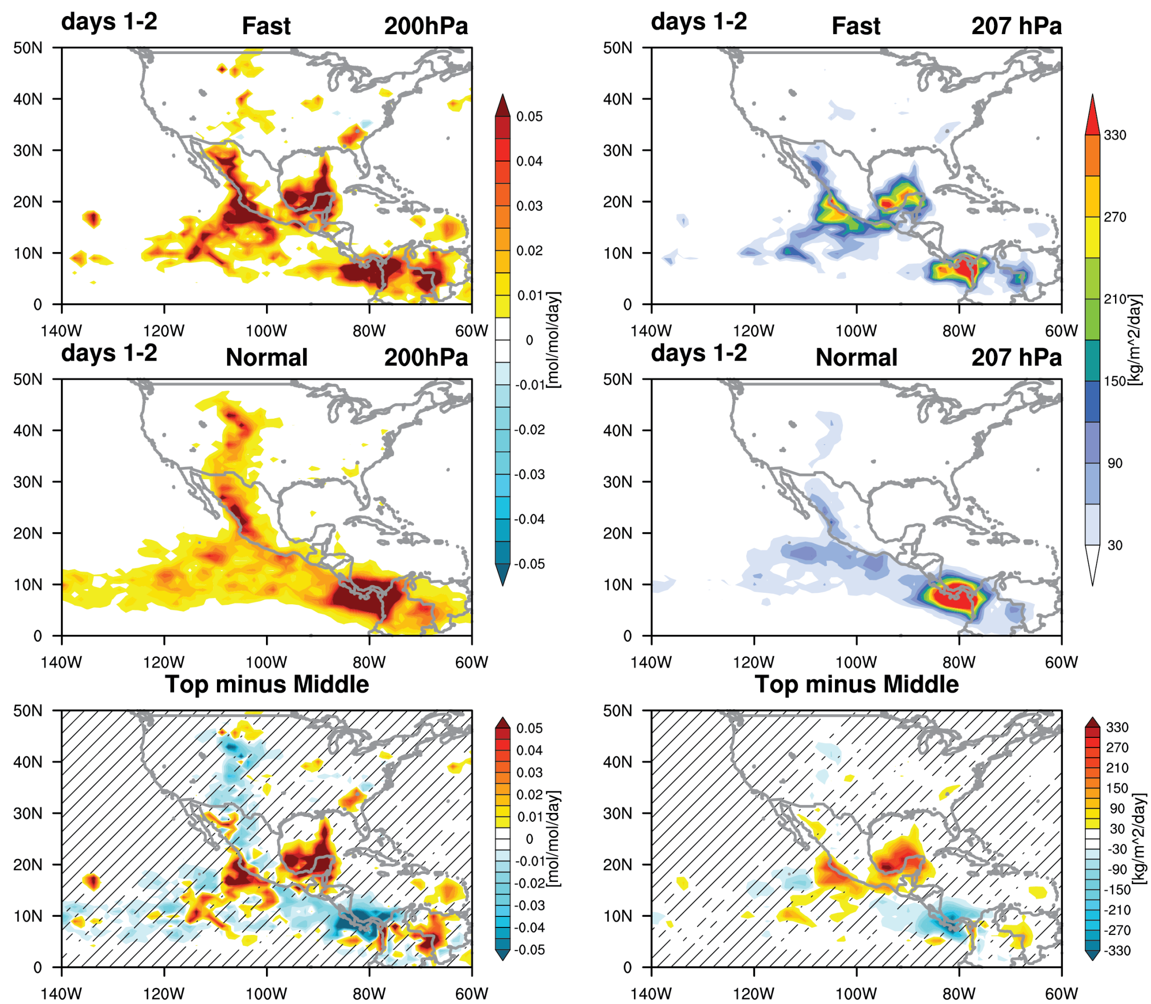


Figure 3.3. Left panels show deep convection-driven transport tendency at 200 hPa for the fast ensembles (top row), the normal ensembles (middle row), and their difference (bottom row) in days 1-2. Right panels show the composited convective mass flux from Zhang-McFarlane (ZM) scheme ($kg/m^2/day$) at 207 hPa for the fast ensembles (top row), the normal ensembles (middle row), and their difference (bottom row) in days 1-2. The hatching denotes the region where the differences are not statistically significant at the 95% confidence level using the bootstrap method.

Plains in the fast ensembles compared to the normal. The convection driven transport tendency becomes weak and statistically insignificant from the third day (not shown). In addition, we also examine the convective mass flux from Zhang-McFarlane (ZM) scheme, which is the direct measure of convective transport, to confirm our findings. Coherent patterns of convective mass flux around 200 hPa are evident on the right column of Figure 3.3, that is, the large positive transport tendency is collocated with stronger convection over the Gulf of Mexico and the eastern Pacific. Vertical cross section of the composited convective mass flux averaged between 140°W-60°W (Figure A.11) shows intensified convection ranging from 20°N to 30°N whereas weaker convection over the U.S. continent from 30°N to 45°N during the fast transport.

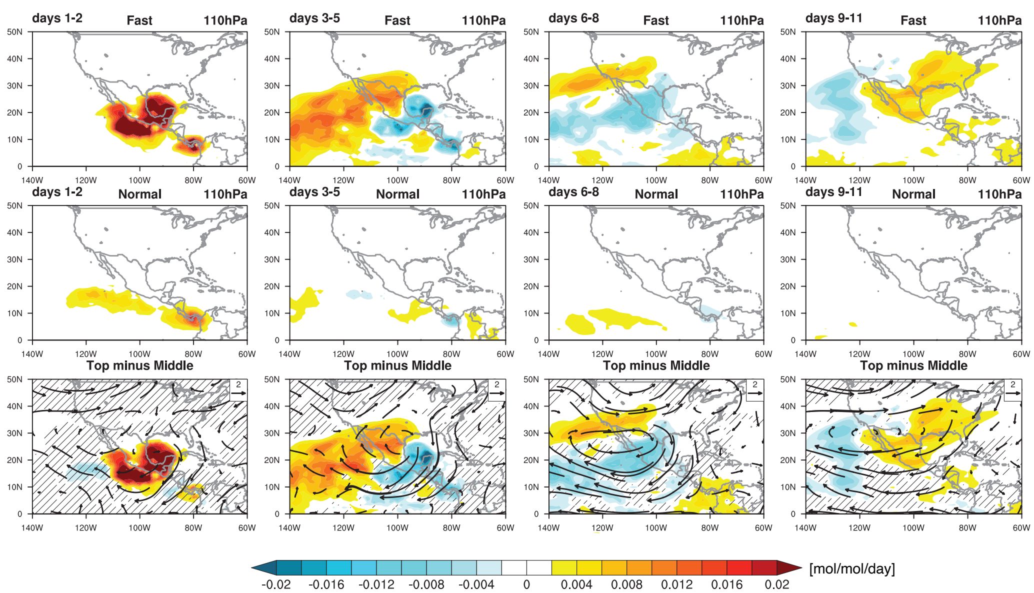


Figure 3.4. Resolved dynamics-driven transport tendency at 110 hPa for the fast ensembles (first row), the normal ensembles (second row), and their differences (third row) in days 1-2 (first column), days 3-5 (second column), days 6-8 (third column), and days 9-11 (fourth column). The vectors in the third row are horizontal wind differences between the fast and the normal ensembles. The hatching is the same as in Figure 3.3.

Evolution of the resolved dynamics-driven transport at 110 hPa is highlighted in Figure 3.4, comparing the fast and normal ensembles. For days 1-2, strong transport tendency occurs above the Gulf of Mexico and the west coast of Mexico, collocated with increased tracer concentration at 110 hPa in Figure 3.2. During days 3-5 westward movement of the tracers increases tendencies over the subtropical Pacific Ocean, linked to anomalously strong UTLS anticyclonic circulation. This behavior continues over days 6-8, contributing to tracer increases along the eastern Pacific at 30°N and reaching the southwestern U.S. continent, which is in agreement with the northward shift of the tracer concentration (Figure 3.2). Over days 9-11, widespread positive tendency occurs above the southeastern U.S. continent and Mexico. In comparison, the tracer tendency due to resolved circulation for the normal ensembles is much weaker in the subtropics during the first two weeks (Figure 3.4, middle row). The bottom panel of Figure 3.4 shows the $TAT_x$ difference between the top and middle panels and the superimposed vectors are the horizontal wind difference accordingly. The differences highlight a persistent anomalous anticyclonic circulation over the southern U.S. continent during the first two weeks, consistent with the horizontal tracer transport over the U.S. This is an important component of the systematic fast transport pathways ending over the continental U.S. We further decompose the resolved dynamics term related to the fast transport into vertical and horizontal components following Eq. 3.2 (see Figure A.12). During the first two weeks, persistent positive transport tendency due to the vertical advection appears above the Gulf of Mexico and the eastern Pacific, constantly uplifting the tracers to 110 hPa via these regions. But this is largely compensated by negative contribution due to the horizontal advection, which transports the tracers towards the continental U.S. via the intensified upper-level anticyclone.

To summarize the mechanism resulting in the fast transport, Figure 3.5 shows the vertical structure of composite differences between the fast and normal ensembles for temperature, meridional wind, and vertical motion averaged over the latitudinal band of 10°N to 40°N. The latent heat released by the stronger than normal convection in 20°N-30°N latitudes (i.e., the Gulf of Mexico and the eastern Pacific; Figure 3.3) leads to an intensified upward transport extending into the UTLS region and a warm anomaly in the tropospheric column. In response to the stronger convective forcing, the upper level anticyclonic circulation is strengthened above the southern U.S. The strong ascent (descent) is coupled with increased northerly (southerly) in the UTLS via Sverdrup balance; that is, $\beta v \approx f(\partial\omega/\partial p)$, where $f$ is the Coriolis parameter and $\beta$ is its meridional gradient (Gill, 1980; Garny & Randel, 2013; Wu & Shaw, 2016; Siu & Bowman, 2019). The net effect is that tracers are efficiently advected upward and then are confined and circulated by the intensified anticyclone associated with stronger subtropical convection.

### 3.4 Conclusion

In this study, we employ the pulse passive tracer approach implemented in WACCM5-L110 to study transport processes connecting the NH boundary layer to the NA UTLS during summer months. Understanding transport paths and associated transit times are important in interpreting and modeling the behavior of chemical species in the UTLS. We focus on the fast pathway due to its potential for uplifting very short-lived ozone depleting substances into the lower stratosphere. In addition, we explicitly evaluate the budget of the pulse tracers to investigate the leading mechanism for the fast transport.

We show that the majority of tracers enters the NA UTLS via Central America, tropical Pacific and Atlantic Ocean on modal time scale of 40 days. However, efficient transport pathways can be found in some tracer ensembles occurring over the Gulf of Mexico and the eastern Pacific. These fast ensembles, defined as transport cases whose model ages fall below the $10^{th}$ percentile, are on modal time scale of 17 days. For the fast transport into the NA UTLS, the origin is enhanced deep convection over the Gulf of Mexico and the eastern Pacific, not locally over the U.S continent. Convective transport occurs from the boundary layer to ~200 hPa. Then strong vertical advection further uplifts the tracers to the UTLS region where the intensified anticyclone takes over by circulating the tracers towards the southern U.S. continent. The

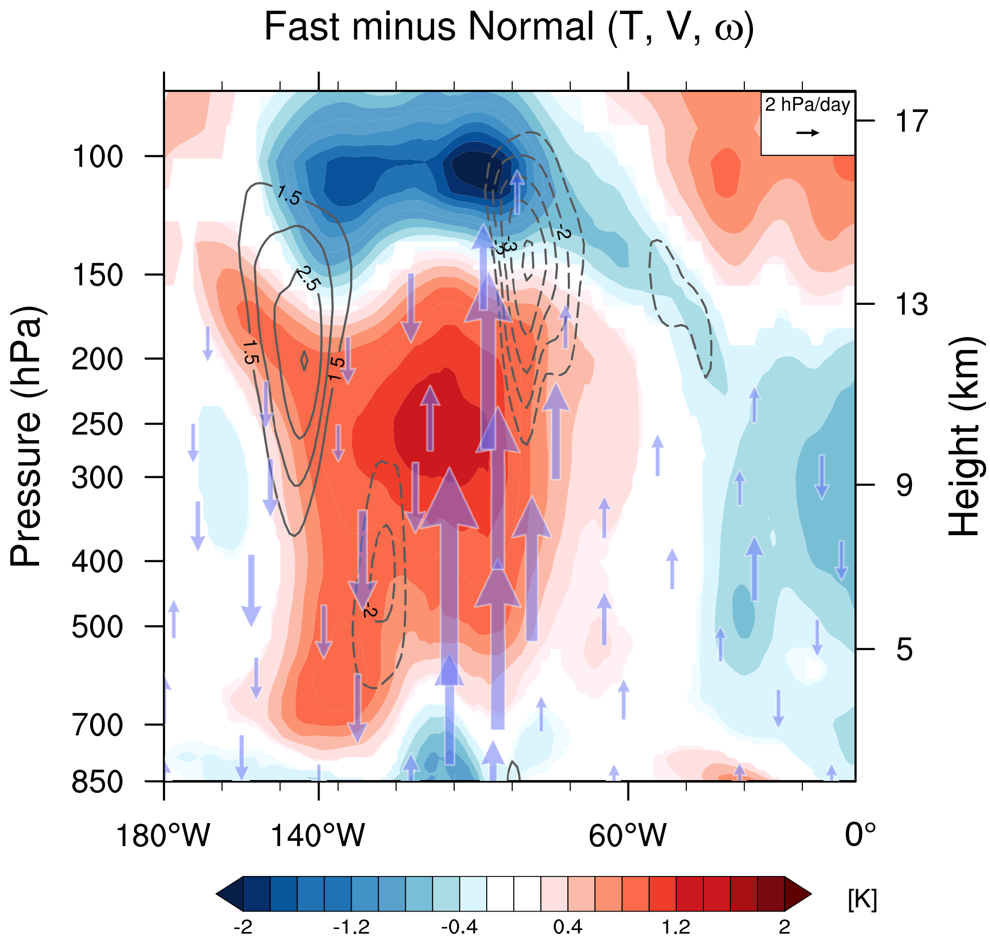


Figure 3.5. The composited differences between the fast and the normal ensemble for temperature (K, shaded), meridional winds (in contour with 1 m/s interval), and vertical velocities $\omega$ (hPa/day, in arrow). Variables are averaged between 10°N and 40°N during days 1-14. Regions where temperature differences are not significant at the 95% level using the bootstrap method are shaded white.

large-scale circulation in the UTLS is amplified as a response to enhanced convection forcing at lower levels via Sverdrup balance. Future work will explore the sensitivity of these results to model's representation of convection.

Case studies show that the northwestern Pacific tropical cyclones affect the chemical composition in the vicinity of the Asian monsoon anticyclone (Vogel et al., 2014; D. Li et al., 2017). However, we doubt that the fast transport pathway identified here is related to tropical cyclones since no coherent warm cyclonic centers were found during these cases (not shown). Overall, our results demonstrate the importance of interaction between deep convection and resolved dynamics in rapid uplifting of the tracer into the NA UTLS region and have important implications for understanding the chemical constituents in NA UTLS.

# 4. STRATOSPHERIC CONTRIBUTION TO THE SUMMERTIME HIGH SURFACE OZONE EVENTS OVER THE WESTERN UNITED STATES

The work contained in this chapter has been published in Environmental Research Letters.

## 4.1 Introduction

Surface ozone ($O_3$) adversely affects human health and the ecosystem because of its high oxidation capability (U.S. Environmental Protection Agency, 2015). The risk of $O_3$ pollution on mortality is also significantly raised by high temperatures (Levy & Patz, 2015). During summer, surface $O_3$ level maximizes over the western U.S. (Gaudel et al., 2018), mainly attributed to the combination of active photochemical production and noncontrollable sources, such as intercontinental pollution transport, lightning, and wildfire events (Fiore et al., 2002; Jaffe et al., 2018). Downward transport of $O_3$ during stratospheric intrusions is also considered to be a contributing factor during summertime (Danielsen, 1980; Lefohn et al., 2011; Lefohn, Wernli, Shadwick, Oltmans, & Shapiro, 2012; Zanis et al., 2014; Akritidis et al., 2016; Yang et al., 2016; Škerlak, Pfahl, Sprenger, & Wernli, 2019). The transport is achieved irreversibly by a tongue-like structure containing high stratospheric $O_3$ extruding downward, folding into the tropospheric air and descending toward the surface (Danielsen, 1968; Johnson & Viezee, 1981). When a stratospheric intrusion contributes high $O_3$ to the surface, in addition to that produced by anthropogenic pollution, it could easily push the surface $O_3$ values beyond the National Ambient Air Quality Standard threshold 70 ppbv (Langford et al., 2017; Škerlak et al., 2019). Observational and modeling studies have shown that surface $O_3$ extremes that are directly associated with downward transport from the stratosphere preferentially occur in the western U.S. (Stohl et al., 2003; Lin et al., 2012, 2015; Škerlak, Sprenger, & Wernli, 2014). Consequently, the joint effects of chemistry and episodic stratospheric transport make the western U.S. a hot spot of $O_3$ pollution in summer.

Due to the large dynamic variability of the tropopause, limited temporal and spatial extent of measurements, and mixing with tropospheric air, the observations of transport due to stratospheric intrusions are challenging (Stohl et al., 2003). In addition, most of the previous studies focused on springtime stratospheric influence because tropopause $O_3$ abundances and downward air mass fluxes maximize during that time (Langford, 1999; Prather, Zhu, Tang, Hsu, & Neu, 2011; Langford et al., 2009, 2012; Lin et al., 2012, 2015; Langford et al., 2017; Albers et al., 2018). The linkage between summertime stratospheric intrusion and high surface $O_3$ events over the western U.S. has received less attention (Lefohn et al., 2011, 2012). By analyzing the output of a state-of-the-art chemistry climate model implemented with an artificial stratospheric ozone tracer ($O_3S$), we aim to 1. estimate the contribution of $O_3$ reaching the surface associated with summertime stratospheric intrusions, 2. understand the space-time behavior of stratospheric intrusion events, and 3. clarify the underlying dynamical mechanism.

## 4.2 Methods

### 4.2.1 CESM2(WACCM6) and $O_3S$ Diagnostic

We analyzed daily surface $O_3$ and stratospheric $O_3$ tracer (denoted by $O_3S$) from 1995 to 2014 summer months (June-August, JJA) using the Whole Atmosphere Community Climate Model version 6 (WACCM6) of the Community Earth System Model version 2 (CESM2). It is the high-top version of the Community Atmosphere Model version 6 (CAM6), integrating the atmospheric physics and chemistry from the surface to nearly 140 km. The WACCM6 uses the same atmospheric physics as CAM6. The chemical mechanism includes comprehensive troposphere, stratosphere, mesosphere and lower thermosphere chemistry, described by Emmons et al. (2020). The standard emissions are based on anthropogenic and biomass burning inventories specified for the Coupled Model Intercomparison Project 6 (CMIP6). WACCM6 is coupled to the interactive Community Land Model version 5 (CLM5), which handles dry deposition. The simulations shown here are fully coupled ocean-atmosphere experiment, and feature $0.95° \times 1.25°$ (latitude$\times$longitude) horizontal resolution and 70 layers, with $\sim 1.2$ km vertical resolution above the boundary layer to the lower stratosphere. We consider WACCM6 is well suited for studying the transport during stratospheric intrusion because that 1. the atmospheric chemistry and deposition scheme for $O_3$ are well represented and tropospheric $O_3$ simulations are improved in comparison to observations (Emmons et al., 2020); 2. WACCM6 is able to effectively reproduce the observed wind and temperature climatologies as well as stratospheric variability (Gettelman et al., 2019); 3. the twenty-year simulation with daily output of $O_3$ and $O_3S$ provides us with large samples to study. Detailed model formulations, descriptions, and evaluations can be found in Gettelman et al. (2019) and Emmons et al. (2020).

To quantify the stratospheric contribution to high surface $O_3$ events, we study an artificial tracer, $O_3S$, for $O_3$ originating in the stratosphere, which is implemented in a manner as described in Tilmes et al. (2016). $O_3S$ experiences the same loss rate as $O_3$ in the troposphere but is not affected by $NO_x$ photolysis as defined by the Chemistry-Climate Model Initiative (CCMI). Earlier studies have shown that the diagnostics of deep stratospheric intrusions are insensitive to the choice of tropopause definition (Yang et al., 2016) or $O_3S$ tagging methods (Lin et al., 2012).

### 4.2.2 Maximum Covariance Analysis

Maximum Covariance Analysis (MCA), known as Singular Value Decomposition (SVD) analysis, is a useful tool for detecting coherent patterns between two different geophysical fields (Bretherton, Smith, & Wallace, 1992; Hurrell, 1995; Dai, 2013). In this study, we isolate pairs of spatial patterns and corresponding time series by performing the eigenanalysis on the temporal covariance matrix between $O_3$ anomalies and $O_3S$ anomalies at the lowest model level (Bretherton, 2015). Daily anomalies of $O_3$ and $O_3S$ at the lowest model level are derived with respect to the twenty-year (1995-2014) mean of that day. The considered domain in this study is 20°-50°N, 70°-140°W.

## 4.3 Results

### 4.3.1 Evaluation of CESM2(WACCM6)

Here we first evaluate the WACCM6 simulations against observations from the Tropospheric Ozone Assessment Report (TOAR, Schultz et al., 2017). Figure 4.1a is the 1995-2014 mean of "*all_mean*" variables from the TOAR 5°×5° (latitude×longitude) monthly median products. High $O_3$ values ($\sim$ 45 nmol/mol) are seen over the western U.S. in TOAR measurements. For WACCM6, we have gridded the simulations onto the horizontal grid of TOAR data and calculated median $O_3$ concentrations using the same metrics to guarantee an apple-to-apple comparison (see Figure 4.1b). Generally a good agreement is found between the model and observations over the Central U.S. and most of the West Region, with percentage differences within 15% (see Figure A.13). However, WACCM6 overestimates the surface median $O_3$ over the southeast U.S. by 55% ($\sim$ 15 nmol/mol), which is consistent with the evaluation in Emmons et al. (2020). The biased $O_3$ over the eastern U.S. is a long existing problem that can have various reasons starting with still insufficient complexity of the chemistry, but also the model resolution, deposition scheme, etc. (Schwantes et al., 2020).

Figure 4.1c, d show the 1995-2014 mean of daily $O_3$ and $O_3S$ simulations in $0.95° \times 1.25°$ (latitude×longitude) resolution at the lowest model level, respectively. Figure 4.1c is similar to Figure 4.1b and shows that high $O_3$ are concentrated over the western U.S. As shown in 4.1d, strong stratospheric impact, ranging from 6-10 nmol/mol, is found over the Canada-U.S. border and the Western States, including southern British Columbia, Washington, Oregon, Idaho, Montana, Wyoming, Cali-

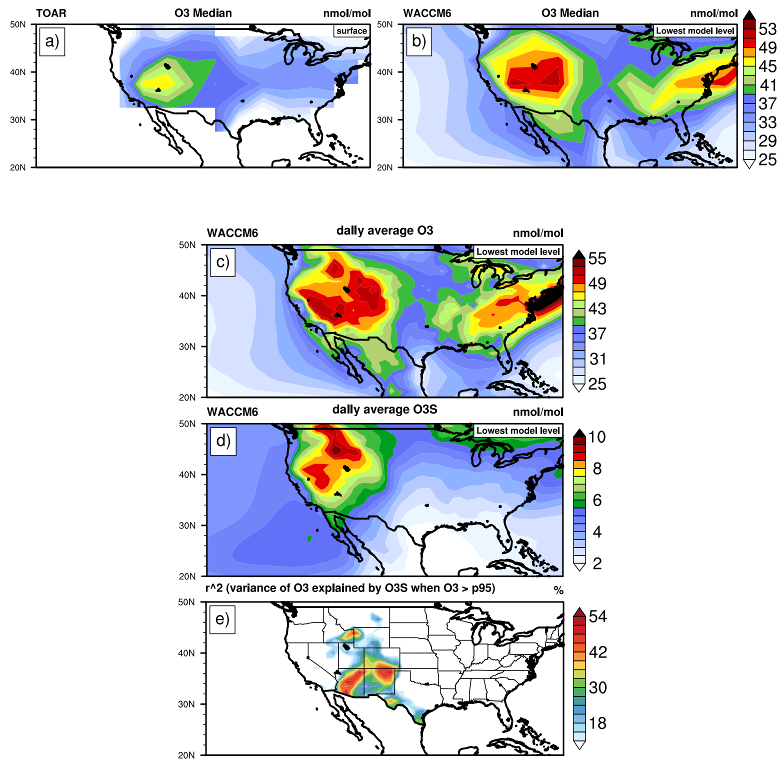


Figure 4.1. Twenty-year (1995-2014) mean of summertime surface $O_3$ median values (a) observed from the TOAR and (b) simulated in WACCM6 at the lowest model level with 5° latitude ×5° longitude resolution. (c) and (d) show the mean of daily average $O_3$ and $O_3S$ simulations at the lowest model level in the same time period, respectively. Note the ranges of color bars are different. (e) $R^2$ in color shows the near-surface $O_3$ variance explained by surface $O_3S$ when surface $O_3 > 95^{th}$ percentile at each grid cell during 1995-2014 summer.

fornia, Nevada, Utah, Arizona, and Colorado. Our model simulation is in agreement with previous observational studies which reported that deep stratospheric intrusions preferentially occur in the West and the Intermountain West (Brioude et al., 2007; Bourqui & Trépanier, 2010; Ambrose, Reidmiller, & Jaffe, 2011; Lefohn et al., 2011, 2012; Lin et al., 2012; Langford et al., 2012, 2015, 2017; Clark & Chiao, 2019). A minimum stratospheric impact occurs in the Southeast, in good agreement with results in Lin et al. (2012). These features are also consistent with simulations by the Geophysical Fluid Dynamics Laboratory global chemistry-climate model (Clifton, Fiore, Correa, Horowitz, & Naik, 2014). Additionally, the simulated stratospheric impact in late spring (Figure A.14) agrees well with that shown in Figure 11c and d from Lin et al. (2012).

We now estimate the importance of $O_3S$ on surface $O_3$. We calculate the percentage of variance ($r^2$) of surface $O_3$ explained by surface $O_3S$ when surface $O_3$ exceeds the $95^{th}$ percentile (p95, hereinafter) value at each grid point during 1995-2014 summer months using daily average $O_3$ and $O_3S$ (see Figure 4.1c,d). The linear trend has been removed before the calculation. As suggested in Figure 4.1e, high peaks are located over Wyoming, southern Texas, and the Four Corners area (Colorado, Utah, Arizona, and New Mexico). We see in Arizona, for example, $O_3S$ can explain as high as 54% of surface $O_3$ variance during days in which surface $O_3$ exceeds p95. We compare our results with those from prior observational studies. Lefohn et al. (2012) studied stratospheric intrusion events associated with daily maximum hourly $O_3$ in exceedance of 50 nmol/mol at both rural and urban monitoring sites of the U.S. Statistically significant relations are found over the southern Texas, Arizona, Colorado, Utah, Nevada, California, and Wyoming in summer months during 2006-2008. Overall, our model simulations support observational findings that stratospheric intrusions coincident with $O_3$ preferentially take place in the West and Intermountain West during summertime. We also quantify the stratospheric impact when surface $O_3$ exceeds p95 at each grid cell and find that in regional average over the western U.S. (30°N-50°N, 100°W-125°W), the stratospheric contribution is 18.4% (not shown).

#### 4.3.2 MCA Results and Interpretation

We employ MCA to investigate how surface $O_3$ is related to $O_3S$ reaching the surface on daily basis. The first two leading modes are summarized in Figure 4.2. Together, these two modes explain 60% of the covariance pattern over the domain of interest. The first mode shows large positive covariances over the eastern Pacific, western and northern tier of the U.S. (Figure 4.2a). The second mode shows dipole structure with $O_3$ and $O_3S$ surplus over the western U.S. and deficit over the east (Figure 4.2b). Surface level $O_3S$ anomalies are found to lag the 200-500 hPa $O_3S$ anomalies by two days (not shown), suggesting the downward influence. No significant lead-lag relationships are found either between the expansion coefficient time series (loadings) of $O_3$ and $O_3S$ at the surface or between the first two SVD modes.

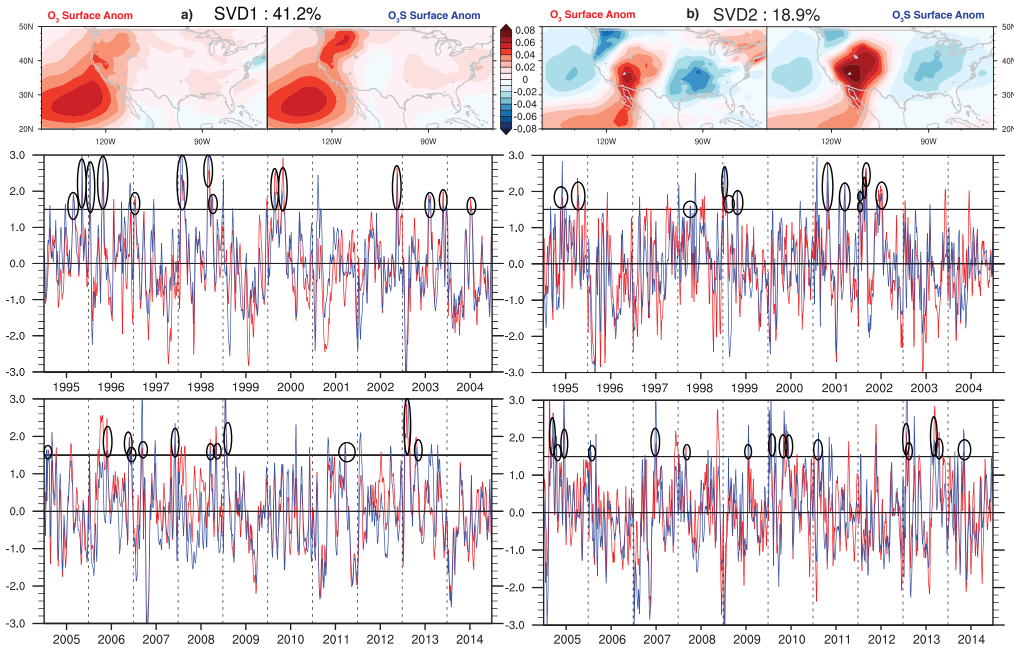


Figure 4.2. Spatial and temporal patterns of the two leading modes from MCA with a) Mode 1 on the left and b) Mode 2 on the right. Upper panels show the covariance patterns between surface $O_3$ anomalies and surface $O_3S$ anomalies on daily bases in JJA over 1995-2014. Red (blue) color shadings represent positive (negative) values. The number shown in the top center is the portion of the covariance explained by each mode. Below are the standardized anomalies of the loadings with red lines representing the principal component coefficients of surface $O_3$ anomalies in summer from 1995 to 2014 and blue for surface $O_3S$ anomalies. Black circles indicate the occurrences of the high surface $O_3$ events as defined in the text.

We identify $\sim$ 20 days per month (1404 days in twenty years for the first two leading modes) when both expansion coefficient time series are greater than 0, indicating that surface $O_3$ concentration increase is coincident with $O_3S$ reaching the surface. Lefohn et al. (2011, 2012) investigated the frequency of surface $O_3$ enhancements that are associated with stratosphere-to-troposphere transport down to the surface across the U.S. and reported that the average number of days per month ranges from 16 days to 23 days at monitoring sites in the West and Intermountain West in summer months. Our results of intrusion frequency are in remarkable agreement with their results.

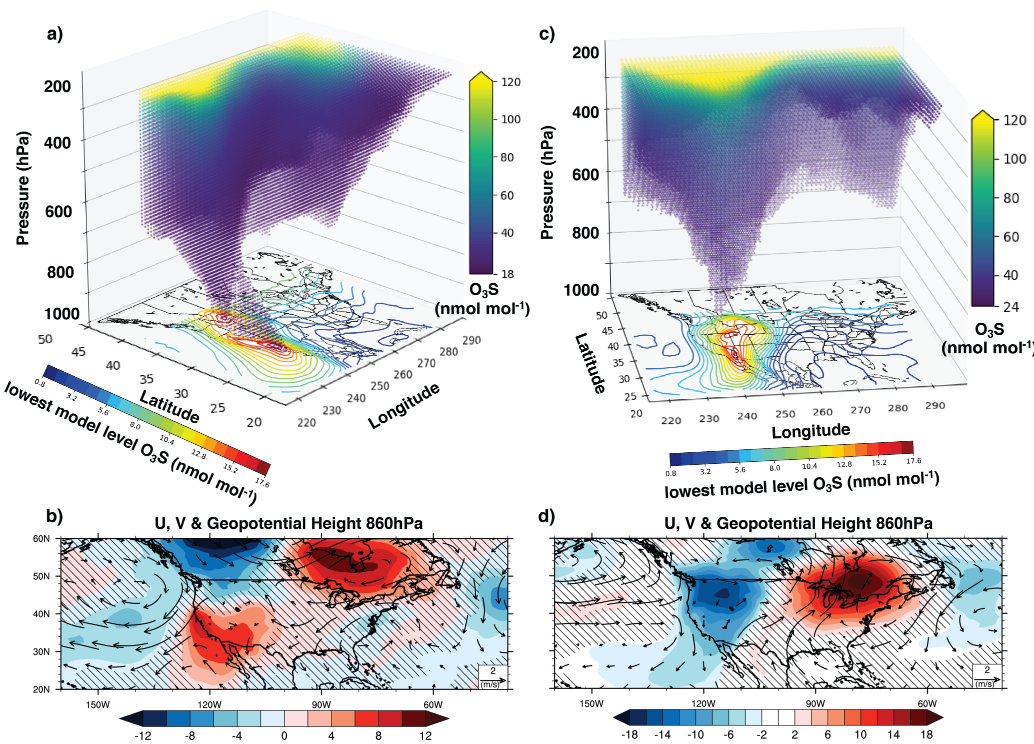


Figure 4.3. (a) Composited $O_3S$ structure of high surface $O_3$ events for Mode 1. For illustrative purpose, scatter plot includes only the grid points with $O_3S > 18$ nmol/mol. (b) A map of 860 hPa geopotential height anomalies (in color, unit is m) and surface wind anomalies (in vectors, m/s) composited to the defined high surface $O_3$ events for Mode 1. The hatching denotes that the geopotential height anomalies are not statistically significant at the 95% confidence level using the Student's $t$ test. (c) (d) are similar to (a) (b) but for Mode 2. For illustrative purpose, scatter plot (c) includes only the grid points with $O_3S > 24$ nmol/mol.

Next, we define high surface $O_3$ events caused by stratospheric intrusions when both loadings exceed 1.5 standard deviations, as marked by black circles in Figure 4.2. Each event lasts for a few days. Based on this definition, composite analyses according to high surface $O_3$ events are carried out using $O_3S$ daily data. The composited patterns are not sensitive to the thresholds we chose for the analyses.

Schematics in Figure 4.3 show the large amplitude composited $O_3S$ structures and near-surface circulations corresponding to both modes. We use neon yellow color to highlight the area with $O_3S$ larger than 120 nmol/mol, which can be treated approximately as the tropopause (Yang et al., 2016). During Mode 1, depressed tropopause height followed by enhanced $O_3S$ can be found around 50°N, 120°W (Figure 4.3a). Since stratospheric air contains higher values of potential vorticity (PV) and $O_3$, the intrusion of the tropopause tends to replace the tropospheric air by ozone-rich stratospheric air with large PV (Danielsen, 1968; Mote, Holton, & Wallace, 1991; Wimmers et al., 2003). Transport of $O_3S$ to low levels is tied to stratospheric intrusions and strong subsidence in the troposphere. Figure 4.4d shows a map of composited means of 500 hPa vertical velocity ($\omega$) anomalies on the day of the events corresponding to Mode 1. The intrusion is associated with intensified subsidence on the U.S.-Canada border. Coherently, enhanced $O_3S$ on the northern tier can be seen throughout the troposphere, while the maximum over the Pacific appears below 700 hPa (Figure 4.3a). We conduct composited analyses on anomalies of 860 hPa geopotential height as well as surface winds according to events of Mode 1. A quadrupole pattern of low-level geopotential height anomalies is seen over the North American continent. In contrast to the positive correlation between the upper-level cyclonic vorticity and $O_3S$ (Figure A.15a), low-level geopotential height and $O_3S$ reaching the surface are strongly anti-correlated (Figure 4.3b). Dry air (Figure A.15b) with high PV value (Figure A.15a) descends on the northern tier of the U.S. as a result of stratosphere-to-troposphere transport by intensified subsidence. Warm and moist tropospheric air is seen (Figure A.15b-c) downstream (east) of the surface low. In addition to the anomalous descent, we also see a strengthening of northeasterly along the west coast near the surface (Figure 4.3b). This intensified easterly associated with stronger anticyclone facilitates the horizontal transport towards the subtropical Pacific in the mid-to-lower troposphere (Figure 4.3a).

During Mode 2 (Figure 4.3c), the intrusion occurs around 40°N, 115°W. Surface $O_3S$ maximum is concentrated over the Intermountain West, such as Colorado, Arizona, Utah, Nevada. Different from Mode 1, a dipole pattern of the low-level geopotential height anomalies is seen over the continental U.S. Large values of negative geopotential height anomalies are observed above the intermountain regions (Figure 4.3d) aligned with cold dry air and positive PV anomalies (Figure A.16a-c) subsiding west of the surface low pressure while rising warm and moist air occur on the east (Figure 4.4h and Figure A.16b-c).

During both modes, the $O_3S$ reaching the surface can be 10-18 nmol/mol (see surface contours of Figure 4.3a and Figure 4.3c, respectively). In regional average over the western U.S. (30°N-50°N, 100°W-125°W, the stratospheric contribution is 11 nmol/mol. The amplitude agrees well with the observational record from the California Baseline Ozone Transport Study (CABOTS), in which they found that stratospheric contribution is 10-20 nmol/mol to the surface over Northern California during an intrusion case in August 2016 (Clark & Chiao, 2019). We also see $\sim$ 10 days per summer season when high surface $O_3$ events associated with the first two SVD modes occur, with variation across years.

### 4.3.3 Dynamical Mechanism

Next we examine the dynamical mechanism underlying the stratospheric intrusion events associated with Mode 1 and Mode 2. Figure 4.4 shows the time evolution of 500 hPa vertical velocity ($\omega$) anomalies and 200 hPa zonal winds for the composites based on high $O_3$ and $O_3S$ events in Mode 1 (Figure 4.4a-d) and Mode 2 (Figure 4.4e-h), respectively. The positions of the upper-level jet axis are marked by dashed lines. The downstream development (Chang, 1993), characterized by eastward propagation of the wave systems, can be seen in both modes.

More specifically, for Mode 1, the large descending anomaly is centered at 50°N, 160°W on day -6 (Figure 4.4a). After two days, it shifts eastward following the continuous jet (Figure 4.4b). On day -2, the descending center manifests near the west coast (Figure 4.4c), consistent with the result that relationship of 500 hPa $O_3S$

with the principal component of Mode 1 is maximized about two days ahead of surface $O_3S$ peaks (not shown). During day -2 to day 0, the subsidence stays close to the U.S.-Canada border, embedded within the jet stream (Figure 4.4d). On day 0, the strong descent on the northern tier of the U.S. continuously facilitates the downward transport of $O_3S$ toward the surface (Figure 4.3a).

Regarding Mode 2, large disturbance center can be seen on day -6 near the eastern Pacific (Figure 4.4e). From day -4 to day -2, the descending center continues to grow near 135°W (Figure 4.4f-g). The downstream side strengthens remarkably near 125°W where the jet breaks. On day -2, strong anomalous subsidence reaches the western U.S. whereas ascending anomalies are triggered on the east. It is the enhanced subsidence that induces the stratospheric intrusion and downward transport of stratospheric $O_3$ (Figure 4.4h and Figure 4.3c).

During boreal summer, the dominant upper-level circulation consists of westerly jet north of 40°N, together with frequent eastward traveling baroclinic waves (White, 1982). The baroclinic waves commonly exhibit life cycles of baroclinic growth and barotropic decay along the storm track regions (Simmons & Hoskins, 1978; Blackmon, Lee, & Wallace, 1984). Observational and modeling studies have revealed that the baroclinic disturbances leave imprint on atmospheric composition. Aircraft experiments provided evidence that high amounts of stratospheric radioactive debris and ozone were drawn into the troposphere by midlatitude storms (Danielsen, 1968). M. R. Schoeberl and Krueger (1983) and Mote et al. (1991) identified the coherent fluctuations in total $O_3$ and medium scale waves along the wintertime oceanic storm track regions using satellite data. Stone, Randel, Stanford, Read, and Waters (1996) found baroclinic wave features using upper tropospheric water vapor measurement. General circulation model was capable of representing stratosphere-troposphere exchange associated with baroclinic waves in midlatitudes (Mote, Holton, & Boville, 1994). In our study, baroclinic wave system and its resulting circulation is also found important for the occurrence of deep stratospheric intrusions over the western U.S. in summertime (Sprenger & Wernli, 2003).

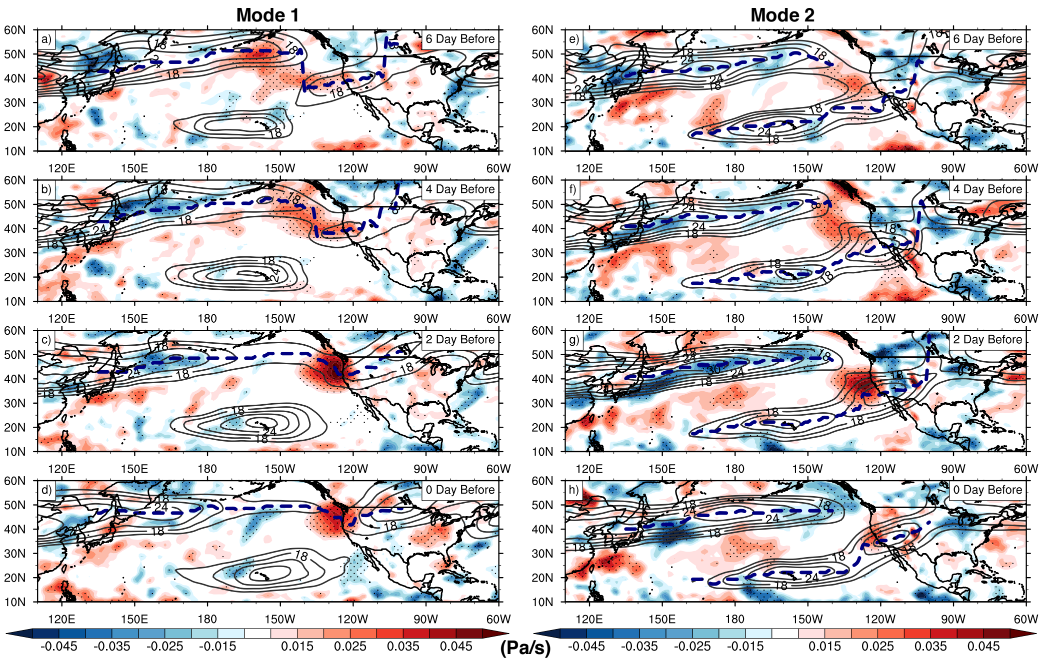


Figure 4.4. Snapshots of composited mean of 500 hPa $\omega$ anomalies (in colors, Pa/s) and 200 hPa zonal winds (in contours, m/s) when large events occur for Mode 1 (left) and for Mode 2 (right) during (a, e) day -6, (b, f) day -4, (c, g) day -2, (d, h) day 0. Red (blue) colors indicate regions with anomalous descent (ascent). Contour interval is 3 m/s. Stippling indicates that the $\omega$ anomalies are statistically significant at the 95% confidence level using the Student's $t$ test. The navy dashed line marks the location of 200 hPa jet axis.

In both modes, we see that the wave trains originate over the baroclinically unstable central Pacific, grow by baroclinic conversion, radiate energy downstream through ageostrophic geopotential fluxes, and dissipate over the jet exit near the western U.S., as discussed in previous studies (Chang & Orlanski, 1993; Chang, 1993). The upper-level jet stream acts as a wave guide, constraining the baroclinic system tightly along its core. From day -2 to day 0 in both modes, the intensified descents at 500 hPa, which corresponded to the downward transport of $O_3S$, are evident near the western U.S. (115°-120°W). These two modes mainly differ by the location of the jet core. For Mode 1, the jet is almost continuous across the North Pacific and the averaged jet axis is located at 46°N. The passage of the wave trains takes about 8 days, starting from central North Pacific (40°N, 170°W, see Figure 4.5a), propagating eastward to the U.S.-Canada border (45°N, 120°W). For Mode 2, the polar jet and the subtropical jet are well separated. The successive baroclinic waves develop rapidly, beginning with a large descending anomaly at the jet exit (40°N, 140°E) from day -6, ending with a trough on the west-and-a-ridge on the east over the continental U.S. (Figure 4.3d).

Finally, Hovmöller diagrams are constructed to summarize the eastward propagating baroclinic systems that occur prior to high surface $O_3$ and $O_3S$ events. The longitude-time plots of 500 hPa $\omega$ anomalies along the latitudinal band of the jet axis are depicted for both modes (Figure 4.5). More specifically, Figure 4.5a is the $\omega$ anomalies along the jet axis as marked in Figure 4.4a-d while Figure 4.5b is plotted along 38°N for simplicity. We can see a sequence of downstream developing wave train originating from the North Pacific and propagating along the upper-level jet. Eastward propagation of Mode 2 is less clear than that of Mode 1. The descending anomalies begin to amplify near the jet exit two days before the deep intrusions over the western U.S. Similar conclusions are also found using upper-level meridional velocity (not shown). The results are consistent with evolving of baroclinic waves, and are in good agreement with the wave train signature diagnosed in Lim and Wallace (1991) and Chang (1993), in terms of their structure, magnitude, and traveling speed.

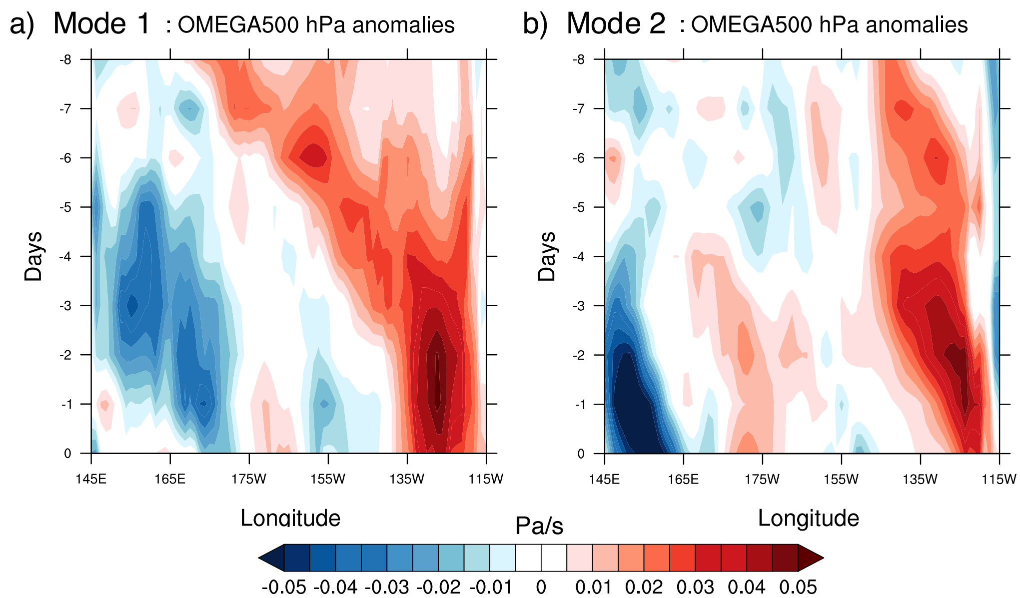


Figure 4.5. Days versus longitude diagrams of $\omega$ anomalies (Pa/s) at 500 hPa (a) along the band of 200 hPa jet axis for Mode 1 and (b) along 38°N for Mode 2, respectively.

To sum up, the large $O_3$ events caused by deep intrusions are associated with eastward propagating baroclinic systems tied closely to the North Pacific storm tracks, with enhanced wave amplitudes and descents over the jet exit region near the western U.S.

## 4.4 Conclusions and Discussions

Our study has examined high surface $O_3$ events associated with downward transport from the stratosphere over the U.S. during summertime, when high temperature could further increase the impact of $O_3$ pollution on mortality. By analyzing a twenty-year (1995-2014) simulation by CESM2(WACCM6), we have found that the stratospheric $O_3$ can explain as high as 54% of surface $O_3$ variability when surface $O_3$ exceeds $95^{th}$ percentile, and the regional averaged stratospheric contribution is $\sim$ 18% over the western U.S. We have further analyzed the circumstances when stratospheric intrusions of ozone covary with surface $O_3$ anomalies over the region of 20°-50°N and 70°-140°W on daily basis using MCA. The first two leading modes explain 60% of the total covariance pattern. In Mode 1, deep stratospheric intrusions occur preferentially over the northwestern U.S. The associated intensified northeasterly wind anomalies over the west coast further brings continental $O_3S$ towards the Pacific Ocean. In Mode 2, deep stratospheric intrusions occur over the Intermountain West. The composited $O_3S$ values reaching the surface associated with these two SVD modes range from 10-18 nmol/mol. In regional average over the western U.S., the stratospheric contribution is 11 nmol/mol. Both modes are results of eastward propagating wave trains, originating from the central North Pacific and amplifying near the jet exit, with enhanced subsidence over the western U.S.

We have also repeated our MCA analysis to demonstrate the robustness of the dynamical mechanism across seasons. The first leading mode and corresponding anomalous $\omega$ evolution prior to instrusion events for winter, spring, and fall seasons are summarized in Figure A.17-A.19. The first leading modes during each of the seasons explain $\sim 40\%$ of covariance between $O_3$ and $O_3S$. Similarly, we find that the strongest disturbance extends from the central North Pacific to the west coast of the U.S. during day -6 to day -4. During day -2 to day 0, the descents strengthen remarkably over the west coast while new ascending centers develop on the downstream side. The downward $O_3$ transport is typically regulated by upper-level jet streams across seasons, consistent with previous studies (Langford, 1999; Lin et al., 2015; Albers et al., 2018).

Overall, our study has demonstrated that summertime stratospheric intrusions, though infrequent, can contribute crucially to surface $O_3$ extremes over the Western U.S. These stratospheric intrusion events are caused by strong subsidence in the region, which is a result of eastward propagating baroclinic waves originating from the central North Pacific Ocean. However, a few caveats have to be noted. WACCM6 overestimates tropospheric $O_3$ and thus the exact contribution of stratospheric intrusion to surface should be treated with caution. Additionally, our diagnostic is based on one single climate model because of the use of daily $O_3S$ output. It's worth performing similar analyses in other chemistry climate models to assess the robustness of the conclusions. Future work will also be devoted to 1. studying simulations with high spatiotemporal resolution at certain hot spot areas so that our results can directly benefit air pollution management, and 2. understanding the origination of upstream baroclinic disturbance so that we can improve the predictability of such $O_3$ extremes associated with summertime stratospheric intrusions.

# 5. CONCLUSIONS AND FUTURE DIRECTIONS

## 5.1 Conclusions

As introduced in Chapter 1, the UTLS is dynamically active and its chemical composition plays a crucial in the climate system. The focus of this thesis has been on understanding the bidirectional transport processes in the UTLS associated with monsoonal circulations.

In Chapter 2, we examined the representation of SWV associated with the Asian summer monsoon in different configurations of WACCM models. We found that the majority of the WACCM produced the SWV maximum over the central Pacific Ocean, instead of over the Asian continent as observed. The high vertical resolution version of WACCM with refined GWD parameterization, though displaying a dry bias on the poleward side, corrects the deficiency with SWV confined within the AMA and maximized over the continent. Our results indicated that the temperature over the central Pacific Ocean is a significant factor in the representation of the Asian monsoon characters in the UTLS. We found that the WACCM with increased vertical resolution and refined GWD is capable of alleviating the cold bias above and the warm bias below 100 hPa over the central Pacific Ocean, and therefore simulates a steepened PV gradient over the central Pacific Ocean that better closes the upper-level anticyclone and confines the SWV within the enhanced transport barrier.

In Chapter 3, we investigated efficient pathways connecting surface air to the North American UTLS. Our pulse tracer diagnostic showed that the fast transport into the NA UTLS region can occur in a small fraction of cases with modal age less than 20 days. For these fast cases, the origin is enhanced deep convection over the eastern Pacific and the Gulf of Mexico, rather than locally over the contiguous United States. Deep convection controls transport from the boundary layer to 200 hPa, and then enhanced large-scale circulation, as a balanced response to the enhanced convection, dominates transport upwards into the UTLS region and anticyclonically towards southern United States.

Finally, in Chapter 4, we examined the downward transport of stratospheric $O_3$ induced by stratospheric intrusions in summer months by analyzing a twenty-year simulation by CESM2(WACCM6). We found that the stratospheric contribution is $\sim 18\%$ during days in which surface $O_3$ exceeds $95^{th}$ percentile over the western U.S. We further analyzed the circumstances when stratospheric intrusions of ozone covary with surface $O_3$ anomalies on daily basis using maximum covariance analysis. The first two leading modes explain 60% of the total covariance pattern. In Mode 1, deep stratospheric intrusions occur preferentially over the northwestern U.S. The associated intensified northeasterly wind anomalies over the west coast further brings continental $O_3S$ towards the Pacific Ocean. The composited $O_3S$ reaching the surface associated ranges from 10-18 nmol/mol. In Mode 2, deep stratospheric intrusions occur over the Intermountain West. The composited stratospheric contribution is $\sim 11\%$ nmol/mol. Both modes are results of eastward propagating wave trains, originating from the central North Pacific and amplifying near the jet exit, with enhanced subsidence over the western U.S.

## 5.2 Future Directions

There are still large knowledge gaps regarding the dynamical and chemical couplings between the UTLS and the summer monsoons:

1. Apart from the persistent anticyclone associated with chemical maxima on climatological scale, the Asian monsoon anticyclone exhibits west-east oscillation associated with eddy shedding on synoptic scale. Coherently, the tropospheric pollutants within the upper-level anticyclone are shed out during the west-east migrations. The shedding is primarily responsible for trace gas distribution and variability in the UTLS. Previous studies classify the zonal variation of anticyclone center into Tibetan Mode and Iranian Mode (Q. Zhang, Wu, & Qian,

2002), which are related to the strength and location of monsoon convection (Garny & Randel, 2013; Nützel, Dameris, & Garny, 2016). Recently, Honomichl and Pan (2019) have revealed the third preferred anticyclonic center over the western Pacific near 135°E near both 150 hPa and 100 hPa. Examining the western Pacific UTLS outflow is an important objective proposed in the Asian Summer Monsoon Chemical and Climate Impact Project (ACCLIP) campaign that will take place in summer 2021. However, the dynamical drivers of the AMA movement, especially eastward shedding over the western Pacific, remain unclear. Understanding the mechanisms will enable us to improve model representation of eddy shedding events in order to advance the day-to-day chemical forecast of the UTLS composition and facilitate field campaign planning.

2. While water vapor maxima are observed above both Asia and NA during summer, distinct HDO/$H_2O$ ratio (i.e., $\delta D$) patterns in the UTLS are found over the two regions in the Atmospheric Chemistry Experiment Fourier transform spectrometer (ACE-FTS, Randel et al., 2012). The water isotopes are regulated by phase changes. Heavier isotopologue HDO tends to be removed from vapor phase. Therefore, different isotopic compositions are possibly due to differing background thermodynamic structure. Studies on isotopic effects of monsoon systems in the UTLS are limited by the difficulty in estimating the effect of physical processes and also by model biases in temperature and precipitation (Lee, Fung, DePaolo, & Henning, 2007; Lee, Pierrehumbert, Swann, & Lintner, 2009; Galewsky et al., 2016). Incorporating the cycling of water isotopes into the GCMs is important in interpreting convective influence on water vapor isotope.

3. Monsoon circulations are expected to change in an evolving climate. The troposphere-to-stratosphere transport associated with the Asian and the NA monsoons is also likely to change as greenhouse gases increase. Analyzing the changes in transport pathways and involved dynamics under a warming climate

has great implications for predicting the chemical composition and climate in the stratosphere. However, only a few works have studied future transport changes in the UTLS (Abalos et al., 2017, and references therein). Additionally, discrepancies exist among the results, which are challenging to interpret since different chemical constituents and models are analyzed.

REFERENCES

# REFERENCES


Abalos, M., Randel, W., Kinnison, D., & Serrano, E. (2013). Quantifying tracer transport in the tropical lower stratosphere using WACCM. *Atmos. Chem. Phys*, *13*(10), 591–10.

Abalos, M., Randel, W. J., Kinnison, D. E., & Garcia, R. R. (2017). Using the artificial tracer e90 to examine present and future UTLS tracer transport in WACCM. *Journal of the Atmospheric Sciences*, *74*(10), 3383–3403.

Ackerman, T. P., Liou, K.-N., Valero, F. P., & Pfister, L. (1988). Heating rates in tropical anvils. *Journal of the atmospheric sciences*, *45*(10), 1606–1623.

Adams, D. K., & Comrie, A. C. (1997). The north American monsoon. *Bulletin of the American Meteorological Society*, *78*(10), 2197–2214.

Akritidis, D., Pozzer, A., Zanis, P., Tyrlis, E., Skerlak, B., Sprenger, M., & Lelieveld, J. (2016). On the role of tropopause folds in summertime tropospheric ozone over the eastern Mediterranean and the Middle East. *Atmospheric Chemistry and Physics*, *16*(21), 14025.

Albers, J. R., Perlwitz, J., Butler, A. H., Birner, T., Kiladis, G. N., Lawrence, Z. D., … Dias, J. (2018). Mechanisms Governing Interannual Variability of Stratosphere-to-Troposphere Ozone Transport. *Journal of Geophysical Research: Atmospheres*, *123*(1), 234–260.

Ambrose, J., Reidmiller, D., & Jaffe, D. (2011). Causes of high $O_3$ in the lower free troposphere over the Pacific Northwest as observed at the Mt. Bachelor Observatory. *Atmospheric Environment*, *45*(30), 5302–5315.

Anderson, J. G., Weisenstein, D. K., Bowman, K. P., Homeyer, C. R., Smith, J. B., Wilmouth, D. M., … others (2017). Stratospheric ozone over the United States in summer linked to observations of convection and temperature via chlorine and bromine catalysis. *Proceedings of the National Academy of Sciences*, *114*(25), E4905–E4913.

Anderson, J. G., Wilmouth, D. M., Smith, J. B., & Sayres, D. S. (2012). UV dosage levels in summer: Increased risk of ozone loss from convectively injected water vapor. *Science*, *337*(6096), 835–839.

Andrews, D. G., Holton, J. R., & Leovy, C. B. (1987). *Middle atmosphere dynamics* (No. 40). Academic press.

Arnone, E., Smith, A., Enell, C.-F., Kero, A., & Dinelli, B. (2014). WACCM climate chemistry sensitivity to sprite perturbations. *Journal of Geophysical Research: Atmospheres*, *119*(11), 6958–6970.

Bannister, R., O'neill, A., Gregory, A., & Nissen, K. (2004). The role of the south-east Asian monsoon and other seasonal features in creating the 'tape-recorder'signal in the Unified Model. *Quarterly Journal of the Royal Meteorological Society*, *130*(599), 1531–1554.

Bergman, J. W., Fierli, F., Jensen, E. J., Honomichl, S., & Pan, L. L. (2013). Boundary layer sources for the Asian anticyclone: Regional contributions to a vertical conduit. *Journal of Geophysical Research: Atmospheres*, *118*(6), 2560–2575.

Blackmon, M. L., Lee, Y., & Wallace, J. M. (1984). Horizontal structure of 500 mb height fluctuations with long, intermediate and short time scales. *Journal of the Atmospheric Sciences*, *41*(6), 961–980.

Boehm, M. T., & Lee, S. (2003). The implications of tropical Rossby waves for tropical tropopause cirrus formation and for the equatorial upwelling of the Brewer–Dobson circulation. *Journal of the atmospheric sciences*, *60*(2), 247–261.

Bosilovich, M. G., Akella, S., Coy, L., Cullather, R., Draper, C., Gelaro, R., ... others (2015). MERRA-2: Initial evaluation of the climate. *NASA Tech. Rep. Series on Global Modelling and Data Assimilation NASA/TM–2015-104606, Vol. 43, 145 pp.*.

Bourqui, M., & Trépanier, P.-Y. (2010). Descent of deep stratospheric intrusions during the IONS August 2006 campaign. *Journal of Geophysical Research: Atmospheres*, *115*(D18).

Bretherton, C. S. (2015). Maximum covariance analysis, ATM 522 notes. Retrieved from https://atmos.washington.edu/ breth/classes/AS552/lect/lect22.pdf.

Bretherton, C. S., Smith, C., & Wallace, J. M. (1992). An intercomparison of methods for finding coupled patterns in climate data. *Journal of climate*, *5*(6), 541–560.

Brewer, A. (1949). Evidence for a world circulation provided by the measurements of helium and water vapour distribution in the stratosphere. *Quarterly Journal of the Royal Meteorological Society*, *75*(326), 351–363.

Brioude, J., Cooper, O., Trainer, M., Ryerson, T., Holloway, J., Baynard, T., ... others (2007). Mixing between a stratospheric intrusion and a biomass burning plume. *Atmospheric Chemistry and Physics*, *7*(16), 4229–4235. Retrieved from `https://acp.copernicus.org/articles/7/4229/2007/` doi: 10.5194/acp-7-4229-2007

Butchart, N., Anstey, J. A., Hamilton, K., Osprey, S., McLandress, C., Bushell, A. C., ... others (2018). Overview of experiment design and comparison of models participating in phase 1 of the SPARC Quasi-Biennial Oscillation initiative (QBOi). *Geoscientific Model Development*, *11*(3), 1009–1032.

Calvo, N., Garcia, R., Randel, W., & Marsh, D. (2010). Dynamical mechanism for the increase in tropical upwelling in the lowermost tropical stratosphere during warm ENSO events. *Journal of the Atmospheric Sciences*, *67*(7), 2331–2340.

Chang, E. K. (1993). Downstream development of baroclinic waves as inferred from regression analysis. *Journal of the atmospheric sciences*, *50*(13), 2038–2053.

Chang, E. K., & Orlanski, I. (1993). On the dynamics of a storm track. *Journal of the atmospheric sciences*, *50*(7), 999–1015.

Charlton-Perez, A. J., Baldwin, M. P., Birner, T., Black, R. X., Butler, A. H., Calvo, N., ... others (2013). On the lack of stratospheric dynamical variability in low-top versions of the CMIP5 models. *Journal of Geophysical Research: Atmospheres*, *118*(6), 2494–2505.

Chen, B., Tung, W.-w., & Yanai, M. (2016). Multiscale Temporal Mean Features of Perturbation Kinetic Energy and Its Budget in the Tropics: Review and Computation. *Meteorological Monographs*, *56*, 8–1.

Chen, B., Xu, X., Yang, S., & Zhao, T. (2012). Climatological perspectives of air transport from atmospheric boundary layer to tropopause layer over Asian monsoon regions during boreal summer inferred from Lagrangian approach. *Atmospheric Chemistry & Physics Discussions*, *12*(2).

Chen, G., & Sun, L. (2011). Mechanisms of the tropical upwelling branch of the Brewer–Dobson circulation: The role of extratropical waves. *Journal of the Atmospheric Sciences*, *68*(12), 2878–2892.

Clapp, C., & Anderson, J. (2019). Modeling the effect of potential nitric acid removal during convective injection of water vapor over the Central United States on the chemical composition of the lower stratosphere. *Journal of Geophysical Research: Atmospheres*, *124*(16), 9743–9770.

Clark, J., & Chiao, S. (2019). A Case Study of Stratospheric Ozone Transport to the Northern San Francisco Bay Area and Sacramento Valley during CABOTS 2016. *Journal of Applied Meteorology and Climatology*, *58*(12), 2675–2697.

Clifton, O. E., Fiore, A. M., Correa, G., Horowitz, L. W., & Naik, V. (2014). Twenty-first century reversal of the surface ozone seasonal cycle over the northeastern United States. *Geophysical Research Letters*, *41*(20), 7343–7350.

Collins, W., Derwent, R., Garnier, B., Johnson, C., Sanderson, M., & Stevenson, D. (2003). Effect of stratosphere-troposphere exchange on the future tropospheric ozone trend. *Journal of Geophysical Research: Atmospheres*, *108*(D12).

Cooney, J. W., Bowman, K. P., Homeyer, C. R., & Fenske, T. M. (2018). Ten year analysis of tropopause-overshooting convection using GridRad data. *Journal of Geophysical Research: Atmospheres*, *123*(1), 329–343.

Dai, A. (2013). Increasing drought under global warming in observations and models. *Nature Climate Change*, *3*(1), 52.

Danielsen, E. F. (1968). Stratospheric-tropospheric exchange based on radioactivity, ozone and potential vorticity. *Journal of the Atmospheric Sciences*, *25*(3), 502–518.

Danielsen, E. F. (1980). Stratospheric source for unexpectedly large values of ozone measured over the Pacific Ocean during Gametag, August 1977. *Journal of Geophysical Research: Oceans*, *85*(C1), 401–412.

Dee, D. P., Uppala, S., Simmons, A., Berrisford, P., Poli, P., Kobayashi, S., ... others (2011). The ERA-Interim reanalysis: Configuration and performance of the data assimilation system. *Quarterly Journal of the royal meteorological society*, *137*(656), 553–597.

de F. Forster, P. M., & Shine, K. P. (1999a). Stratospheric water vapour changes as a possible contributor to observed stratospheric cooling. *Geophysical research letters*, *26*(21), 3309–3312.

de F. Forster, P. M., & Shine, K. P. (1999b). Stratospheric water vapour changes as a possible contributor to observed stratospheric cooling. *Geophysical Research Letters*, *26*(21), 3309–3312. Retrieved from `http://dx.doi.org/10.1029/1999GL010487` doi: 10.1029/1999GL010487

Dessler, A., Schoeberl, M., Wang, T., Davis, S., & Rosenlof, K. (2013). Stratospheric water vapor feedback. *Proceedings of the National Academy of Sciences*, *110*(45), 18087–18091.

Dessler, A., & Sherwood, S. (2004). Effect of convection on the summertime extratropical lower stratosphere. *Journal of Geophysical Research: Atmospheres*, *109*(D23).

Dethof, A., O'Neill, A., Slingo, J., & Smit, H. (1999). A mechanism for moistening the lower stratosphere involving the Asian summer monsoon. *Quarterly Journal of the Royal Meteorological Society*, *125*(556), 1079–1106.

Dobson, G. M. B. (1956). Origin and distribution of the polyatomic molecules in the atmosphere. *Proceedings of the Royal Society of London. Series A. Mathematical and Physical Sciences*, *236*(1205), 187–193.

Dunkerton, T. J. (1995). Evidence of meridional motion in the summer lower stratosphere adjacent to monsoon regions. *Journal of Geophysical Research: Atmospheres*, *100*(D8), 16675–16688.

Dütsch, H. (1978). Vertical ozone distribution on a global scale. *pure and applied geophysics*, *116*(2-3), 511–529.

Dvortsov, V. L., & Solomon, S. (2001). Response of the stratospheric temperatures and ozone to past and future increases in stratospheric humidity. *Journal of Geophysical Research: Atmospheres*, *106*(D7), 7505–7514.

Emmons, L. K., Schwantes, R. H., Orlando, J. J., Tyndall, G., Kinnison, D., Lamarque, J.-F., ... others (2020). The Chemistry Mechanism in the Community Earth System Model version 2 (CESM2). *Journal of Advances in Modeling Earth Systems*.

Eyring, V., Lamarque, J.-F., Hess, P., Arfeuille, F., Bowman, K., Chipperfiel, M. P., ... others (2013). Overview of IGAC/SPARC Chemistry-Climate Model Initiative (CCMI) community simulations in support of upcoming ozone and climate assessments. *SPARC newsletter*, *40*(Januar), 48–66.

Fiore, A. M., Jacob, D. J., Bey, I., Yantosca, R. M., Field, B. D., Fusco, A. C., & Wilkinson, J. G. (2002). Background ozone over the United States in summer: Origin, trend, and contribution to pollution episodes. *Journal of Geophysical Research: Atmospheres*, *107*(D15), ACH–11.

Folkins, I., Oltmans, S. J., & Thompson, A. M. (2000). Tropical convective outflow and near surface equivalent potential temperatures. *Geophysical Research Letters*, *27*(16), 2549–2552.

Froyd, K. D., Murphy, D. M., Sanford, T. J., Thomson, D. S., Wilson, J. C., Pfister, L., & Lait, L. (2009). Aerosol composition of the tropical upper troposphere. *Atmospheric Chemistry and Physics*, *9*(13), 4363–4385. Retrieved from `https://acp.copernicus.org/articles/9/4363/2009/` doi: 10.5194/acp-9-4363-2009

Fu, R., Hu, Y., Wright, J. S., Jiang, J. H., Dickinson, R. E., Chen, M., ... Wu, D. L. (2006). Short circuit of water vapor and polluted air to the global stratosphere by convective transport over the Tibetan Plateau. *Proceedings of the National Academy of Sciences*, *103*(15), 5664–5669.

Fueglistaler, S., Dessler, A., Dunkerton, T., Folkins, I., Fu, Q., & Mote, P. W. (2009). Tropical tropopause layer. *Reviews of Geophysics*, *47*(1).

Fueglistaler, S., Liu, Y., Flannaghan, T., Haynes, P., Dee, D., Read, W., ... others (2013). The relation between atmospheric humidity and temperature trends for stratospheric water. *Journal of Geophysical Research: Atmospheres*, *118*(2), 1052–1074.

Fueglistaler, S., Wernli, H., & Peter, T. (2004). Tropical troposphere-to-stratosphere transport inferred from trajectory calculations. *Journal of Geophysical Research: Atmospheres*, *109*(D3).

Gage, K., McAfee, J., Carter, D., Ecklund, W., Riddle, A., Balsley, B., & REID, G. (1991). Long-term mean vertical motion over the tropical Pacific- Wind-profiling Doppler radar measurements. *Science*, *254*(5039), 1771–1773.

Galewsky, J., Steen-Larsen, H. C., Field, R. D., Worden, J., Risi, C., & Schneider, M. (2016). Stable isotopes in atmospheric water vapor and applications to the hydrologic cycle. *Reviews of Geophysics*, *54*(4), 809–865.

Garcia, R. R., & Randel, W. J. (2008). Acceleration of the Brewer–Dobson circulation due to increases in greenhouse gases. *Journal of the Atmospheric Sciences*, *65*(8), 2731–2739.

Garcia, R. R., & Richter, J. H. (2019). On the momentum budget of the quasi-biennial oscillation in the whole atmosphere community climate model. *Journal of the Atmospheric Sciences*, *76*(1), 69–87.

Garcia, R. R., Smith, A. K., Kinnison, D. E., Cámara, Á. d. l., & Murphy, D. J. (2017). Modification of the gravity wave parameterization in the Whole Atmosphere Community Climate Model: Motivation and results. *Journal of the Atmospheric Sciences*, *74*(1), 275–291.

Garny, H., Dameris, M., Randel, W., Bodeker, G. E., & Deckert, R. (2011). Dynamically forced increase of tropical upwelling in the lower stratosphere. *Journal of the Atmospheric Sciences*, *68*(6), 1214–1233.

Garny, H., & Randel, W. (2013). Dynamic variability of the Asian monsoon anticyclone observed in potential vorticity and correlations with tracer distributions. *Journal of Geophysical Research: Atmospheres*, *118*(24), 13–421.

Garny, H., & Randel, W. J. (2016). Transport pathways from the Asian monsoon anticyclone to the stratosphere. *Atmospheric Chemistry and Physics*, *16*(4), 2703–2718.

Gaudel, A., Cooper, R., Ancellet, G., Barret, B., Boynard, A., Burrows, J., ... others (2018). Tropospheric Ozone Assessment Report: Present-day distribution and trends of tropospheric ozone relevant to climate and global atmospheric chemistry model evaluation. *Elementa: Science of the Anthropocene*, *6*(1), art–39.

Gettelman, A., Hegglin, M. I., Son, S.-W., Kim, J., Fujiwara, M., Birner, T., ... others (2010). Multimodel assessment of the upper troposphere and lower stratosphere: Tropics and global trends. *Journal of Geophysical Research: Atmospheres*, *115*(D3).

Gettelman, A., Kinnison, D. E., Dunkerton, T. J., & Brasseur, G. P. (2004). Impact of monsoon circulations on the upper troposphere and lower stratosphere. *Journal of Geophysical Research: Atmospheres*, *109*(D22).

Gettelman, A., Mills, M., Kinnison, D., Garcia, R., Smith, A., Marsh, D., ... others (2019). The Whole Atmosphere Community Climate Model Version 6 (WACCM6). *Journal of Geophysical Research: Atmospheres*, *124*(23), 12380–12403.

Gettelman, A., et al. (2002). A climatology of the tropical tropopause layer. *Journal of the Meteorological Society of Japan. Ser. II*, *80*(4B), 911–924.

Gill, A. E. (1980). Some simple solutions for heat-induced tropical circulation. *Quarterly Journal of the Royal Meteorological Society*, *106*(449), 447–462.

Hardiman, S. C., Boutle, I. A., Bushell, A. C., Butchart, N., Cullen, M. J., Field, P. R., ... others (2015). Processes controlling tropical tropopause temperature and stratospheric water vapor in climate models. *Journal of Climate*, *28*(16), 6516–6535.

Haynes, P., McIntyre, M., Shepherd, T., Marks, C., & Shine, K. P. (1991). On the "downward control" of extratropical diabatic circulations by eddy-induced mean zonal forces. *Journal of the Atmospheric Sciences*, *48*(4), 651–678.

Hegglin, M. I., & Shepherd, T. G. (2009). Large climate-induced changes in ultraviolet index and stratosphere-to-troposphere ozone flux. *Nature Geoscience*, *2*(10), 687–691.

Higgins, R., Yao, Y., & Wang, X. (1997). Influence of the North American monsoon system on the US summer precipitation regime. *Journal of Climate*, *10*(10), 2600–2622.

Highwood, E., & Hoskins, B. (1998). The tropical tropopause. *Quarterly Journal of the Royal Meteorological Society*, *124*(549), 1579–1604.

Holton, J. R., Haynes, P. H., McIntyre, M. E., Douglass, A. R., Rood, R. B., & Pfister, L. (1995). Stratosphere-troposphere exchange. *Reviews of geophysics*, *33*(4), 403–439.

Honomichl, S. B., & Pan, L. L. (2019). Transport from the Asian Summer Monsoon Anticyclone over the Western Pacific. *Journal of Geophysical Research: Atmospheres*, e2019JD032094.

Hoskins, B. J., & Rodwell, M. J. (1995). A model of the Asian summer monsoon. Part I: The global scale. *Journal of the Atmospheric Sciences*, *52*(9), 1329–1340.

Hossaini, R., Chipperfield, M., Montzka, S., Rap, A., Dhomse, S., & Feng, W. (2015). Efficiency of short-lived halogens at influencing climate through depletion of stratospheric ozone. *Nature Geoscience*, *8*(3), 186–190.

Hsu, C. J., & Plumb, R. A. (2000). Nonaxisymmetric thermally driven circulations and upper-tropospheric monsoon dynamics. *Journal of the atmospheric sciences*, *57*(9), 1255–1276.

Hurrell, J. W. (1995). Decadal trends in the North Atlantic Oscillation: regional temperatures and precipitation. *Science*, *269*(5224), 676–679.

Hurrell, J. W., Holland, M. M., Gent, P. R., Ghan, S., Kay, J. E., Kushner, P. J., ... others (2013). The community earth system model: a framework for collaborative research. *Bulletin of the American Meteorological Society*, *94*(9), 1339–1360.

Inness, P. M., Slingo, J. M., Woolnough, S. J., Neale, R. B., & Pope, V. (2001). Organization of tropical convection in a GCM with varying vertical resolution; implications for the simulation of the Madden-Julian Oscillation. *Climate Dynamics*, *17*(10), 777–793.

Jackson, D., Driscoll, S., Highwood, E., Harries, J., & Russell, J. (1998). Troposphere to stratosphere transport at low latitudes as studies using HALOE observations of water vapour 1992–1997. *Quarterly Journal of the Royal Meteorological Society*, *124*(545), 169–192.

Jaeglé, L., Wood, R., & Wargan, K. (2017). Multiyear Composite View of Ozone Enhancements and Stratosphere-to-Troposphere Transport in Dry Intrusions of Northern Hemisphere Extratropical Cyclones. *Journal of Geophysical Research: Atmospheres*, *122*(24), 13–436.

Jaffe, D. A., Cooper, O. R., Fiore, A. M., Henderson, B. H., Tonnesen, G. S., Russell, A. G., ... Moore, T. (2018). Scientific assessment of background ozone over the US: Implications for air quality management. *Elementa (Washington, DC)*, *6*(1), 56.

Jiang, J. H., Su, H., Zhai, C., Perun, V. S., Del Genio, A., Nazarenko, L. S., ... others (2012). Evaluation of cloud and water vapor simulations in CMIP5 climate models using NASA "A-Train" satellite observations. *Journal of Geophysical Research: Atmospheres*, *117*(D14).

Jiang, J. H., Su, H., Zhai, C., Wu, L., Minschwaner, K., Molod, A. M., & Tompkins, A. M. (2015). An assessment of upper troposphere and lower stratosphere water vapor in MERRA, MERRA2, and ECMWF reanalyses using Aura MLS observations. *Journal of Geophysical Research: Atmospheres*, *120*(22).

Jin, F., & Hoskins, B. J. (1995). The direct response to tropical heating in a baroclinic atmosphere. *Journal of the atmospheric sciences*, *52*(3), 307–319.

Johnson, W. B., & Viezee, W. (1981). Stratospheric ozone in the lower troposphere—I. Presentation and interpretation of aircraft measurements. *Atmospheric Environment (1967)*, *15*(7), 1309–1323.

Kim, J., Grise, K. M., & Son, S.-W. (2013). Thermal characteristics of the cold-point tropopause region in CMIP5 models. *Journal of Geophysical Research: Atmospheres*, *118*(16), 8827–8841.

Kim, J., Randel, W. J., & Birner, T. (2018). Convectively driven tropopause-level cooling and its influences on stratospheric moisture. *Journal of Geophysical Research: Atmospheres*, *123*(1), 590–606.

Koby, T. R. (2016). *Development of a trajectory model for the analysis of stratospheric water vapor* (Unpublished doctoral dissertation). Harvard University.

Kuang, Z., & Bretherton, C. S. (2004). Convective influence on the heat balance of the tropical tropopause layer: A cloud-resolving model study. *Journal of the atmospheric sciences*, *61*(23), 2919–2927.

Kunz, A., Pan, L., Konopka, P., Kinnison, D., & Tilmes, S. (2011). Chemical and dynamical discontinuity at the extratropical tropopause based on START08 and WACCM analyses. *Journal of Geophysical Research: Atmospheres*, *116*(D24).

Lamarque, J.-F., Emmons, L., Hess, P., Kinnison, D. E., Tilmes, S., Vitt, F., ... others (2012). CAM-chem: Description and evaluation of interactive atmospheric chemistry in the Community Earth System Model. *Geoscientific Model Development*, *5*(2), 369.

Langford, A. (1999). Stratosphere-troposphere exchange at the subtropical jet: Contribution to the tropospheric ozone budget at midlatitudes. *Geophysical research letters*, *26*(16), 2449–2452.

Langford, A., Aikin, K., Eubank, C., & Williams, E. (2009). Stratospheric contribution to high surface ozone in Colorado during springtime. *Geophysical Research Letters*, *36*(12).

Langford, A., Alvarez, R., Brioude, J., Fine, R., Gustin, M., Lin, M., ... others (2017). Entrainment of stratospheric air and Asian pollution by the convective boundary layer in the southwestern US. *Journal of Geophysical Research: Atmospheres*, *122*(2), 1312–1337.

Langford, A., Brioude, J., Cooper, O., Senff, C., Alvarez, R., Hardesty, R., ... Oltmans, S. (2012). Stratospheric influence on surface ozone in the Los Angeles area during late spring and early summer of 2010. *Journal of Geophysical Research: Atmospheres*, *117*(D21).

Langford, A., Senff, C., Alvarez Ii, R., Brioude, J., Cooper, O., Holloway, J., ... others (2015). An overview of the 2013 Las Vegas Ozone Study (LVOS): Impact of stratospheric intrusions and long-range transport on surface air quality. *Atmospheric environment*, *109*, 305–322.

Lau, W. K., Yuan, C., & Li, Z. (2018). Origin, maintenance and variability of the Asian Tropopause Aerosol Layer (ATAL): the roles of monsoon dynamics. *Scientific reports*, *8*(1), 1–14.

Lee, J.-E., Fung, I., DePaolo, D. J., & Henning, C. C. (2007). Analysis of the global distribution of water isotopes using the NCAR atmospheric general circulation model. *Journal of Geophysical Research: Atmospheres*, *112*(D16).

Lee, J.-E., Pierrehumbert, R., Swann, A., & Lintner, B. R. (2009). Sensitivity of stable water isotopic values to convective parameterization schemes. *Geophysical Research Letters*, *36*(23).

Lefohn, A. S., Wernli, H., Shadwick, D., Limbach, S., Oltmans, S. J., & Shapiro, M. (2011). The importance of stratospheric–tropospheric transport in affecting surface ozone concentrations in the western and northern tier of the United States. *Atmospheric environment*, *45*(28), 4845–4857.

Lefohn, A. S., Wernli, H., Shadwick, D., Oltmans, S. J., & Shapiro, M. (2012). Quantifying the importance of stratospheric-tropospheric transport on surface ozone concentrations at high-and low-elevation monitoring sites in the United States. *Atmospheric environment*, *62*, 646–656.

Levine, J., Braesicke, P., Harris, N., Savage, N., & Pyle, J. (2007). Pathways and timescales for troposphere-to-stratosphere transport via the tropical tropopause layer and their relevance for very short lived substances. *Journal of Geophysical Research: Atmospheres*, *112*(D4).

Levy, B. S., & Patz, J. A. (2015). Climate change, human rights, and social justice. *Annals of global health*, *81*(3), 310–322.

Li, D., Vogel, B., Bian, J., Müller, R., Pan, L. L., Günther, G., … others (2017). Impact of typhoons on the composition of the upper troposphere within the Asian summer monsoon anticyclone: the SWOP campaign in Lhasa 2013. *Atmospheric chemistry and physics*, *17*(7), 4657.

Li, Q., Jacob, D. J., Park, R., Wang, Y., Heald, C. L., Hudman, R., … Evans, M. (2005). North American pollution outflow and the trapping of convectively lifted pollution by upper-level anticyclone. *Journal of Geophysical Research: Atmospheres*, *110*(D10).

Li, Q., Jiang, J. H., Wu, D. L., Read, W. G., Livesey, N. J., Waters, J. W., … others (2005). Convective outflow of South Asian pollution: A global CTM simulation compared with EOS MLS observations. *Geophysical Research Letters*, *32*(14).

Li, X., Ting, M., Li, C., & Henderson, N. (2015). Mechanisms of Asian summer monsoon changes in response to anthropogenic forcing in CMIP5 models. *Journal of Climate*, *28*(10), 4107–4125.

Lim, G. H., & Wallace, J. M. (1991). Structure and evolution of baroclinic waves as inferred from regression analysis. *Journal of the atmospheric sciences*, *48*(15), 1718–1732.

Lin, M., Fiore, A. M., Cooper, O. R., Horowitz, L. W., Langford, A. O., Levy, H., … Senff, C. J. (2012). Springtime high surface ozone events over the western United States: Quantifying the role of stratospheric intrusions. *Journal of Geophysical Research: Atmospheres*, *117*(D21).

Lin, M., Fiore, A. M., Horowitz, L. W., Langford, A. O., Oltmans, S. J., Tarasick, D., & Rieder, H. E. (2015). Climate variability modulates western US ozone air quality in spring via deep stratospheric intrusions. *Nature Communications*, *6*, 7105.

Lindzen, R. S., & Fox-Rabinovitz, M. (1989). Consistent vertical and horizontal resolution. *Monthly Weather Review*, *117*(11), 2575–2583.

Livesey, N. J., Read, W. G., Wagner, P. A., Froidevaux, L., Lambert, A., Manney, G. L., ... others (2015). Earth Observing System (EOS) Aura Microwave Limb Sounder (MLS) version 4.2 x level 2 data quality and description document, JPL D-33509 rev. A. *Jet Propulsion Laboratory, available at: http://mls. jpl. nasa. gov/data/v4-2_data_ quality_document. pdf (last access: 18 August 2016).*

Marsh, D. R., Mills, M. J., Kinnison, D. E., Lamarque, J.-F., Calvo, N., & Polvani, L. M. (2013). Climate change from 1850 to 2005 simulated in CESM1 (WACCM). *Journal of Climate*, *26*(19), 7372–7391.

Maycock, A. C., Joshi, M. M., Shine, K. P., & Scaife, A. A. (2013). The circulation response to idealized changes in stratospheric water vapor. *Journal of Climate*, *26*(2), 545–561.

Mills, M. J., Richter, J. H., Tilmes, S., Kravitz, B., MacMartin, D. G., Glanville, A. A., ... others (2017). Radiative and chemical response to interactive stratospheric sulfate aerosols in fully coupled CESM1 (WACCM). *Journal of Geophysical Research: Atmospheres*, *122*(23), 13–061.

Mills, M. J., Schmidt, A., Easter, R., Solomon, S., Kinnison, D. E., Ghan, S. J., ... others (2016). Global volcanic aerosol properties derived from emissions, 1990–2014, using CESM1 (WACCM). *Journal of Geophysical Research: Atmospheres*, *121*(5), 2332–2348.

Milz, M., Von Clarmann, T., Fischer, H., Glatthor, N., Grabowski, U., Höpfner, M., ... others (2005). Water vapor distributions measured with the Michelson Interferometer for Passive Atmospheric Sounding on board Envisat (MIPAS/Envisat). *Journal of Geophysical Research: Atmospheres*, *110*(D24).

Mohanakumar, K. (2008). *Stratosphere troposphere interactions: an introduction.* Springer Science & Business Media.

Morgenstern, O., Hegglin, M. I., Rozanov, E., O'Connor, F. M., Abraham, N. L., Akiyoshi, H., ... others (2017). Review of the global models used within phase 1 of the Chemistry-Climate Model Initiative (CCMI). *Geoscientific Model Development*.

Mote, P. W., Holton, J. R., & Boville, B. A. (1994). Characteristics of stratosphere-troposphere exchange in a general circulation model. *Journal of Geophysical Research: Atmospheres*, *99*(D8), 16815–16829.

Mote, P. W., Holton, J. R., & Wallace, J. M. (1991). Variability in total ozone associated with baroclinic waves. *Journal of the atmospheric sciences*, *48*(16), 1900–1903.

Neale, R. B., Chen, C.-C., Gettelman, A., Lauritzen, P. H., Park, S., Williamson, D. L., ... others (2010). Description of the NCAR community atmosphere model (CAM 5.0). *NCAR Tech. Note NCAR/TN-486+ STR.*

Norton, W. (2001). Longwave heating of the tropical lower stratosphere. *Geophysical research letters*, *28*(19), 3653–3656.

Norton, W. (2006). Tropical wave driving of the annual cycle in tropical tropopause temperatures. Part II: Model results. *Journal of the atmospheric sciences*, *63*(5), 1420–1431.

Nützel, M., Dameris, M., & Garny, H. (2016). Movement, drivers and bimodality of the South Asian High. *Atmospheric Chemistry and Physics*(16), 14755–14774.

Oleson, K., Lawrence, D., Bonan, G., Drewniak, B., Huang, M., Koven, C., ... others (2013). Technical description of version 4.5 of the Community Land Model (CLM), NCAR Technical Note: NCAR/TN-503+ STR. *National Center for Atmospheric Research (NCAR), Boulder, CO, USA, https://doi.org/10.5065/D6RR1W7M*.

Orbe, C., Holzer, M., & Polvani, L. M. (2012). Flux distributions as robust diagnostics of stratosphere-troposphere exchange. *Journal of Geophysical Research: Atmospheres*, *117*(D1).

Orbe, C., Holzer, M., Polvani, L. M., & Waugh, D. (2013). Air-mass origin as a diagnostic of tropospheric transport. *Journal of Geophysical Research: Atmospheres*, *118*(3), 1459–1470.

Orbe, C., Waugh, D. W., & Newman, P. A. (2015). Air-mass origin in the tropical lower stratosphere: The influence of Asian boundary layer air. *Geophysical Research Letters*, *42*(10), 4240–4248.

Orbe, C., Waugh, D. W., Newman, P. A., & Steenrod, S. (2016). The transit-time distribution from the Northern Hemisphere midlatitude surface. *Journal of the Atmospheric Sciences*, *73*(10), 3785–3802.

Pan, L. L., Honomichl, S. B., Kinnison, D. E., Abalos, M., Randel, W. J., Bergman, J. W., & Bian, J. (2016). Transport of chemical tracers from the boundary layer to stratosphere associated with the dynamics of the Asian summer monsoon. *Journal of Geophysical Research: Atmospheres*, *121*(23).

Park, M., Randel, W. J., Emmons, L. K., Bernath, P. F., Walker, K. A., & Boone, C. D. (2008). Chemical isolation in the Asian monsoon anticyclone observed in Atmospheric Chemistry Experiment (ACE-FTS) data. *Atmospheric Chemistry and Physics*, *8*(3), 757–764.

Park, M., Randel, W. J., Emmons, L. K., & Livesey, N. J. (2009). Transport pathways of carbon monoxide in the Asian summer monsoon diagnosed from Model of Ozone and Related Tracers (MOZART). *Journal of Geophysical Research: Atmospheres*, *114*(D8).

Park, M., Randel, W. J., Gettelman, A., Massie, S. T., & Jiang, J. H. (2007). Transport above the Asian summer monsoon anticyclone inferred from Aura Microwave Limb Sounder tracers. *Journal of Geophysical Research: Atmospheres*, *112*(D16).

Park, M., Randel, W. J., Kinnison, D. E., Garcia, R. R., & Choi, W. (2004). Seasonal variation of methane, water vapor, and nitrogen oxides near the tropopause: Satellite observations and model simulations. *Journal of Geophysical Research: Atmospheres*, *109*(D3).

Park, S., & Bretherton, C. S. (2009). The University of Washington shallow convection and moist turbulence schemes and their impact on climate simulations with the Community Atmosphere Model. *Journal of Climate*, *22*(12), 3449–3469.

Ploeger, F., Gottschling, C., Griessbach, S., Grooß, J.-U., Guenther, G., Konopka, P., . . . others (2015). A potential vorticity-based determination of the transport barrier in the Asian summer monsoon anticyclone. *Atmospheric chemistry and physics*, *15*(22), 13145–13159.

Ploeger, F., Günther, G., Konopka, P., Fueglistaler, S., Müller, R., Hoppe, C., . . . Riese, M. (2013). Horizontal water vapor transport in the lower stratosphere from subtropics to high latitudes during boreal summer. *Journal of Geophysical Research: Atmospheres*, *118*(14), 8111–8127.

Ploeger, F., Konopka, P., Walker, K., & Riese, M. (2017). Quantifying pollution transport from the Asian monsoon anticyclone into the lower stratosphere. *Atmospheric Chemistry and Physics*, *17*(11), 7055.

Plumb, R. A. (1996). A "tropical pipe" model of stratospheric transport. *Journal of Geophysical Research: Atmospheres*, *101*(D2), 3957–3972.

Plumb, R. A., & Eluszkiewicz, J. (1999). The Brewer–Dobson circulation: Dynamics of the tropical upwelling. *Journal of the atmospheric sciences*, *56*(6), 868–890.

Pope, V., Pamment, J., Jackson, D., & Slingo, A. (2001). The representation of water vapor and its dependence on vertical resolution in the Hadley Centre Climate Model. *Journal of climate*, *14*(14), 3065–3085.

Popovic, J. M., & Plumb, R. A. (2001). Eddy shedding from the upper-tropospheric Asian monsoon anticyclone. *Journal of the atmospheric sciences*, *58*(1), 93–104.

Prather, M. J., Zhu, X., Tang, Q., Hsu, J., & Neu, J. L. (2011). An atmospheric chemist in search of the tropopause. *Journal of Geophysical Research: Atmospheres*, *116*(D4).

Qu, X., & Huang, G. (2015). The decadal variability of the tropical Indian Ocean SST–the South Asian High relation: CMIP5 model study. *Climate Dynamics*, *45*(1-2), 273–289.

Randel, W. J., & Jensen, E. J. (2013). Physical processes in the tropical tropopause layer and their roles in a changing climate. *Nature Geoscience*, *6*(3), 169–176.

Randel, W. J., Moyer, E., Park, M., Jensen, E., Bernath, P., Walker, K., & Boone, C. (2012). Global variations of HDO and HDO/H2O ratios in the upper troposphere and lower stratosphere derived from ACE-FTS satellite measurements. *Journal of Geophysical Research: Atmospheres*, *117*(D6).

Randel, W. J., & Park, M. (2006). Deep convective influence on the Asian summer monsoon anticyclone and associated tracer variability observed with Atmospheric Infrared Sounder (AIRS). *Journal of Geophysical Research: Atmospheres*, *111*(D12).

Randel, W. J., Park, M., Emmons, L., Kinnison, D., Bernath, P., Walker, K. A., . . . Pumphrey, H. (2010). Asian monsoon transport of pollution to the stratosphere. *Science*, *328*(5978), 611–613.

Randel, W. J., & Wu, F. (2005). Kelvin wave variability near the equatorial tropopause observed in GPS radio occultation measurements. *Journal of Geophysical Research: Atmospheres*, *110*(D3).

Randel, W. J., Wu, F., Gettelman, A., Russell, J., Zawodny, J. M., & Oltmans, S. J. (2001). Seasonal variation of water vapor in the lower stratosphere observed in Halogen Occultation Experiment data. *Journal of Geophysical Research: Atmospheres*, *106*(D13), 14313–14325.

Randel, W. J., Wu, F., Voemel, H., Nedoluha, G. E., & Forster, P. (2006). Decreases in stratospheric water vapor after 2001: Links to changes in the tropical tropopause and the brewer-dobson circulation. *Journal of Geophysical Research: Atmospheres*, *111*(D12).

Randel, W. J., Zhang, K., & Fu, R. (2015). What controls stratospheric water vapor in the NH summer monsoon regions? *Journal of Geophysical Research: Atmospheres*, *120*(15), 7988–8001.

Reid, G., & Gage, K. (1996). The tropical tropopause over the western Pacific: Wave driving, convection, and the annual cycle. *Journal of Geophysical Research: Atmospheres*, *101*(D16), 21233–21241.

Richter, J. H., & Rasch, P. J. (2008). Effects of convective momentum transport on the atmospheric circulation in the Community Atmosphere Model, version 3. *Journal of Climate*, *21*(7), 1487–1499.

Richter, J. H., Sassi, F., & Garcia, R. R. (2010). Toward a physically based gravity wave source parameterization in a general circulation model. *Journal of the Atmospheric Sciences*, *67*(1), 136–156.

Richter, J. H., Solomon, A., & Bacmeister, J. T. (2014). Effects of vertical resolution and nonorographic gravity wave drag on the simulated climate in the Community Atmosphere Model, version 5. *Journal of Advances in Modeling Earth Systems*, *6*(2), 357–383.

Rienecker, M. M., Suarez, M. J., Gelaro, R., Todling, R., Bacmeister, J., Liu, E., … others (2011). MERRA: NASA's modern-era retrospective analysis for research and applications. *Journal of climate*, *24*(14), 3624–3648.

Rodwell, M. J., & Hoskins, B. J. (1996). Monsoons and the dynamics of deserts. *Quarterly Journal of the Royal Meteorological Society*, *122*(534), 1385–1404.

Roeckner, E., Brokopf, R., Esch, M., Giorgetta, M., Hagemann, S., Kornblueh, L., … Schulzweida, U. (2006). Sensitivity of simulated climate to horizontal and vertical resolution in the ECHAM5 atmosphere model. *Journal of Climate*, *19*(16), 3771–3791.

Rosenlof, K. H., Tuck, A. F., Kelly, K. K., Russell, J. M., & McCormick, M. P. (1997). Hemispheric asymmetries in water vapor and inferences about transport in the lower stratosphere. *Journal of Geophysical Research: Atmospheres*, *102*(D11), 13213–13234.

Ryu, J.-H., & Lee, S. (2010). Effect of tropical waves on the tropical tropopause transition layer upwelling. *Journal of the Atmospheric Sciences*, *67*(10), 3130–3148.

Santee, M., Manney, G., Livesey, N., Schwartz, M., Neu, J., & Read, W. (2017). A comprehensive overview of the climatological composition of the Asian summer monsoon anticyclone based on 10 years of Aura Microwave Limb Sounder measurements. *Journal of Geophysical Research: Atmospheres*, *122*(10), 5491–5514.

Schoeberl, M., & Dessler, A. (2011). Dehydration of the stratosphere. *Atmospheric Chemistry and Physics*, *11*(16), 8433–8446.

Schoeberl, M. R., & Krueger, A. J. (1983). Medium scale disturbances in total ozone during southern hemisphere summer. *Bulletin of the American Meteorological Society*, *64*(12), 1358–1365.

Schultz, M. G., Schröder, S., Lyapina, O., Cooper, O. R., Galbally, I., Petropavlovskikh, I., ... others (2017). Tropospheric Ozone Assessment Report: Database and metrics data of global surface ozone observations. *Elementa: Science of the Anthropocene*, *5*.

Schwantes, R. H., Emmons, L. K., Orlando, J. J., Barth, M. C., Tyndall, G. S., Hall, S. R., ... others (2020). Comprehensive isoprene and terpene gas-phase chemistry improves simulated surface ozone in the southeastern US. *Atmospheric Chemistry & Physics*, *20*(6).

Schwartz, M. J., Read, W. G., Santee, M. L., Livesey, N. J., Froidevaux, L., Lambert, A., & Manney, G. L. (2013). Convectively injected water vapor in the North American summer lowermost stratosphere. *Geophysical Research Letters*, *40*(10), 2316–2321.

Shapiro, M. (1980). Turbulent mixing within tropopause folds as a mechanism for the exchange of chemical constituents between the stratosphere and troposphere. *Journal of the Atmospheric Sciences*, *37*(5), 994–1004.

Sherwood, S. C., Horinouchi, T., & Zeleznik, H. A. (2003). Convective impact on temperatures observed near the tropical tropopause. *Journal of the atmospheric sciences*, *60*(15), 1847–1856.

Simmons, A. J., & Hoskins, B. J. (1978). The life cycles of some nonlinear baroclinic waves. *Journal of the Atmospheric Sciences*, *35*(3), 414–432.

Siu, L. W., & Bowman, K. P. (2019). Forcing of the Upper-Tropospheric Monsoon Anticyclones. *Journal of the Atmospheric Sciences*, *76*(7), 1937–1954.

Škerlak, B. (2014). *Climatology and process studies of tropopause folds, cross-tropopause exchange, and transport into the boundary layer* (Unpublished doctoral dissertation). ETH Zurich.

Škerlak, B., Pfahl, S., Sprenger, M., & Wernli, H. (2019). A numerical process study on the rapid transport of stratospheric air down to the surface over western North America and the Tibetan Plateau. *Atmospheric Chemistry and Physics*, *19*(9), 6535–6549.

Škerlak, B., Sprenger, M., & Wernli, H. (2014). A global climatology of stratosphere-troposphere exchange using the ERA-Interim data set from 1979 to 2011. *Atmospheric Chemistry & Physics*, *14*(2).

Smith, J. B., Wilmouth, D. M., Bedka, K. M., Bowman, K. P., Homeyer, C. R., Dykema, J. A., ... others (2017). A case study of convectively sourced water vapor observed in the overworld stratosphere over the United States. *Journal of Geophysical Research: Atmospheres*, *122*(17), 9529–9554.

Smith, K. L., Neely, R., Marsh, D., & Polvani, L. M. (2014). The Specified Chemistry Whole Atmosphere Community Climate Model (SC-WACCM). *Journal of Advances in Modeling Earth Systems*, *6*(3), 883–901.

Solomon, D. L., Bowman, K. P., & Homeyer, C. R. (2016). Tropopause-penetrating convection from three-dimensional gridded NEXRAD data. *Journal of Applied Meteorology and Climatology*, *55*(2), 465–478.

Solomon, S., Daniel, J. S., Neely, R. R., Vernier, J.-P., Dutton, E. G., & Thomason, L. W. (2011). The persistently variable "background" stratospheric aerosol layer and global climate change. *Science*, *333*(6044), 866–870.

Solomon, S., Kinnison, D., Garcia, R. R., Bandoro, J., Mills, M., Wilka, C., ... others (2016). Monsoon circulations and tropical heterogeneous chlorine chemistry in the stratosphere. *Geophysical Research Letters*, *43*(24), 12–624.

Solomon, S., Rosenlof, K. H., Portmann, R. W., Daniel, J. S., Davis, S. M., Sanford, T. J., & Plattner, G.-K. (2010). Contributions of stratospheric water vapor to decadal changes in the rate of global warming. *Science*, *327*(5970), 1219–1223.

Sprenger, M., & Wernli, H. (2003). A northern hemispheric climatology of cross-tropopause exchange for the ERA15 time period (1979–1993). *Journal of Geophysical Research: Atmospheres*, *108*(D12).

Sprenger, M., Wernli, H., & Bourqui, M. (2007). Stratosphere–troposphere exchange and its relation to potential vorticity streamers and cutoffs near the extratropical tropopause. *Journal of the atmospheric sciences*, *64*(5), 1587–1602.

Stohl, A., Bonasoni, P., Cristofanelli, P., Collins, W., Feichter, J., Frank, A., ... others (2003). Stratosphere-troposphere exchange: A review, and what we have learned from STACCATO. *Journal of Geophysical Research: Atmospheres*, *108*(D12).

Stone, E. M., Randel, W. J., Stanford, J. L., Read, W. G., & Waters, J. W. (1996). Baroclinic wave variations observed in MLS upper tropospheric water vapor. *Geophysical research letters*, *23*(21), 2967–2970.

Sun, Y., & Huang, Y. (2015). An examination of convective moistening of the lower stratosphere using satellite data. *Earth and Space Science*, *2*(7), 320–330.

Taguchi, M. (2009). Wave driving in the tropical lower stratosphere as simulated by WACCM. Part I: Annual cycle. *Journal of the Atmospheric Sciences*, *66*(7), 2029–2043.

Takahashi, H., Su, H., & Jiang, J. H. (2016). Error analysis of upper tropospheric water vapor in CMIP5 models using "A-Train" satellite observations and reanalysis data. *Climate dynamics*, *46*(9-10), 2787–2803.

Tang, Q., Prather, M., & Hsu, J. (2011). Stratosphere-troposphere exchange ozone flux related to deep convection. *Geophysical research letters*, *38*(3).

Taylor, K. E., Stouffer, R. J., & Meehl, G. A. (2012). An overview of CMIP5 and the experiment design. *Bulletin of the American Meteorological Society*, *93*(4), 485–498.

Thomason, L., & Vernier, J.-P. (2013). Improved SAGE II cloud/aerosol categorization and observations of the Asian tropopause aerosol layer: 1989-2005. *Atmospheric Chemistry and Physics*, *13*(9), 4605.

Tian, B., Fetzer, E. J., Kahn, B. H., Teixeira, J., Manning, E., & Hearty, T. (2013). Evaluating CMIP5 models using AIRS tropospheric air temperature and specific humidity climatology. *Journal of Geophysical Research: Atmospheres*, *118*(1), 114–134.

Tilmes, S., Lamarque, J.-F., Emmons, L. K., Kinnison, D. E., Marsh, D., Garcia, R. R., ... others (2016). Representation of the Community Earth System Model (CESM1) CAM4-chem within the Chemistry-Climate Model Initiative (CCMI). *Geoscientific Model Development Discussions*.

Tissier, A.-S., & Legras, B. (2016). Convective sources of trajectories traversing the tropical tropopause layer. *Atmospheric Chemistry and Physics*, *16*(5), 3383–3398.

Tsuda, T., Murayama, Y., Wiryosumarto, H., Harijono, S. W. B., & Kato, S. (1994). Radiosonde observations of equatorial atmosphere dynamics over Indonesia: 1. Equatorial waves and diurnal tides. *Journal of Geophysical Research: Atmospheres*, *99*(D5), 10491–10505.

Uma, K., Das, S. K., & Das, S. S. (2014). A climatological perspective of water vapor at the UTLS region over different global monsoon regions: observations inferred from the Aura-MLS and reanalysis data. *Climate dynamics*, *43*(1-2), 407–420.

Vaughan, G., & Timmis, C. (1998). Transport of near-tropopause air into the lower midlatitude stratosphere. *Quarterly Journal of the Royal Meteorological Society*, *124*(549), 1559–1578.

Vernier, J.-P., Fairlie, T., Natarajan, M., Wienhold, F., Bian, J., Martinsson, B., ... Bedka, K. (2015). Increase in upper tropospheric and lower stratospheric aerosol levels and its potential connection with asian pollution. *Journal of Geophysical Research: Atmospheres*, *120*(4), 1608–1619.

Vernier, J.-P., Thomason, L., & Kar, J. (2011). CALIPSO detection of an Asian tropopause aerosol layer. *Geophysical Research Letters*, *38*(7).

Vogel, B., Günther, G., Müller, R., Grooß, J., Hoor, P., Krämer, M., ... Riese, M. (2014). Fast transport from Southeast Asia boundary layer sources to northern Europe: rapid uplift in typhoons and eastward eddy shedding of the Asian monsoon anticyclone. *Atmos. Chem. Phys*, *14*(23), 12–745.

Vogel, B., Müller, R., Günther, G., Spang, R., Hanumanthu, S., Li, D., ... Stiller, G. P. (2019). Lagrangian simulations of the transport of young air masses to the top of the Asian monsoon anticyclone and into the tropical pipe. *Atmospheric Chemistry and Physics*, *19*(9), 6007–6034.

Wang, B., Yim, S.-Y., Lee, J.-Y., Liu, J., & Ha, K.-J. (2014). Future change of asian-australian monsoon under rcp 4.5 anthropogenic warming scenario. *Climate dynamics*, *42*(1-2), 83–100.

Wang, W., Matthes, K., Schmidt, T., & Neef, L. (2013). Recent variability of the tropical tropopause inversion layer. *Geophysical Research Letters*, *40*(23), 6308–6313.

Wang, X., Wu, Y., Randel, W., & Tilmes, S. (2020). Stratospheric contribution to the summertime high surface ozone events over the western United States. *Environmental Research Letters*. doi: 10.1088/1748-9326/abba53

Wang, X., Wu, Y., Tung, W.-w., Richter, J. H., Glanville, A. A., Tilmes, S., ... Kinnison, D. E. (2018). The Simulation of Stratospheric Water Vapor Over the Asian Summer Monsoon in CESM1 (WACCM) Models. *Journal of Geophysical Research: Atmospheres*, *123*(20), 11–377.

Weinstock, E., Pittman, J., Sayres, D., Smith, J., Anderson, J., Wofsy, S., ... others (2007). Quantifying the impact of the North American monsoon and deep midlatitude convection on the subtropical lowermost stratosphere using in situ measurements. *Journal of Geophysical Research: Atmospheres*, *112*(D18).

White, G. H. (1982). An observational study of the Northern Hemisphere extratropical summertime general circulation. *Journal of the Atmospheric Sciences*, *39*(1), 24–40.

Wimmers, A. J., Moody, J. L., Browell, E. V., Hair, J. W., Grant, W. B., Butler, C. F., ... Ridley, B. A. (2003). Signatures of tropopause folding in satellite imagery. *Journal of Geophysical Research: Atmospheres*, *108*(D4).

WMO. (1986). Atmospheric ozone 1985. *Global Ozone Research and Monitoring Project, Report No. 16*.

Wright, J., Fu, R., Fueglistaler, S., Liu, Y., & Zhang, Y. (2011). The influence of summertime convection over Southeast Asia on water vapor in the tropical stratosphere. *Journal of Geophysical Research: Atmospheres*, *116*(D12).

Wu, Y., Chen, G., Taylor, L., & Zhang, P. (2018). On the linkage between the Asian summer monsoon and tropopause folds. *Journal of Geophysical Research: Atmospheres*, *123*(4), 2037–2049.

Wu, Y., Orbe, C., Tilmes, S., Abalos, M., & Wang, X. (2020). Fast Transport Pathways Into the Northern Hemisphere Upper Troposphere and Lower Stratosphere During Northern Summer. *Journal of Geophysical Research: Atmospheres*, *125*(3), e2019JD031552.

Wu, Y., & Shaw, T. A. (2016). The impact of the Asian summer monsoon circulation on the tropopause. *Journal of Climate*, *29*(24), 8689–8701.

Yanai, M., Esbensen, S., & Chu, J.-H. (1973). Determination of bulk properties of tropical cloud clusters from large-scale heat and moisture budgets. *Journal of the Atmospheric Sciences*, *30*(4), 611–627.

Yanai, M., & Johnson, R. H. (1993). Impacts of cumulus convection on thermodynamic fields. In *The representation of cumulus convection in numerical models* (pp. 39–62). Springer.

Yang, H., Chen, G., Tang, Q., & Hess, P. (2016). Quantifying isentropic stratosphere-troposphere exchange of ozone. *Journal of Geophysical Research: Atmospheres*, *121*(7), 3372–3387.

Yates, E., Iraci, L., Roby, M., Pierce, R., Johnson, M., Reddy, P., ... Gore, W. (2013). Airborne observations and modeling of springtime stratosphere-to-troposphere transport over california. *Atmospheric Chemistry and Physics*, *13*(24), 12481.

Yu, P., Toon, O. B., Neely, R. R., Martinsson, B. G., & Brenninkmeijer, C. A. (2015). Composition and physical properties of the Asian tropopause aerosol layer and the North American tropospheric aerosol layer. *Geophysical research letters*, *42*(7), 2540–2546.

Zanis, P., Hadjinicolaou, P., Pozzer, A., Tyrlis, E., Dafka, S., Mihalopoulos, N., & Lelieveld, J. (2014). Summertime free-tropospheric ozone pool over the eastern Mediterranean/Middle East. *Atmospheric Chemistry and Physics*, *14*(1), 115–132.

Zhang, G. J., & McFarlane, N. A. (1995). Sensitivity of climate simulations to the parameterization of cumulus convection in the Canadian Climate Centre general circulation model. *Atmosphere-ocean*, *33*(3), 407–446.

Zhang, K., Fu, R., Wang, T., & Liu, Y. (2016). Impact of geographic variations of the convective and dehydration center on stratospheric water vapor over the Asian monsoon region. *Atmospheric Chemistry and Physics*, *16*(12), 7825–7835.

Zhang, Q., Wu, G., & Qian, Y. (2002). The bimodality of the 100 hPa South Asia High and its relationship to the climate anomaly over East Asia in summer. *Journal of the Meteorological Society of Japan. Ser. II*, *80*(4), 733–744.

Zhou, X., & Holton, J. R. (2002). Intraseasonal variations of tropical cold-point tropopause temperatures. *Journal of climate*, *15*(12), 1460–1473.

# APPENDICES

# A. SUPPLEMENTARY ILLUSTRATIVE MATERIAL

First seven figures are for the second chapter. The following five figures are for the third chapter. The last seven figures are for the fourth chapter.

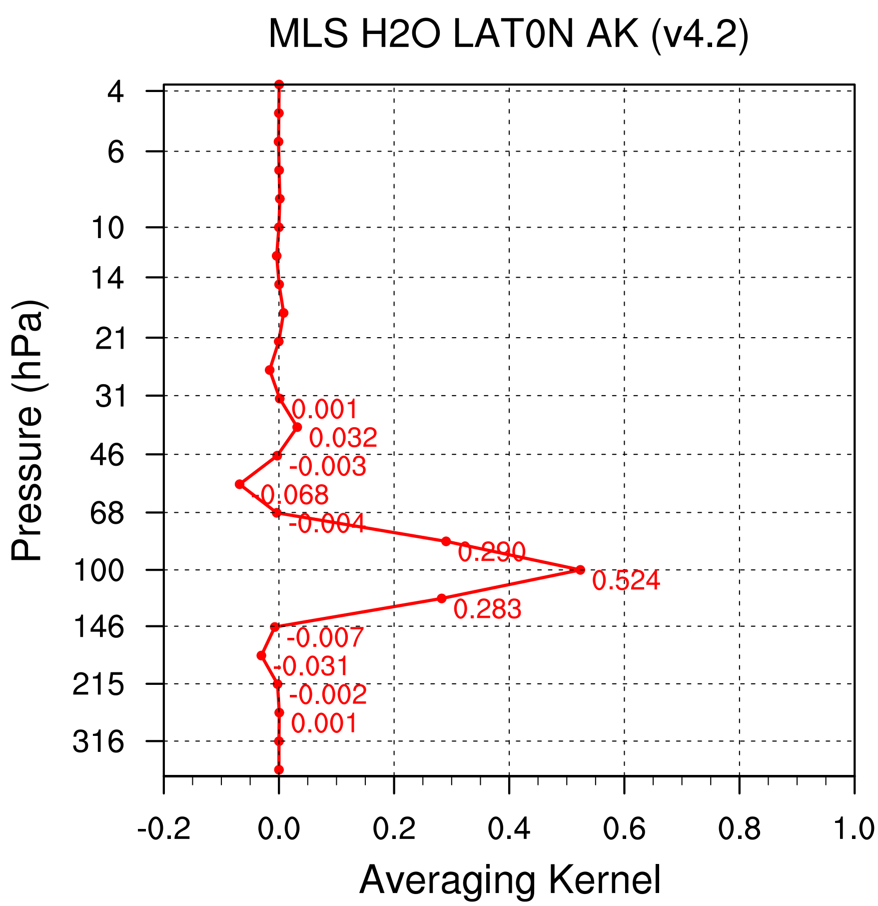


Figure A.1. Equatorial averaging kernel from MLS v4.2 for pressure level 100 hPa.

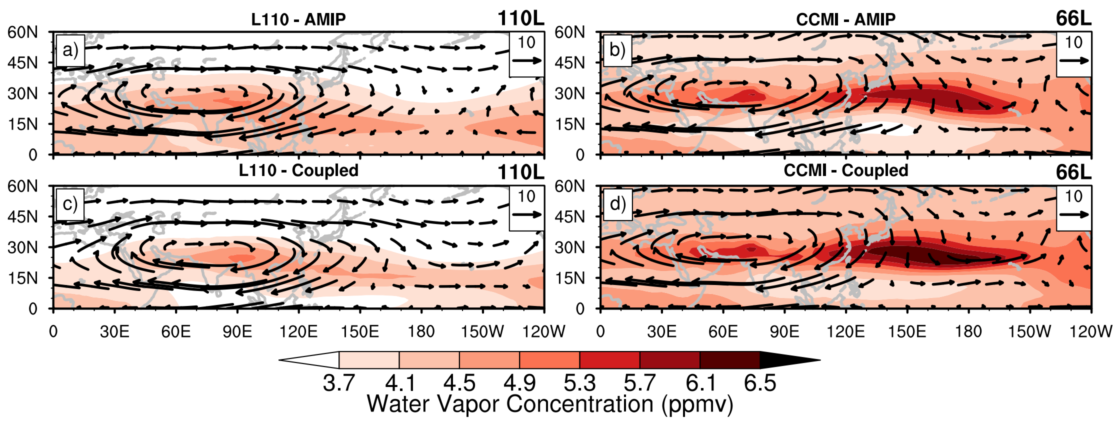


Figure A.2. The summertime horizontal structures of stratospheric water vapor (ppmv, in shadings) and winds (m/s, in vectors) at 100hPa in L110 (on the left) and WACCM CCMI version (on the right). (a) and (b) show the AMIP-style runs. (c) and (d) show the coupled runs. The time period averaged is 1979-2014. Number on the right corner in each plot suggests the total model vertical layers. The results are relatively insensitive to the time period chosen (not shown).

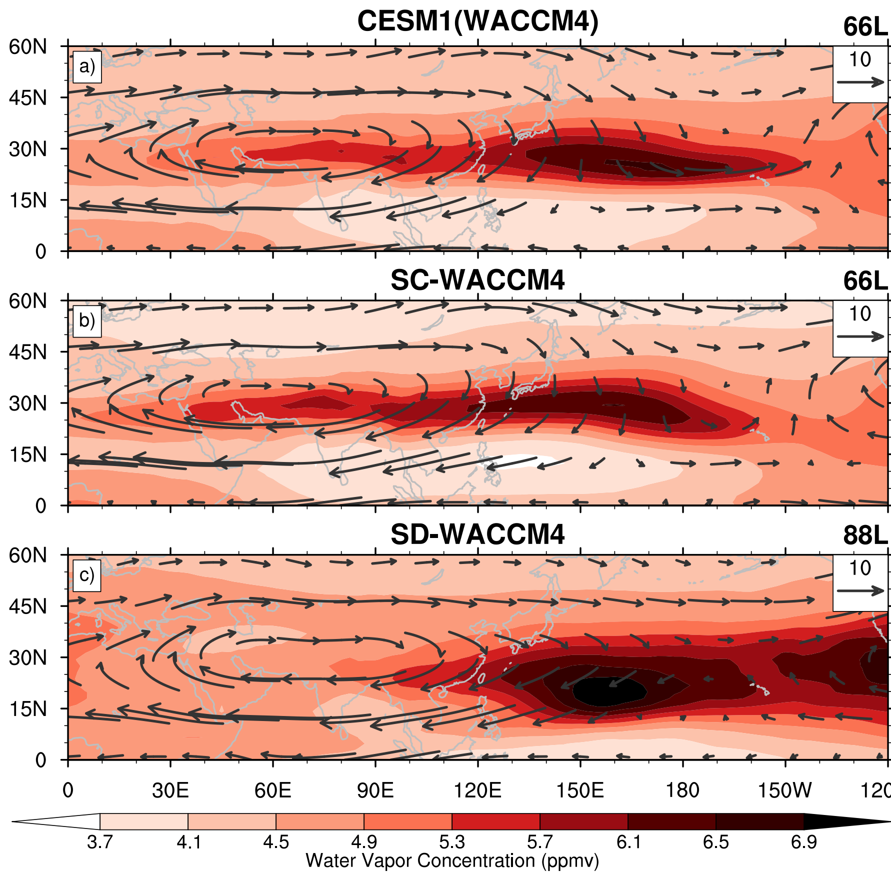


Figure A.3. The summertime horizontal structures of stratospheric water vapor (ppmv, in shadings) and winds (m/s, in vectors) in the different configurations of WACCM4 at 100hPa averaged over (a) 1950-2006 that is available from CESM1(WACCM4) in CMIP5 archive, (b) 1950-2008 that is available from SC-WACCM4, (c) 2005-2010 that is available from SD-WACCM4. Number on the right corner in each plot suggests the total model vertical layers.

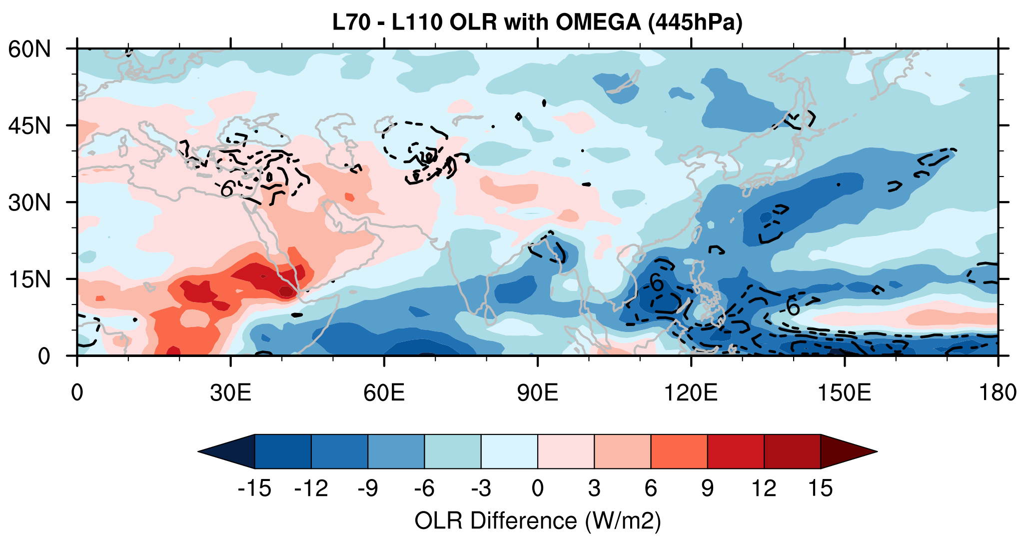


Figure A.4. Differences in outgoing longwave radiation (in shadings) and 445 hPa ascent pressure velocity with $-5 \times 10^{-3}$ Pa/s interval between L70 versus L110.

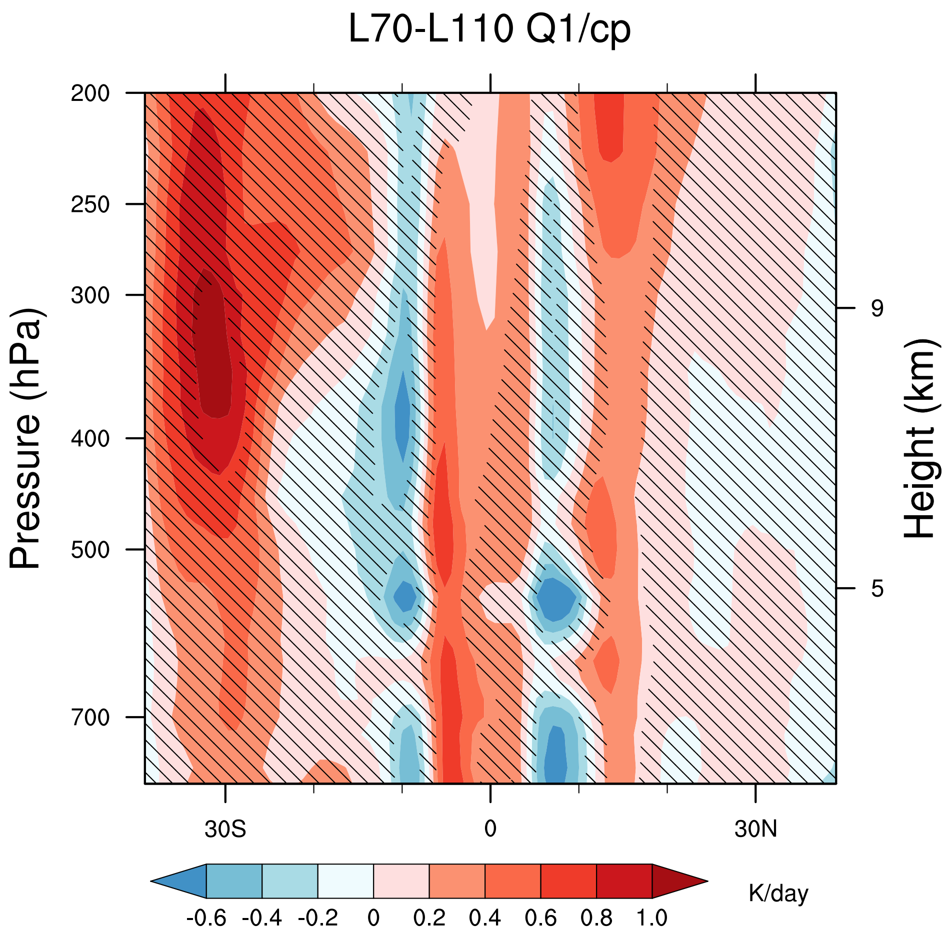


Figure A.5. Latitudinal cross section of heating rate difference (K/day, color shading), averaged between 170°E and 150°W, between L70 and L110. The hatching in the right indicates where the regression coefficient is not statistically significant at the 95% confidence level using the Student $t$-test.

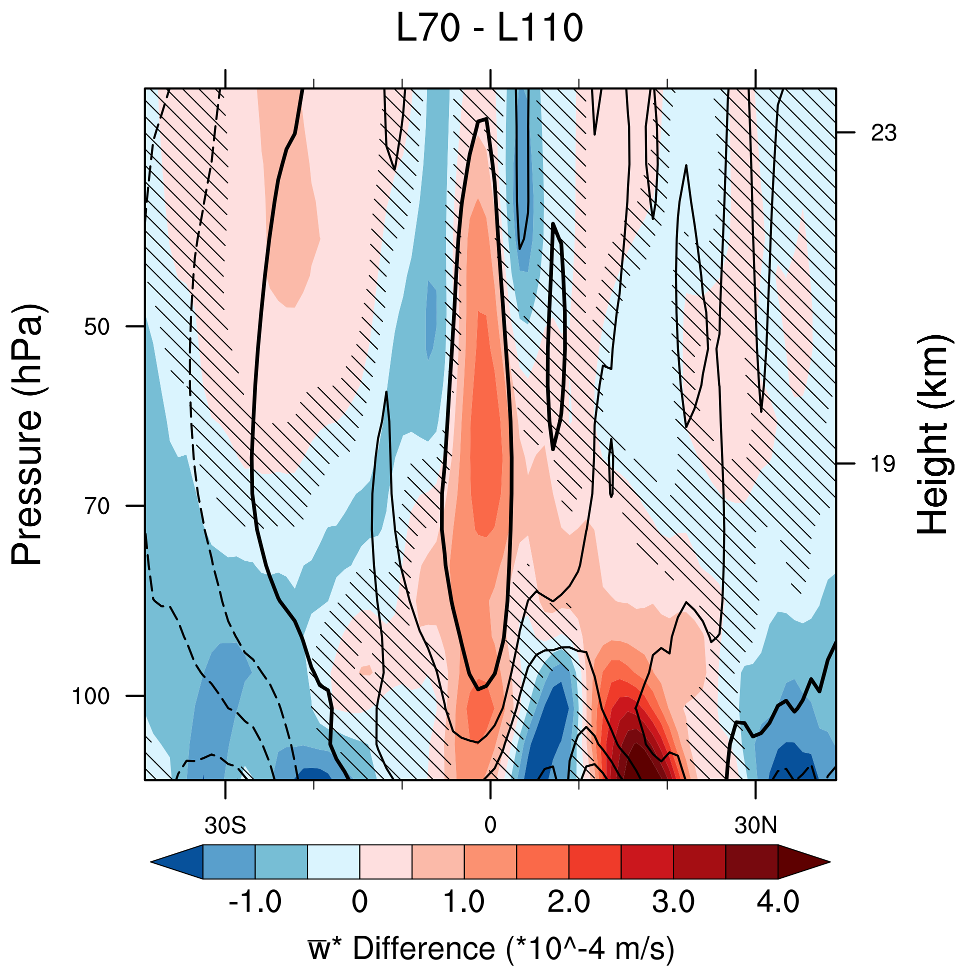


Figure A.6. Difference in $\bar{w}^*$ between L70 and L110 above 110 hPa (color shading). Black contours represent the climatology in L110 with solid contours for positive values, thick solid for zero and dashed for negative values with interval $2.5 \times 10^{-4}$ m/s. The hatching is the same as in Fig. A.5.

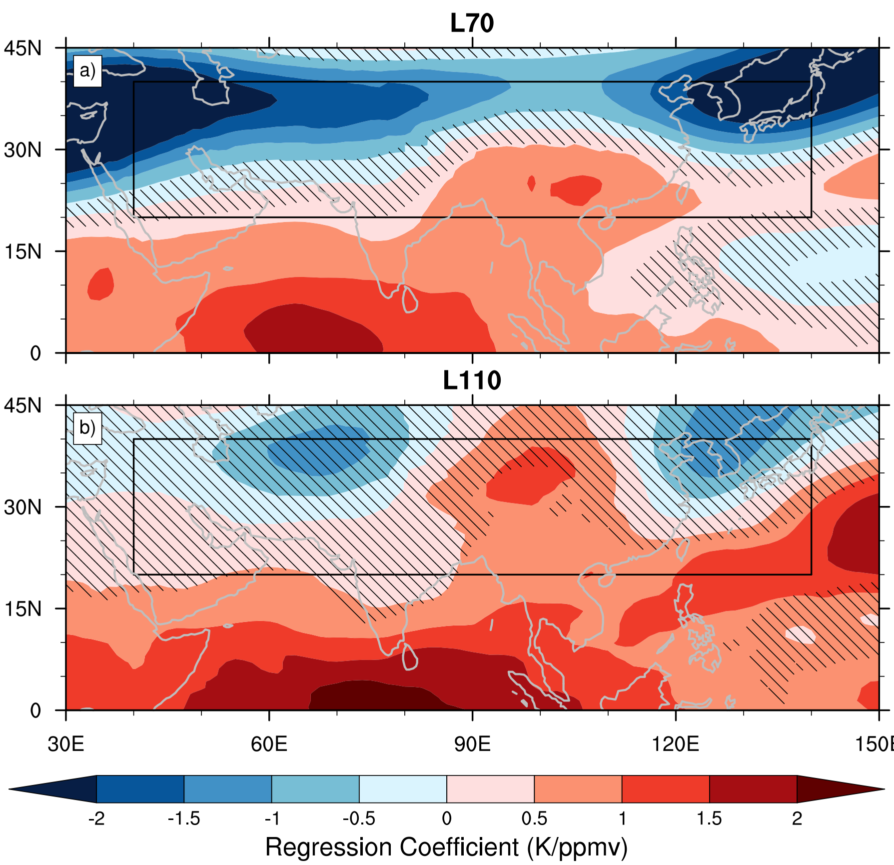


Figure A.7. The regression coefficient between the stratospheric water vapor averaged in the black box (20°-40°N and 40°-140°E) and temperature field at 100 hPa during 1979 to 2014 in (a) L70 and (b) L110. The hatching is the same as in Fig. A.5.

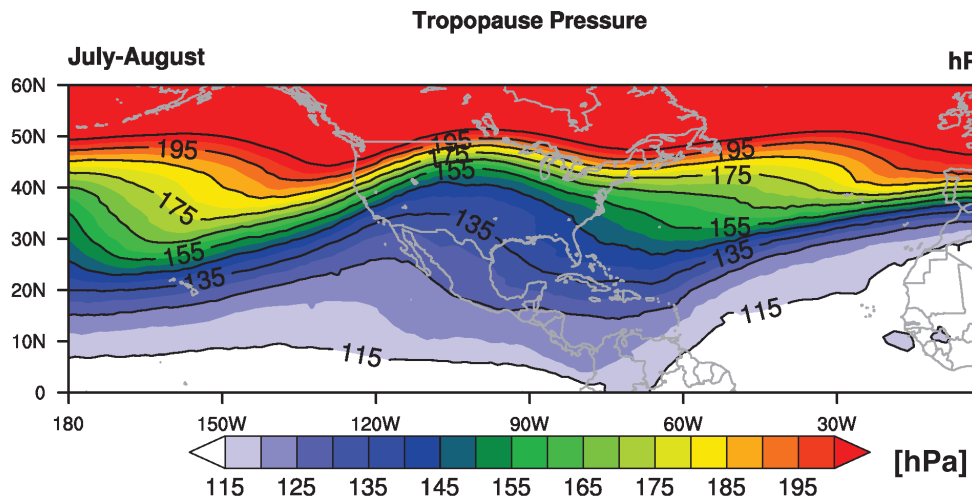


Figure A.8. The climatological tropopause pressure in July and August (contour interval of 10 hPa). The tropopause level is calculated as the lowest pressure level at which the temperature lapse rate decreases to 2 K/km for each day.

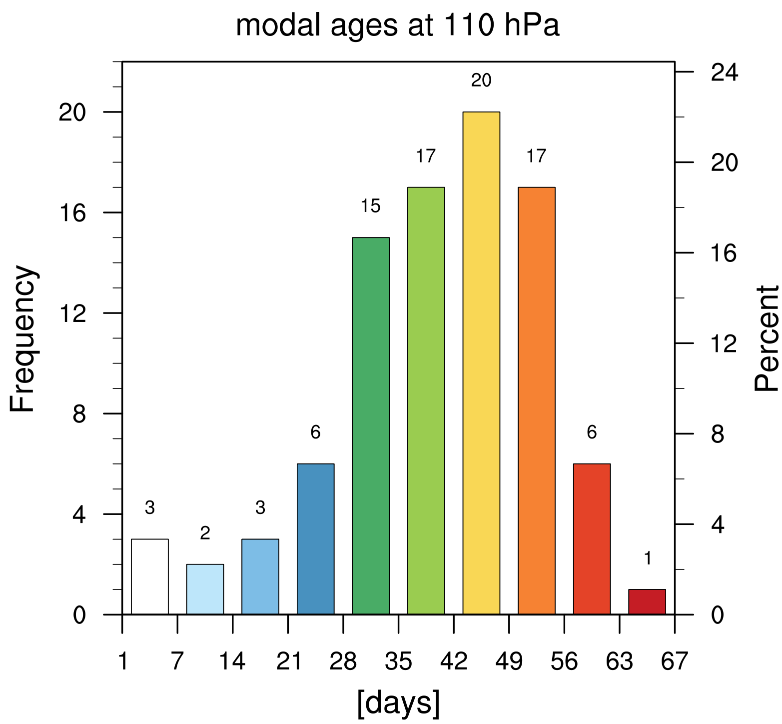


Figure A.9. Modal age distribution of 90 BIR tracer ensembles averaged over 10°N-40°N and 140°W-60°W at 110 hPa.

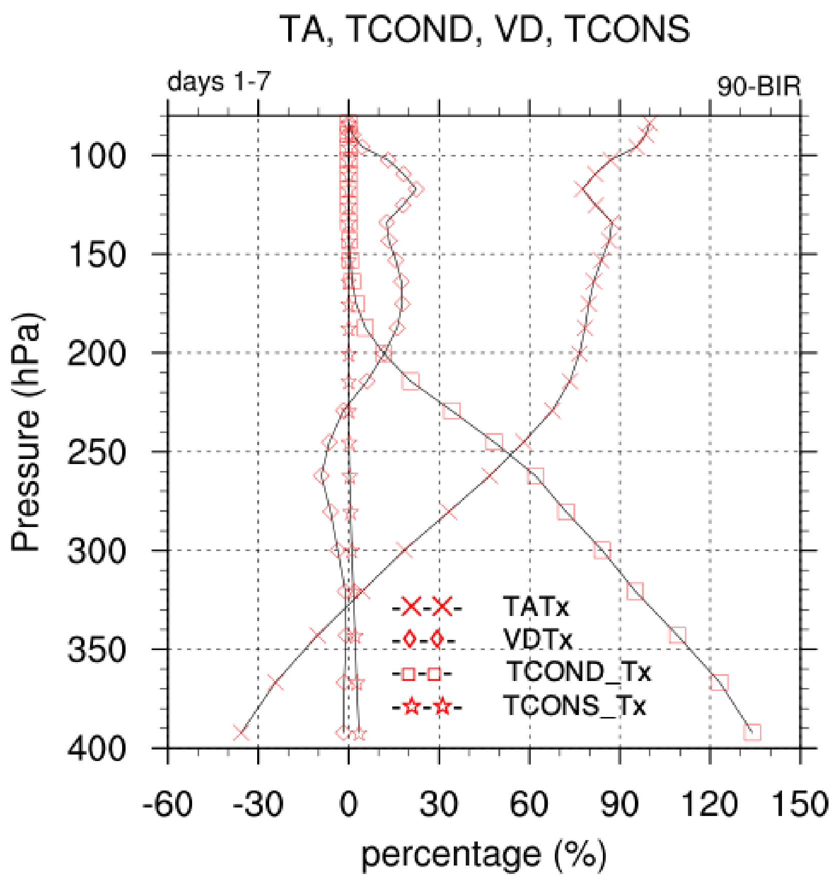


Figure A.10. Vertical profiles of the relative contribution due to resolved dynamics (cross-line), due to deep convection (square-line), due to vertical diffusion (diamond-line), and due to shallow convection (star-line) after averaging over the box area during the first week. The four terms are plotted as a function of pressure from 400 hPa to 80 hPa.

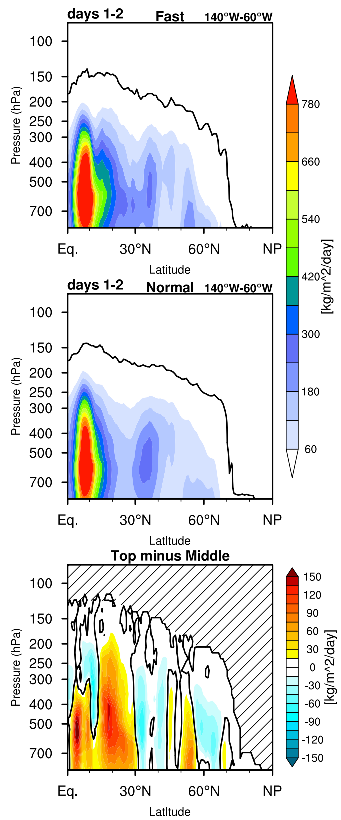


Figure A.11. Vertical-latitudinal cross-sections of the convective mass flux from Zhang-McFarlane (ZM) scheme averaged between 140°W-60°W for the fast ensembles (top row), the normal ensembles (middle row), and their difference (bottom row) in days 1-2. Black contours in the bottom panel are the zero contour lines. The hatching denotes the region where the differences are not statistically significant at the 95% confidence level using the bootstrap method.

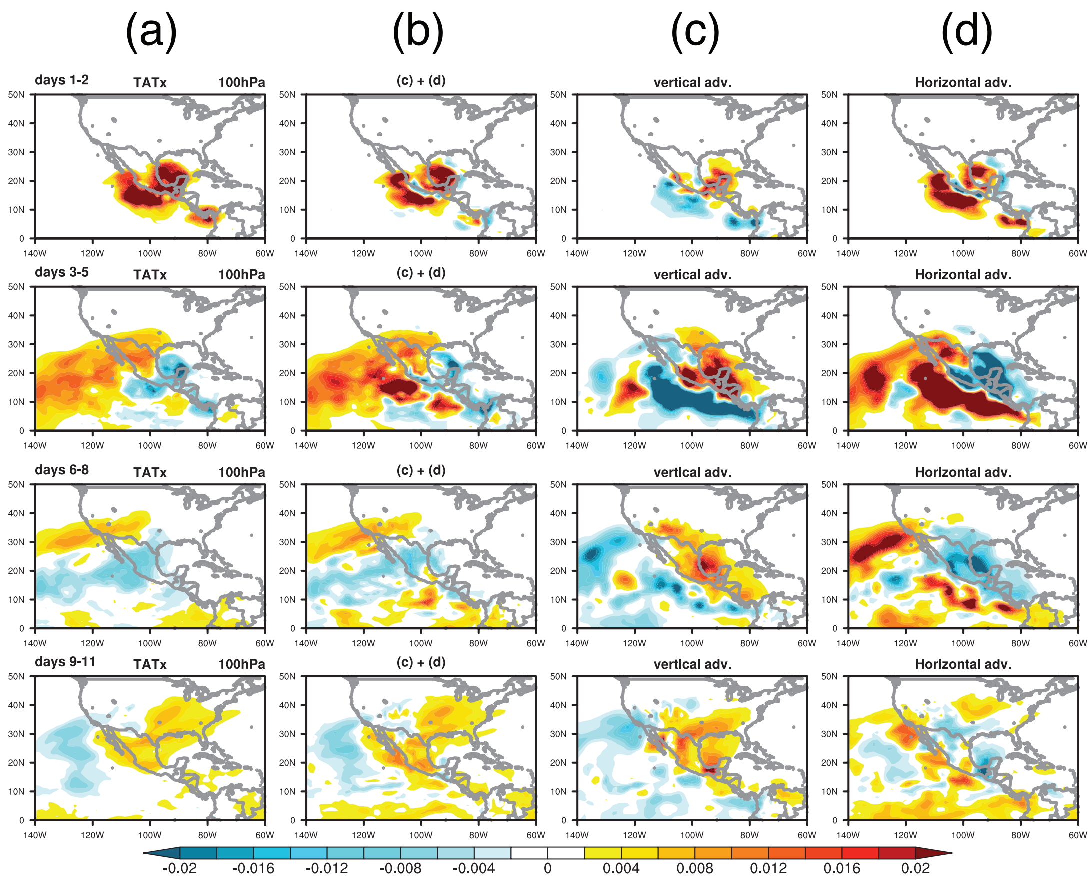


Figure A.12. Decomposition of the resolved dynamics-driven transport tendency (TATx) related to the fast ensembles (column a) into vertical advection component (column c) and horizontal advection component (column d). Column (a) is the first row in Figure 4. (b) is the sum of (c) and (d).

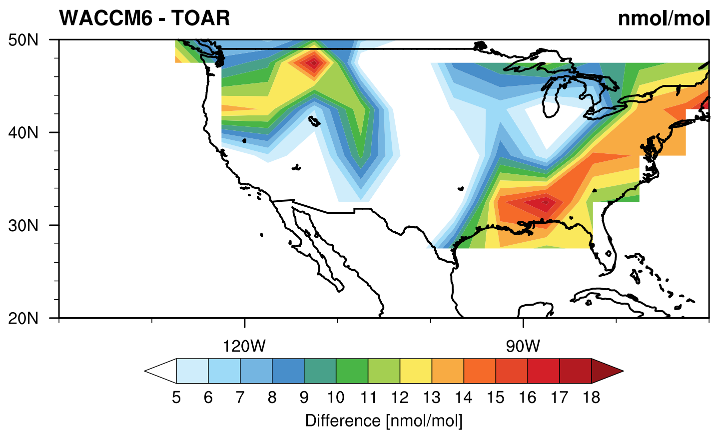


Figure A.13. The absolute difference between the near-surface median $O_3$ value simulated by WACCM6 (Figure 1b) and TOAR observation (Figure 1a) during June-August, 1995-2014.

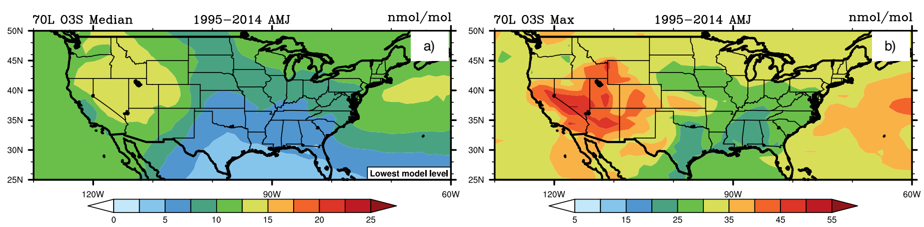


Figure A.14. Distributions of the near-surface (a) median and (b) maximum $O_3S$ concentrations from April-June 1995-2014 estimated by the WACCM6 model.

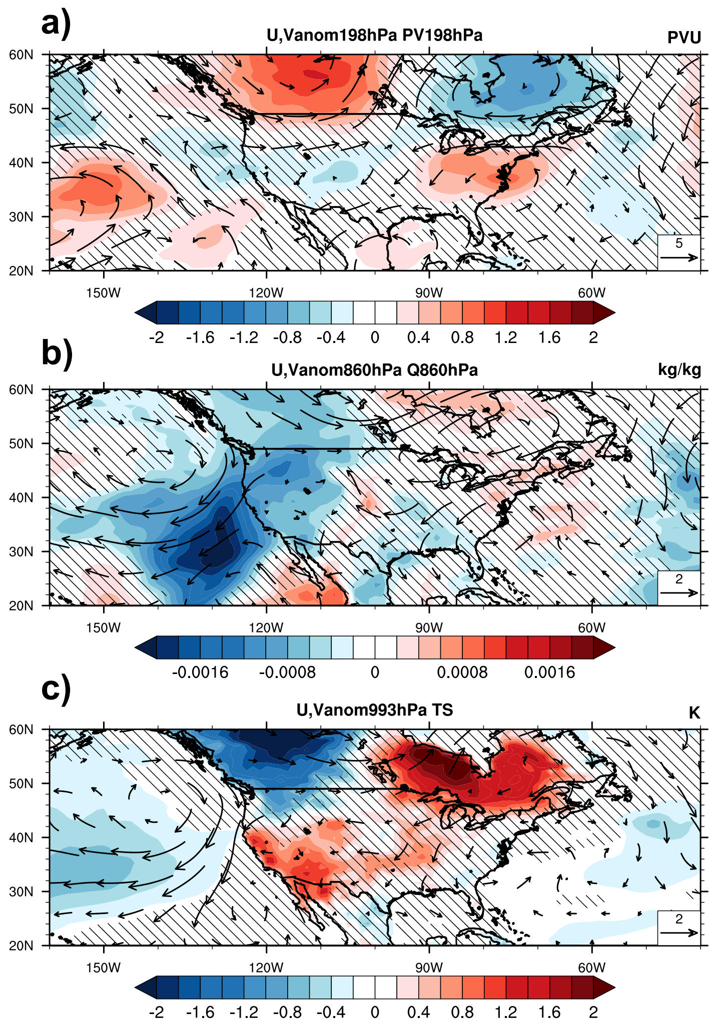


Figure A.15. (a) A map of 200 hPa PV anomalies (in colors, PVU) with wind anomalies (in vectors, m/s) composited to the defined high surface $O_3$ events for Mode 1, (b) composited anomalies in specific humidity at 860 hPa pressure surface (Q860, kg/kg, in colors) and winds at 860 hPa (in vectors, m/s), and (c) composited near-surface temperature anomalies (in colors, K) and surface wind anomalies (in vectors, m/s) corresponding to Mode 1. The hatching denotes that the anomalies are not statistically significant at the 95% confidence level using the Student's $t$ test.

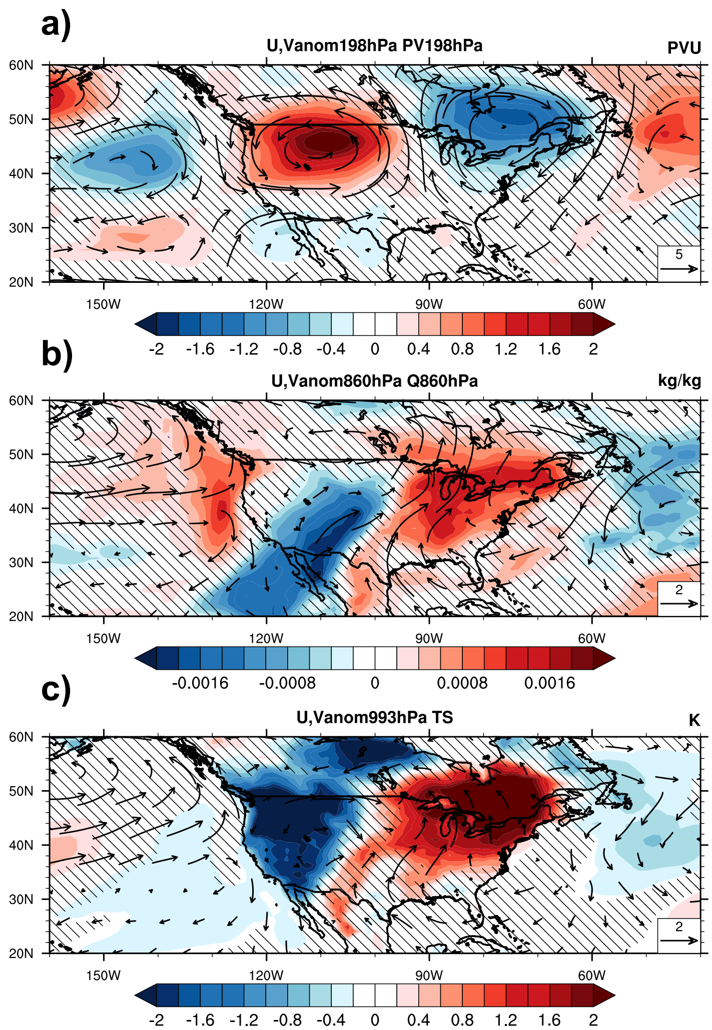


Figure A.16. Similar to Fig A.15 but for Mode 2.

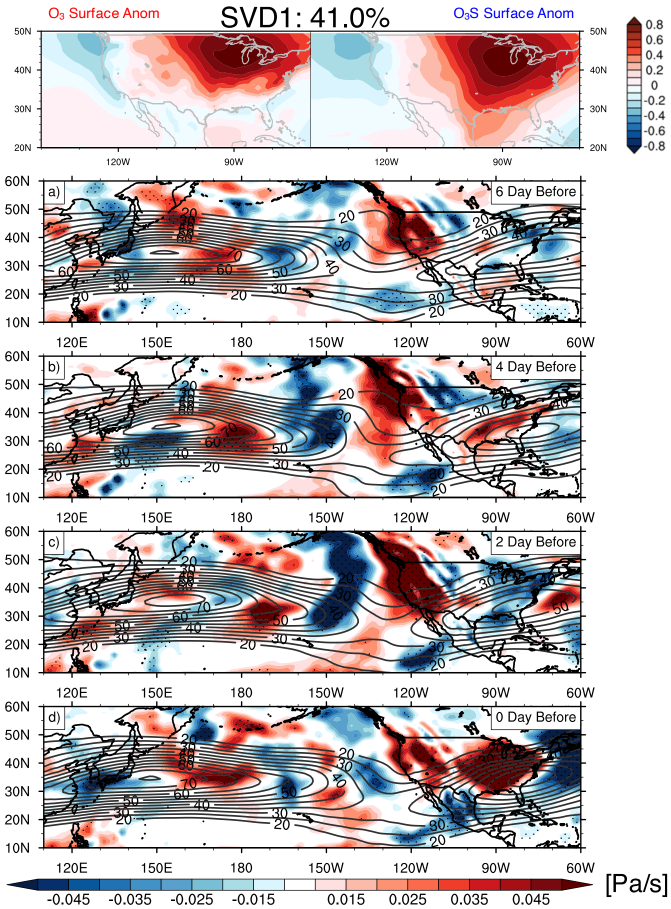


Figure A.17. Upper panel displays the heterogeneous covariance patterns between surface $O_3$ anomalies and surface $O_3$S anomalies regarding the first leading mode from MCA during winter months (DJF) over 1995-2014. Red (blue) color shadings stand for positive (negative) values. The number shown in the top center is the portion of the covariance explained by the first mode. Below are snapshots of composited mean of 500 hPa $\omega$ anomalies (in colors, Pa/s) and 200 hPa zonal winds (in contours, m/s) when large events occur for Mode 1 in DJF from day -6 to day 0 (a-d). Red (blue) colors indicate regions with anomalous descent (ascent). Contour interval is 5 m/s. Stippling indicates that the $\omega$ anomalies are statistically significant at the 95% confidence level using the Student's $t$ test.

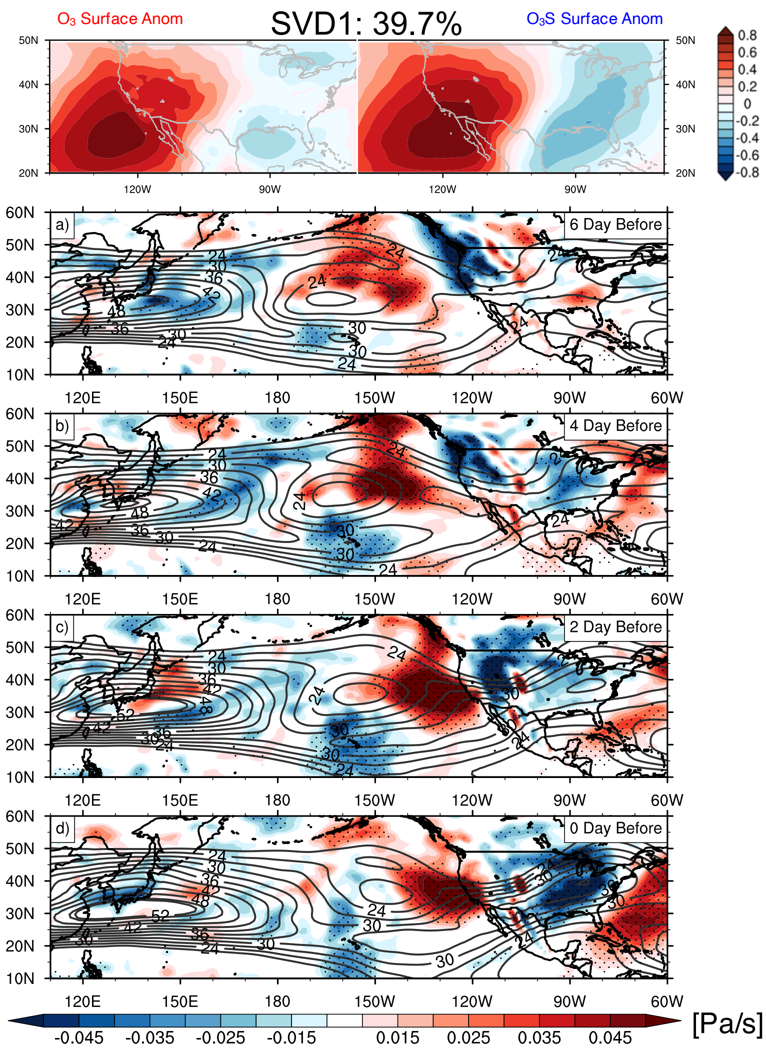


Figure A.18. Same as Figure A.17 but for spring months (March-April-May). In Figure (a) to (d), zonal winds at 200 hPa are in contours (m/s) with 3 m/s interval.

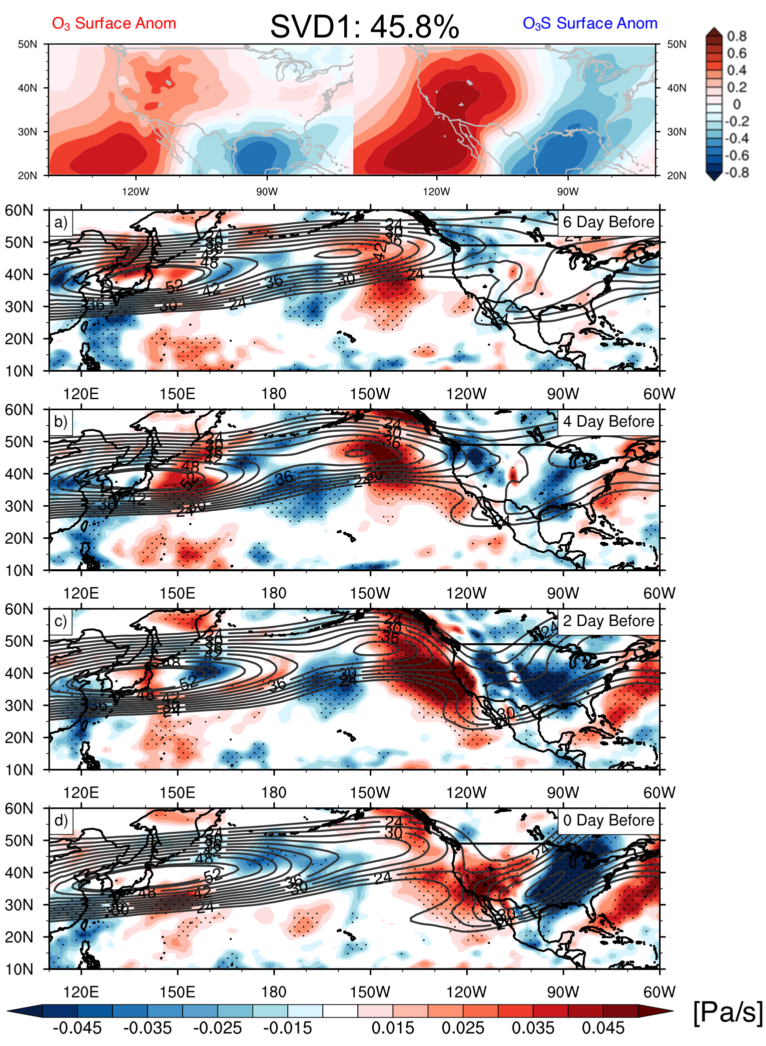


Figure A.19. Same as Figure A.17 but for fall months (September-October-November). In Figure (a) to (d), zonal winds at 200 hPa are in contours (m/s) with 3 m/s interval.